August 2016

Molecular Dynamics Study of Solid-Liquid Heat Transfer and Passive Liquid Flow

Sumith Yesudasan Daisy
Syracuse University

ABSTRACT OF DISSERTATION

Molecular Dynamics Study of Solid-Liquid Heat Transfer and Passive Liquid Flow

by

Sumith Yesudasan Daisy

Doctor of Philosophy in Mechanical and Aerospace Engineering
Syracuse University, Syracuse, NY
August 2016

High heat flux removal is a challenging problem in boilers, electronics cooling, concentrated photovoltaic and other power conversion devices. Heat transfer by phase change is one of the most efficient mechanisms for removing heat from a solid surface. Futuristic electronic devices are expected to generate more than 1000 W/cm^2 of heat. Despite the advancements in microscale and nanoscale manufacturing, the maximum passive heat flux removal has been ~300 W/cm^2 in pool boiling. Such limitations can be overcome by developing nanoscale thin-film evaporation based devices, which however require a better understanding of surface interactions and liquid vapor phase change process. Evaporation based passive flow is an inspiration from the transpiration process that happens in trees. If we can mimic this process and develop heat removal devices, then we can develop efficient cooling devices. The existing passive flow based cooling devices still needs improvement to meet the future demands. To improve the efficiency and capacity of these devices, we need to explore and quantify the passive flow happening at nanoscales. Experimental techniques have not advanced enough to study these fundamental phenomena at the nanoscale, an alternative method is to perform theoretical study at nanoscales.

Molecular dynamics (MD) simulation is a widely accepted powerful tool for studying a range of fundamental and engineering problems. MD simulations can be utilized to study the

passive flow mechanism and heat transfer due to it. To study passive flow using MD, apart from the conventional methods available in MD, we need to have methods to simulate the heat transfer between solid and liquid, local pressure, surface tension, density, temperature calculation methods, realistic boundary conditions, etc. Heat transfer between solid and fluids has been a challenging area in MD simulations, and has only been minimally explored (especially for a practical fluid like water). Conventionally, an equilibrium canonical ensemble (NVT) is simulated using thermostat algorithms. For research in heat transfer involving solid liquid interaction, we need to perform non equilibrium MD (NEMD) simulations. In such NEMD simulations, the methods used for simulating heating from a surface is very important and must capture proper physics and thermodynamic properties.

Development of MD simulation techniques to simulate solid-liquid heating and the study of fundamental mechanism of passive flow is the main focus of this thesis. An accurate surface-heating algorithm was developed for water which can now allow the study of a whole new set of fundamental heat transfer problems at the nanoscale like surface heating/cooling of droplets, thin-films, etc. The developed algorithm is implemented in the in-house developed C++ MD code. A direct two dimensional local pressure estimation algorithm is also formulated and implemented in the code. With this algorithm, local pressure of argon and platinum interaction is studied. Also, the surface tension of platinum-argon (solid-liquid) was estimated directly from the MD simulations for the first time. Contact angle estimation studies of water on platinum, and argon on platinum were also performed.

A thin film of argon is kept above platinum plate and heated in the middle region, leading to the evaporation and pressure reduction thus creating a strong passive flow in the near surface region. This observed passive liquid flow is characterized by estimating the pressure, density,

velocity and surface tension using Eulerian mapping method. Using these simulation, we have demonstrated the fundamental nature and origin of surface-driven passive flow. Heat flux removed from the surface is also estimated from the results, which shows a significant improvement can be achieved in thermal management of electronic devices by taking advantage of surface-driven strong passive liquid flow. Further, the local pressure of water on silicon di-oxide surface is estimated using the LAMMPS atomic to continuum (ATC) package towards the goal of simulating the passive flow in water.

MOLECULAR DYNAMICS STUDY OF SOLID-LIQUID HEAT TRANSFER AND PASSIVE LIQUID FLOW

by

Sumith Yesudasan Daisy

B.Tech. University of Kerala, 2005
M.Tech. National Institute of Technology, 2007

Dissertation
Submitted in partial fulfillment of the requirements for the degree of
Doctor of Philosophy in Mechanical and Aerospace Engineering.

Syracuse University
August 2016

Acknowledgements

I would like to thank Professor Shalabh C. Maroo for his guidance and support in the research work. I would like to thank Professor Ashok Sangani and Professor Alan J. Levy for their valuable suggestions in the development of the molecular dynamics code.

I would like to thank my parents, especially my mother for encouraging and guiding me in the right path since the childhood. I would like to thank my wife and children for their support and encouragement throughout the PhD program.

I would also like to thank my fellow lab mates and friends that I made during these four years. Life in this snow city would have been boring and terrible if I haven't had friends like Srikumar, Kevin, Nikolay, Phil, Dhirendra, An Zou, Geoffrey and Peetak.

Finally, I would like to thank Prof. Ben Akih-Kumgeh, Prof. Ashok Sangani, Prof. Sureshkumar, Prof. Dannenhoffer and Prof. Young B. Moon for serving as my defense committee members.

Table of Contents

List of Tables

List of Figures

1 Introduction and Literature Review

1.1 Motivation and Problem Definition

High heat removal from hot solid surfaces is a challenging and an ongoing research area, especially in the applications like boilers, heat exchangers, gas turbines, concentrated photovoltaic, integrated chips, etc. Currently, the heat flux removed from concentrated photovoltaic (Figure 1-1a) and integrated chips (Figure 1-1b) are in the range of 50-100 W/cm^2. Due to the technological advancements in these fields, in the near future we require heat flux removal technologies in the range of >1000 W/cm^2 [1]. The existing cooling technologies are not sufficient to cool these devices. However in theory [2], up to 20 kW/cm^2 heat can be removed from a surface using evaporative heat transfer while using water as the liquid. We can develop highly efficient and powerful cooling devices if we understand the nanoscale thin film evaporation and physics behind passive fluid flows. Such passive pumping devices can decrease the gap between the existing cooling techniques and the theory.

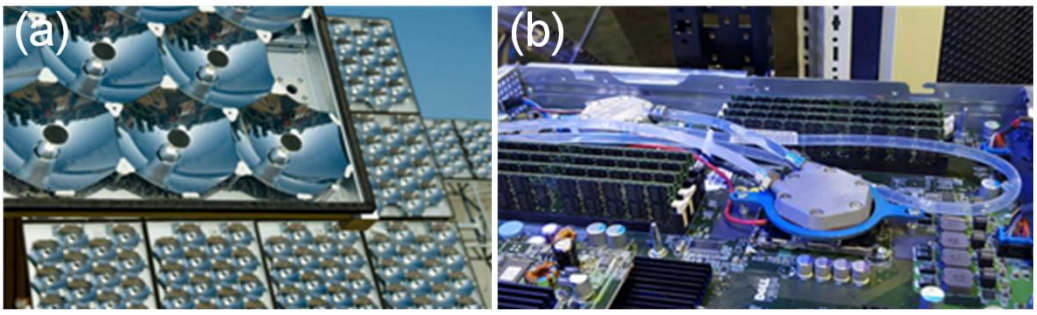

Figure 1-1. Concentrated photovoltaic and integrated chip cooling. (a) A close-up view of concentrated photovoltaic (image courtesy: manfred.amoureux.free.fr). (b) A liquid based cooling for integrated chips (image courtesy: datacenterfrontier.com)

Passive pumping technology is an inspiration from the natural phenomenon called transpiration. Transpiration is the phenomenon, in which the trees transport water from roots to the leaf and other aerial tips. The evaporation from the aerial pores called stomata can lead to a

negative pressure creation in the xylem, which along with the capillary pressure, molecular interactions and cohesive forces of water pulls the water and transports it to heights of ~100 m in redwood trees [3], which would require ~10 times the atmospheric pressure for pumping water to such heights. The osmotic pressure in the roots will pull the water from soil to the tree and makes the transpiration phenomenon a continuous supply of water in the system.

If we can mimic transpiration and develop highly efficient bio-inspired passive pumping cooling devices, then we can meet the future cooling demands. The passive flow is believed to occur due to the presence of negative pressure at nanoscales. A liquid is said to be under negative pressure when it is pulled against its cohesive forces and attaining sub saturation pressures without cavitation. This can happen in nanopores and nanochannels where disjoining pressures can become dominant at nano length scales. They can cause high absolute negative pressures in liquid films [4]. It has been shown that water can exist at extreme metastable state and attain high negative pressures [5] at nanoscales. Molecular [4] and continuum simulations [6] have also been performed on occurrence of negative liquid pressure. Cavitation cannot occur in these regions as the characteristic dimension is smaller than the critical cavitation radius. These studies show that we can utilize this high potential negative pressure which is in metastable condition, by evaporative based passive flow.

In 2008, Tobias et al. [7] demonstrated the wicking action of water in trees by performing experiments in a synthetic "tree". Figure 1-2a gives the schematic details of liquid water entrapped in a spherical void in a synthetic membrane. Water activity or a_w is the partial vapor pressure of water in a substance divided by the standard state partial vapor pressure of water, μ is the chemical potential. The water in void is subjected to cavitation due to the negative pressure created in it while reducing the water activity above the boundary. From cavitation theorem, a negative

pressure of -220 bar was estimated. Figure 1-2b shows the synthetic tree with leaf and root networks. The synthetic tree captured negative pressure existence, continuous heat transfer with the evaporation of liquid water at large negative pressures and continuous extraction of liquid water from sub saturated sources.

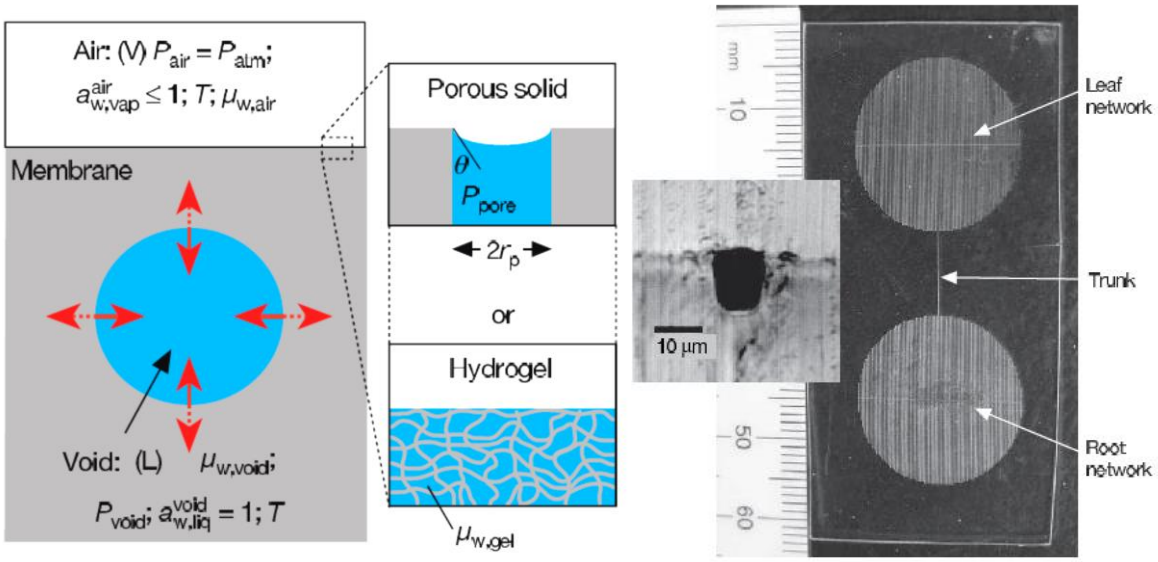

Figure 1-2: (a) Schematic cross section view of liquid water entrapped in a spherical void within a membrane. (b) Optical image of transparent sheet of synthetic tree containing a void in the form of a micro channel network at its mid plane [7].

Experiments have been conducted which confirm the existence of negative liquid pressures. In 1955, Briggs [8] heated water in a thin walled sealed capillary tube up to 267°C until it exploded. His work predicted that the explosion happens when the cohesive forces are not sufficient to hold the water molecules together. He concluded that the water must have been under high negative pressure just before the explosion. His theory was in line with Maxwell's theory of heat [9]. He conducted a series of experiments with different liquids and his theoretical prediction and experimental results were closely matching which bolsters his argument. Further, devices based on this concept and experiments were performed.

In 2003, Niels et al. [10] reported that water plugs can exist at negative pressures of 17 ± 10 bar by filling water in a hydrophilic silicon oxide nano-channel of approximate height of 100 nm. Figure 1-3 shows the optical micrograph of nano water plug in a 10 μm channel. To obtain this, they filled the nanochannels with water and left it for drying. The drying induced curvature of water as shown in Figure 1-3 which led to building up of capillary pressure. This capillary pressure started bending the nanochannels and based on the elastic modulus and geometric deflection they estimated the pressure to be -17 bar in the water plug.

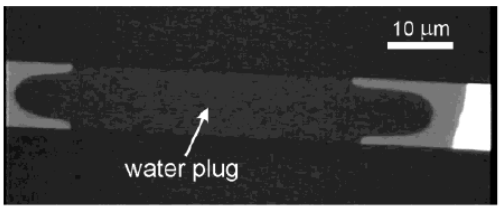

Figure 1-3: Optical micrograph of a water plug in a 10μm wide nanochanel during drying [10].

In 2008, Seung et al. [11] measured pull off force between a nanoscale Silicon Atomic Force Microscope (AFM) tip and a silicon wafer in air and in ultra-high vacuum. The experiments were conducted with different humidity in the surrounding air. This humidity caused microscopic condensation near the AFM tip and silicon wafer. These condensed water served as a bridge between them and the negative pressure (attractive) held them together. The difference between the force values from experiments in ultra-high vacuum and air gave more accurate estimation of Laplace pressure inside the liquid bridge. They attained negative pressures as high as -160MPa. Figure 1-4 shows the schematic of their experiment.

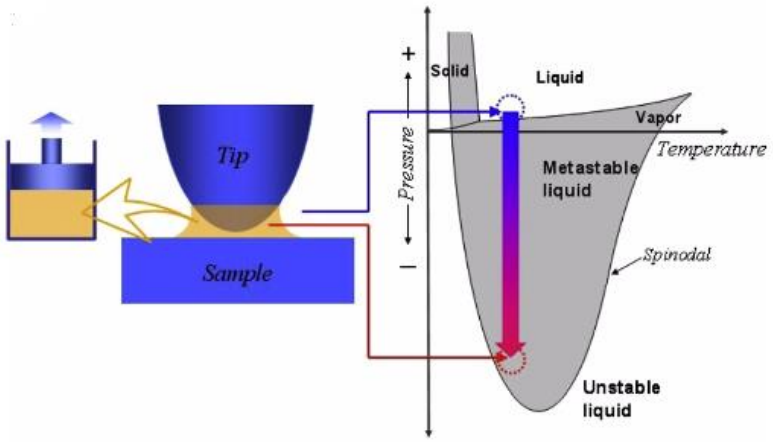

Figure 1-4: Schematic of the water phase diagram showing a metastable capillary bridge [11]. The graph shows the variation of pressure with temperature.

In 2008, Nosonovsky et al. [12] discussed the size effect of system and its impact on phase diagram. In their paper, they discussed that the phase of the water in nano confinements are undetermined experimentally and plays an important role in the MEMS/NEMS applications. They also discussed the existence of nano bubble formation near the AFM tips. Closely following the work of Seung et al. [11], they updated the phase equilibrium diagram of water for nano scale. The AFM tip pull-off force versus the humidity from Seung et al.'s work is discussed again here, without much explanation about the reason behind the peak force occurring at 30 % relative humidity. Also, Nosonovsky et al. have shown that the boiling can happen at temperatures much lower than the saturation temperatures at corresponding vapor pressure.

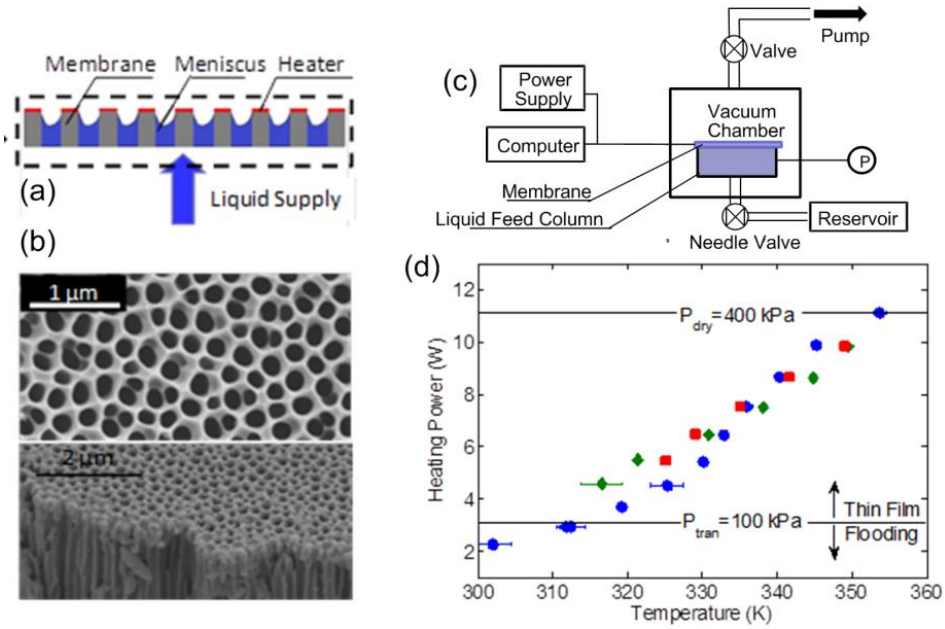

Figure 1-5: Nano porous membranes and negative pressure existence [13].

In 2013, Xiao et al. [13] performed experiments on alumina membranes to mimic passive flow based heat transfer, demonstrated the existence of high negative pressures of -3 bar which were capable of dissipating heat fluxes about 96 W/cm^2. They fabricated the porous alumina membranes with average pore diameter of 150 nm and iso propyl alcohol (IPA) as the working fluid was supplied from bottom. The top of the porous alumina was heated which led to the evaporation of the IPA and stimulating a passive liquid pumping. They have suggested the characterized dimensions required to improve such devices to accommodate heat fluxes above 1000 W/cm^2. Figure 1-5 shows the nano pores and resulting pressure inside them.

Although a few studies have been performed in literature to study negative liquid pressures, the transpiration effect has not been shown in simulations yet. Surface effects of disjoining and capillary pressures at such nanoscale lengths play a vital role, and are lacking in literature for water as the transport fluid. The main objective of this work is to attain fundamental understanding into these surface phenomena which dictate the transpiration effect while coupled with heat transfer.

The insights gained can be potentially used to design nanoscale devices to achieve high heat flux removal with passive liquid pumping.

The past few decades have seen the evolution of molecular dynamics (MD) simulations due to the advent of computers and fast computing. Molecular dynamics is the term used to describe the solution of the classical equations of motion (Newton's equations) for a set of molecules. This was first accomplished for a system of hard spheres by Alder and Wainwright [14] in 1957. Several years later in 1964, Rahman [15] solved the equations of motion for a set of Lennard-Jones particles. MD simulation was used to improve the understanding of phase transitions and behavior at interfaces [16]. Moreover the nanoscale experiments can be simulated more accurately using MD simulations, and we can achieve better understanding of the physics behind adhesion and passive flows at those length scales.

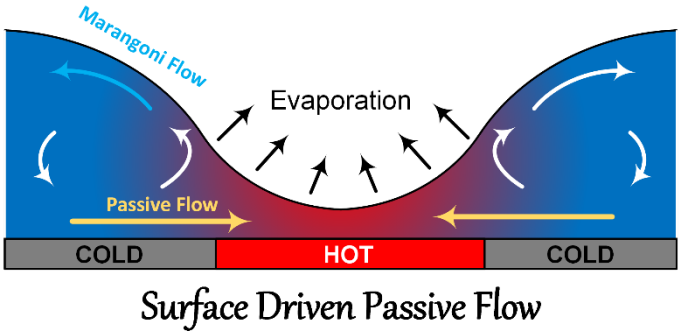

Figure 1-6. A conceptual model to study the evaporative based passive flow system.

A conceptual model to study the evaporation based passive flow system using MD is shown in Figure 1-6. The system has a thin film of liquid kept on top of a solid substrate. The heat transferred from the solid will heat the liquid. The middle region is kept at a higher temperature compared to the sides. This is expected to evaporate from the middle region and a passive flow in the system.

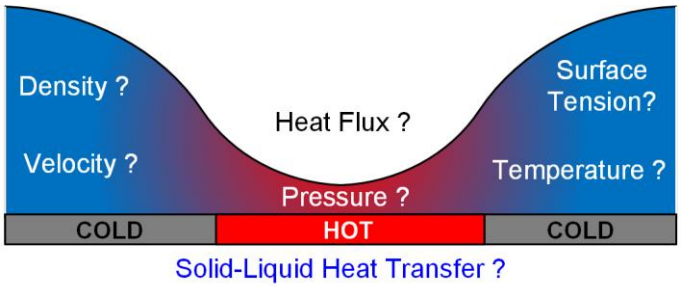

Figure 1-7. Set of properties to be estimated or tracked during the passive flow simulation using MD.

In order to study the passive flow system as shown in Figure 1-6 using MD simulations, we need to estimate the thermodynamic properties near the surface as shown in Figure 1-7. We need the following list of methods to capture and analyze the passive flow using MD simulations.

1. Accurate Solid-Liquid heat transfer method
2. Local pressure, surface tension estimation methods
3. Density, velocity and temperature estimation from Eulerian mapping
4. Custom boundary conditions like adiabatic walls on top

To perform MD simulation studies, we can either use an open source MD software by modifying it with above modules or we can develop our own MD code and implement the modules on it. Due to the complexity in understanding and modifying the existing codes, we developed our own MD code in C++.

1.2 Objectives of this Thesis

The main objectives of this thesis are described as following.

Develop a molecular dynamics simulation code in C++. This includes implementation of commonly used modules to perform MD simulation. Next is to develop a heat transfer algorithm to simulate the heat transfer between solid and water. The current methods available in the literature is not sufficient and accurate to simulate the heat transfer behavior of water and platinum using molecular dynamics simulations. This algorithm had to be validated and implemented in the

code. After that we need to develop accurate methods for estimating pressure, density, surface tension, and temperature in MD simulations to understand and visualize the local variations of these properties in the simulation domain. These methods have to support the thermodynamic parameter estimation in 3D, 2D and in 1D. The code has to be implemented with custom made boundary conditions, data input-output formatting modules, contact angle estimation modules etc. Finally utilizing all the developed modules and using our MD code, simulate passive flow and estimate the heat flux removed using evaporative heat transfer.

Upon completion of these series of objective, we are expected to understand and quantify the origin of passive liquid flows induced by evaporative heat transfer. These findings can be used to develop continuum level models to simulate and predict the passive flow.

1.3 Structure of this Thesis

The structure of this thesis is explained in the below paragraphs.

In chapter 2, we will discuss the development of an in-house C++ code to perform MD simulations and chapter 3 will show the validation of that code. The existing solid-liquid heat transfer algorithms for water are inadequate and not accurate. This makes the first objective to develop such an algorithm and validate it. Modifying the existing open source MD codes like LAMMPS or GROMACS was an option. However, due to the flexibility in developing and implementing new modules, an in-house code is written. This objective requires development of an MD code in C++ language and implementation of major modules of molecular dynamics simulation methodology in to it. Chapter 2 explains the fundamental blocks of the code and chapter 3 gives the validation details of the code. The widely used and essential MD modules like velocity verlet integrator, smooth particle mesh ewald, RATTLE etc. will be implemented in this code.

In chapter 4, the estimation of local thermodynamic properties like pressure, velocity and density and development of newer and faster methods are discussed. The local estimation

algorithms play an important role understanding and characterization of properties of the passive flow systems. Often the system under study will be 2D inhomogeneous and doesn't require a full 3D knowledge of the pressure and density. The classical approach of Hardy to use a 3D smearing (interpolation) function to distribute the pressure across the local 3D grids have to be modified appropriately to account for 2D grids. This local pressure module has to be validated by studying the surface tension and density of the liquid argon suspended in the vapor argon. The validated code can then be used to estimate the surface tension of liquid-solid interface of argon-platinum, directly from the MD simulations. The details of the local pressure formulation, its validation and other case studies are discussed in detail in chapter 4.

In chapter 5, the passive flow induced cooling of a system is simulated using MD simulation of argon and platinum. Using the surface heating algorithm for argon-platinum, we can simulate the passive flow of the liquid under a thermal gradient and estimate the heat removal rate. A thin film of argon will be kept on top of a platinum plate and will be heated in the middle at a higher temperature than the sides. This will create a differential thermal zone and eventually lead to difference in the solid-liquid surface tension. This gradient is expected to create a flow from the sides to the center of the system. The mass flow rate can be estimated based on the local density variations and evaporative mass flux can be estimated from the control volume analysis. Using these details and temperature we can estimate the heat removal rate from the system. The details of these MD studies including the passive flow heat flux estimation will be discussed in chapter 5.

In chapter 6, development of a mathematical model to simulate the heat transfer between water and platinum surface is discussed. With this algorithm we can study the heating and cooling of the water droplets and thin films on top of platinum using MD simulations. The development details and other validation cases are discussed in the chapter 6 and will be implemented in our in-

house developed C++ code. Using the validated code we can study the surface-liquid interaction behavior for argon-platinum and water-platinum. These studies can be done by conducting contact angle estimation and evaporation induced by surface heating. We will discuss a robust contact angle estimation algorithm in chapter 3 and a few case studies using that algorithm. The evaporation of thin films is another way to establish the validity of the surface heating algorithms. We will demonstrate the heating and evaporation of thin films of argon from platinum surfaces in chapter 3.

1.4 Publications Resulting from this Thesis

Aspects of the dissertation has already been published/ submitted for review. Reference to the publications are given below:

Chapter 3: Sumith YD, Shalabh C. Maroo. "Contact Angle Estimation Algorithm for Water and Argon Droplets", (*ICNNM 2015 conference and HTE journal 2016*)

Chapter 4: Sumith YD, Shalabh C. Maroo. "A Direct Two-Dimensional Pressure Formulation in Molecular Dynamics", 2016 (*under review*)

Chapter 5: Sumith YD, Shalabh C. Maroo. "Origin of Surface Driven Passive Flows", 2016 (*under review in Langmuir*)

Chapter 6: Sumith YD, Shalabh C. Maroo. "Surface Heating Algorithm for Water at Nanoscale", *The Journal of Physical Chemistry Letters* (2015)

2 Molecular Dynamics Simulation

In this chapter, a brief introduction of the molecular dynamics (MD) simulation will be provided, followed by details regarding the computational steps behind the molecular simulations performed, different inter-atomic potential functions used, force-field parameters used for the simulations, different MD simulation modules' implementation in the in-house software, and the thermodynamic properties evaluation. These methodologies were used while creating and using our own MD simulation software written in C++ language and are explained in the subsequent sections of this chapter.

2.1 Introduction

Molecular dynamics is a computer simulation method for studying the transient physical movements of atoms and molecules, and is thus a type of N-body simulation [17]. Atoms and molecules are allowed to interact each other using a potential for a desired period of time, giving a view of the dynamical evolution of the system. In the most common version, the trajectories of atoms and molecules are determined by numerically solving Newton's equations of motion for a system of interacting particles, where forces between the particles and their potential energies are calculated using interatomic potentials or molecular mechanics force fields.

A graphical representation of main steps involved is shown in Figure 2-1. These steps will be explained in detail in the following sections.

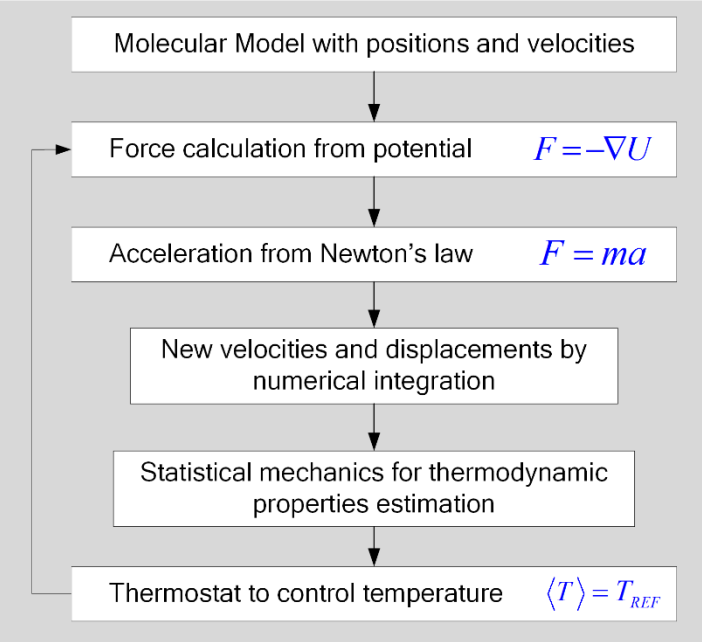

Figure 2-1. Flow chart for MD simulation.

2.1.1 Initial configuration of atoms

As a first step, atoms and molecules are arranged in a specific configuration according to the problem description. This data, as x, y, and z coordinate information, is generally created as a file readable to the MD simulation software. Sometimes we may need to supply the information of the initial velocities of these atoms/molecules in the case of prior knowledge of velocities.

2.1.2 Velocity verlet integrator

The force acting on individual atoms are calculated using the negative gradient of the interatomic potential, from which the acceleration on each particle can be found from Newton's laws of motion.

$$F = -\nabla U \tag{2-1}$$

where F is the force on each particle, U is the interatomic potential.

From the acceleration, velocities and displacements of the particles are calculated using finite difference methods. The widely used velocity Verlet algorithm is adopted for simulation purposes, and takes the form shown below.

Velocity can be found by

$$v(t+h)=v(t)+\tfrac{h}{2}\left[a(t)+a(t+h)\right] \tag{2-2}$$

Displacement can be found by

$$r(t+h)=r(t)+hv(t)+\frac{h^2}{2}a(t) \tag{2-3}$$

Using these mathematical steps we can calculate the time evolution of the atoms, as well as visualize their motion using appropriate software. For performing molecular dynamics simulations, verlet based integrators are superior compared to Runge-Kutta methods, because they are symplectic (conserve energy and time reversible), computationally efficient and have good stability.

2.2 Thermodynamic Properties Estimation

This section deals with the methods to calculate different thermodynamic properties of the simulation system such as temperature, pressure and density.

2.2.1 Temperature

The temperature of the system is calculated based on the Equipartition theorem. Equipartition predicts that the average total energy of N particles or atoms in three dimensions is given by $\frac{3}{2}Nk_BT$. where k_B is the Boltzmann constant, T is the instantaneous temperature.

Thus $\frac{3}{2}Nk_BT=\frac{1}{2}\sum_i m_i v_i^2$ (2-4)

The temperature can then be calculated as $T = \frac{\sum_i m_i v_i^2}{3Nk_B}$

The degree of freedom will be different for rigid molecules. In case of rigid molecules the temperature calculation formula will become.

$$T = \frac{1}{(3N - N_C)k_B} \sum m_i v_i^2 \tag{2-5}$$

where N_C is the number of constraints in the system, like fixed bond lengths and angles. For rigid water with 3 sites, if N_W is the number of water molecules then the temperature is estimated as

$$T = \frac{1}{(9N_W - 3N_W)k_B} \sum m_i v_i^2 = \frac{2KE}{6N_W k_B} \tag{2-6}$$

where m_i is the mass of the i^{th} atom, $N_C = 3N_W$, $N = 3N_W$.

2.2.2 Pressure

Though the molecular dynamics method is a deterministic method, the trajectory information alone is seldom important, and the thermodynamic variables calculated using statistical mechanics is of importance. Most of the simulations are performed to obey a Canonical (NVT) or a micro Canonical (NVE) ensemble. Thus the system obeys statistical physics laws and measurements are averaged over time to obtain average statistical properties. For such a simulation the pressure can be found from the Virial expansion and its modified version is applied to slab geometry by Nijmeijer et.al [18].

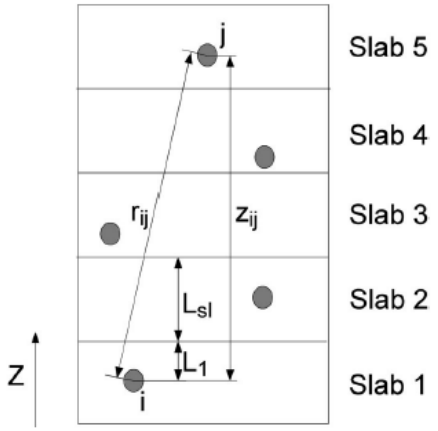

Figure 2-2: Simulation space portioned into imaginary slabs along a direction [19].

The pressure tensors for normal P_N and tangential P_T pressures are given by

$$P_N(k) = n(k)k_B T - \frac{1}{V_{sl}} \sum_{i,j}^{k} \frac{z_{ij}^2}{r_{ij}} \phi'(r_{ij}) f_{k,ij} \tag{2-7}$$

$$P_T(k) = n(k)k_B T - \frac{1}{V_{sl}} \sum_{i,j}^{k} \left(\frac{1}{2}(x_{ij}^2 + y_{ij}^2) \frac{\phi'(r_{ij}) f_{k,ij}}{r_{ij}} \right) \tag{2-8}$$

where $n(k)$ is the number density of the atoms in the kth slab, k_B is the Boltzmann constant, T is the temperature of the slab k, V_{sl} is the slab volume, x_{ij}, y_{ij} and z_{ij} are the components of the vector between atoms i and j, $\varphi'(r_{ij})$ is the gradient of the potential, $f_{k,ij}$ is the factor which determines the proportional contribution of pressure to every slab due to atoms i and j. $\sum_k f_{k,ij} = 1$

For 2D and 3D systems the pressure at local regions can be estimated with the help of interpolation functions and this will discussed in detail with our new methodology in section 4.2.

2.2.3 Density profiles

The density profiles for 1D cases are obtained by simply allocating the mass of the atoms into respective slabs of predetermined thickness and averaging with the slab volume.

$$\rho(z) = \frac{n(z)}{V_S} \tag{2-9}$$

where n is the number density multiplied by mass of the atom, V_S is the slab volume. For 2D and 3D cases the density profile calculation will be discussed in chapter 4.

2.2.4 Thermostat schemes

Majority of the MD simulations are carried out at a specific temperature of the system. Thermostat algorithms are used to produce desired temperature in MD simulations. The group of atoms, which are intended to be at the average temperature, will be subjected to one of such algorithms. The most widely used thermostat schemes are Nose-Hoover[20], velocity scaling, velocity re-scaling[21] and Berendsen[22]. In this work the thermostat schemes that we used are velocity scaling or Berendsen thermostat, unless explicitly mentioned in the respective MD studies.

The velocity scaling method starts with the instantaneous temperature T_{inst} calculation. The scale factor λ is then found by

$$\lambda = \sqrt{\frac{T_{REF}}{T_{inst}}} \tag{2-10}$$

This scale factor λ is multiplied with velocity components of every molecule, which are supposed to be coupled with the thermostat, at every time step of integration.

$$V_{new} = \lambda V_{old} \tag{2-11}$$

The Berendsen thermostat is another widely used approximate NVT ensemble simulator which includes a time component into the scale. A detailed derivation can be found on the original paper [22].

The Berendsen scale factor λ is defined as

$$\lambda = \sqrt{\left[1 + \frac{\Delta t}{\tau}\left(\frac{T_{REF}}{T_{inst}} - 1\right)\right]} \tag{2-12}$$

where Δt is the time step of numerical integration and, τ is the time constant which describes the strength of coupling to heat bath. τ is generally taken as 0.1 ps for most of the simulations. The remaining procedure is same as of velocity scaling.

The Nose-Hoover thermostat modifies the Hamiltonian of the system by adding an extra degree of freedom for temperature.

$$H_{Nose} = V(q) + \sum_{1}^{N} \frac{p_i^2}{2m_i} + \sum_{1}^{M} \frac{p_{\varsigma i}^2}{2Q_i} + NkT\varsigma_1 \tag{2-13}$$

where ς is the thermostat variable, it is used to scale the momentum. Q represents the mass of the thermostat. N is number of atoms, k is Boltzmann constant, T is reference temperature, V is potential energy and p is momentum. The set of equations evolving from this modified Hamiltonian is expected give an accurate canonical ensemble.

2.2.5 Ensemble averaged results

The results of the MD simulation have to be interpreted in a meaningful way. Statistical mechanics is a powerful tool to relate the MD data of atom positions and velocities into physical and measurable properties of the system such as temperature, pressure, density etc. However, these properties have to be sampled and averaged from the resulting MD data over a long period of time. For our analysis, we have typically found that an averaging for 1000 ps provides conclusive results for surface tension, pressure, and density values matching with experimental values for different temperatures.

2.3 Interatomic Potentials

The interatomic potential defines the way in which the atoms and molecules interacts in the system. In our work, we have used non-bonded Lennard Jones potential, Coulomb potential and ZP potential.

2.3.1 LJ potential

The first type of potential is Lennard Jones (LJ) Potential which accounts for weak van der Waal's attraction and also Pauli Exclusion Principle. The potential equation can be written as

$$V_{LJ} = 4\varepsilon\left[\left(\frac{\sigma}{r}\right)^{12} - \left(\frac{\sigma}{r}\right)^{6}\right] \tag{2-14}$$

where σ is the distance at which the potential becomes zero, ε is the strength of the potential and r is the spacing between the atoms.

2.3.2 Coulomb potential

The second type of interatomic interaction is the Coulombic potential, which is the attraction or repulsion between two charges or multi poles.

$$V_{Coulomb} = \frac{1}{4\pi\varepsilon_0}\frac{q_1 q_2}{r} \tag{2-15}$$

where q is the partial charge of the atom, r is the spacing between the atoms and ε_o is the permittivity of free space.

Typical values of LJ parameters and partial charges are given in Table 2-1.

Table 2-1. Values of typical parameters used for simulation

Species	ε [J]	σ [nm]	q [e]
Argon – Argon	1.6567782×10^{-21}	0.34	0
Argon - Platinum	8.94127465×10^{-22}	0.3085	0
Oxygen-Oxygen (SPCE)	1.0793×10^{-21}	0.3166	-0.8476
Hydrogen-Hydrogen	0	0	+0.4238

2.4 Code Implementation Details

This section of the chapter explains some of the MD simulation modules implemented into our computer code related to energy and force estimation, domain boundary conditions and restraint algorithm.

2.4.1 Cell list algorithm

The Cell List method is used to improve the speed of the computation of dense atoms or molecules. In the traditional method (brute force approach) of force calculation, every atom in the system is checked with all other atoms in the system. This is computationally very expensive and is in the order of $O\left(N^2\right)$ for N atoms. Instead we can partition the system into small cells of size equal to or less than cutoff radius (Typically ~1 nm).

Once the system is partitioned, the next step is to create a neighbor list which has the list of neighbor cells for every cell within the cutoff radius. Then, a search has to be made only for the atoms within the neighbor cells which are within the cut-off radius (as shown in Figure 2-3). Mattson et al.'s [23] detailed study further improves the efficiency by considering finer cell divisions smaller than the cutoff radius which was proven to be efficient in highly dense fluids.

For our simulations, we typically used grid sizes of 1 nm and each cell contains approximately contains 25 argon atoms.

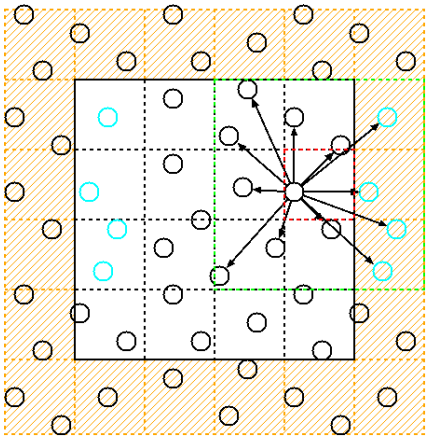

Figure 2-3 Cell list method of partitioning the domain. White cells surrounded by shaded cells are the simulation cells.

2.4.2 Reflective and periodic boundary conditions

In order to approximately simulate an infinite system researchers often use the periodic boundary condition. A unit cell (master cell) is considered the fundamental unit which is periodic in all dimensions under study, with image cells being its exact replica around it. Next, the interaction of atoms in the master cell and with those in the image cells are calculated. If the system is of LJ particles, then a minimum image convention algorithm can be used and the image searching can be limited within one level. However, if it is a Coulombic system of particles then the number levels of image cells will be large, making the computation expensive. In such cases the computationally efficient Ewald summation methods, which will be discuss in detail in the next section, become very useful.

In the case of 2D periodic systems, the non-periodic boundary must be either reflective or should have a physical wall with which to interact. The reflective boundary can be simulated by

defining a region of cushion near the boundary and reversing the direction of the atoms entering into that region from the simulation domain without loss of energy or momentum.

3 Validation of In-House Developed MD Code

In this chapter, we discuss the validation of MD simulation code that was developed in the present study. The code was written in the C++ language and includes all standard and non-standard modules of a MD simulation code explained in chapter two. The code is validated by simulating standard heat transfer examples as explained in this chapter. We start the validation with argon-argon simulations and comparing the results with the experimental phase equilibrium data from NIST [24]. Next, we validate the implementation of argon-platinum heating algorithm [25], followed by the heating and evaporation of argon from the platinum surface. The validation of the water code including the RATTLE is done next by matching the radial distribution from experiments and GROMACS software [26]. Finally we discuss the development of a robust contact angle algorithm and its validation by applying to water and argon droplets.

3.1 Argon Phase Equilibrium Simulation

Argon is an ideal atom for MD validation studies as it has been studied extensively. The abundant information about the properties of argon in literature makes it straightforward to validate the MD code for argon simulations. The first MD computational domain considered is a 5 nm x 5 nm x 12 nm cuboid. This domain, is partitioned into three 4 nm regions in along the Z-direction where the middle region is filled with liquid argon and other two with vapor argon Figure 3-1. As the base case, the system temperature is chosen as 90K and hence the initial configuration consists of 2099 argon atoms based on the saturation density.

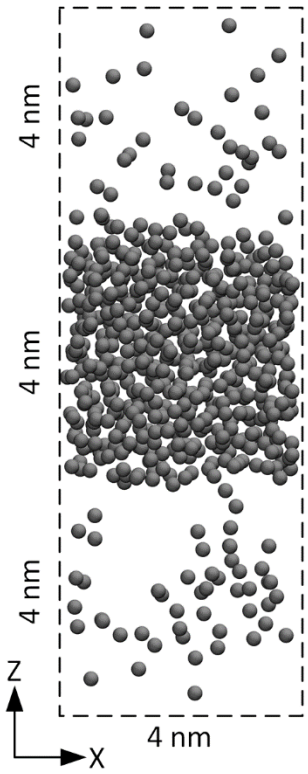

Figure 3-1. Argon liquid film suspended in argon vapor region.

The boundaries are modeled using periodic boundary condition (PBC) which simulates infinite replica of this given domain. MD simulation is performed for the above mentioned simulation model at different system temperatures varying from 90 K to 140 K. Pressure, density, temperature and surface tension are estimated in the domain and is compared with the NIST values. The results shown in the Figure 3-2, Figure 3-3 and Figure 3-4 for pressure, surface tension and temperature, respectively, demonstrate good agreement with the experimentally determined saturation curves. Using these case studies, we have shown that the code is capable of reproducing physically sound results for argon-argon interaction.

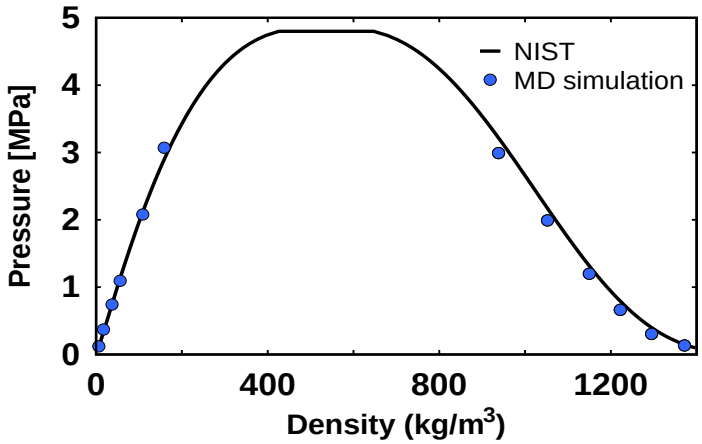

Figure 3-2. Pressure vs. density comparison with standard values from NIST tables [24].

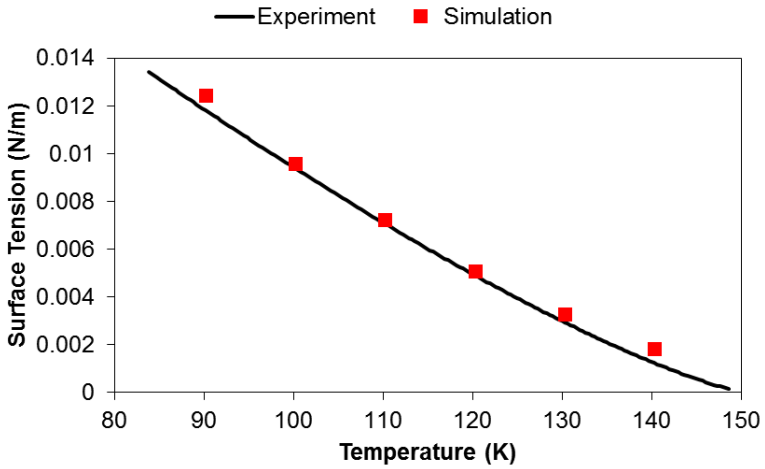

Figure 3-3. Surface tension vs. temperature comparison with standard values from NIST tables [24].

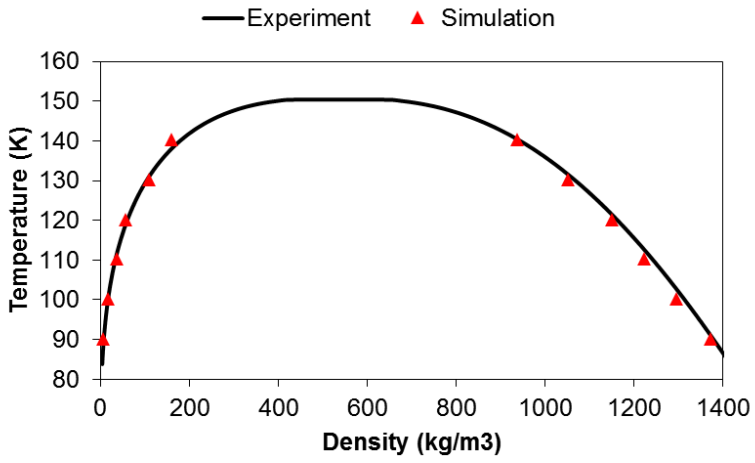

Figure 3-4. Temperature vs. density comparison with standard values from NIST tables [24].

3.2 Thermal wall models

When we use MD simulation, we need to have an accurate method to simulate the heat transfer between solid and liquid atoms. Models to simulate physically-sound transient heat transfer from a surface to water in MD simulations are lacking in literature. Typically, a constant temperature fluid can be attained in MD by coupling it to a thermostat. A few attempts have been made to simulate heat transfer from a surface but are mostly limited to non-polar atoms such as argon. Coupling the bulk liquid directly to a thermostat will produce unrealistic results. It has been pointed out that for boundary driven Couette flow coupling the bulk fluid to a thermostat will produce undesirable and unrealistic results by Liem [27] and Van Der Spoel [28]. They have reported artifacts like layer formation of water in such situations. Also the coupling of bulk liquid with thermostat will remove the temperature gradients and heat fluxes in studies related to Couette flow.

Phonon transport in solid surfaces has much higher vibrational frequencies than those of liquid atoms. MD simulations of phonon transport in literature have roughly used integration time steps an order of magnitude smaller than liquid atoms: for example 0.246 fs to resolve phonon frequencies in PbTe [29], and 0.55 fs to study thermal transport in Silicon substrate [30]. Comparatively, time steps used for liquid atom simulations are in the range of 2 to 5 fs. Thus, accurately coupling solid surface with liquid atoms will either have to involve multi-scale computations or alternatively we have to simulate the liquid and solid at same integration steps in the range of 0.2 to 0.5 fs and will be computationally expensive.

The models that attempt to simulate the heat transfer between solid and liquid can be broadly classified into two. They are the models for LJ type of atoms and the models for water type of polar liquids.

3.2.1 Lennard-Jones liquid heating models

A simple method is to assign a heavy mass to the wall atoms and allow them to move according to the equations of motion. This was proposed by Koplik et al. [31] in 1989. They were inspired by the models suggested by Abraham [32]. Although the wall and fluid conserve the energy, it will disintegrate over the period of time. A widely used method for simulating the thermal wall model is the phantom wall method by Yi et al. [33]. As shown in Figure 3-5 they modeled two additional layers of atoms and anchored the bottom layer. The top phantom layer is then coupled to a Langevin thermostat and all platinum atoms are connected to each other using springs.

The phantom wall method is computationally expensive due to the incorporation of phantom layers of atom and has not been shown to follow the proper physics of evaporation. This was an approximate modeling of phonon transport. However, the heat diffusion results in literature[33] obtained by using these methods do not match the classical heat conduction theory. For example, a thin layer of argon took ~4000 ps to reach the wall temperature, while the theory predicts around 10-30 ps. Further, due to these deficiencies in such models, the interfacial thermal resistance, also known as Kapitza resistance [34] values obtained may possibly be incorrect (as these models are not validated).

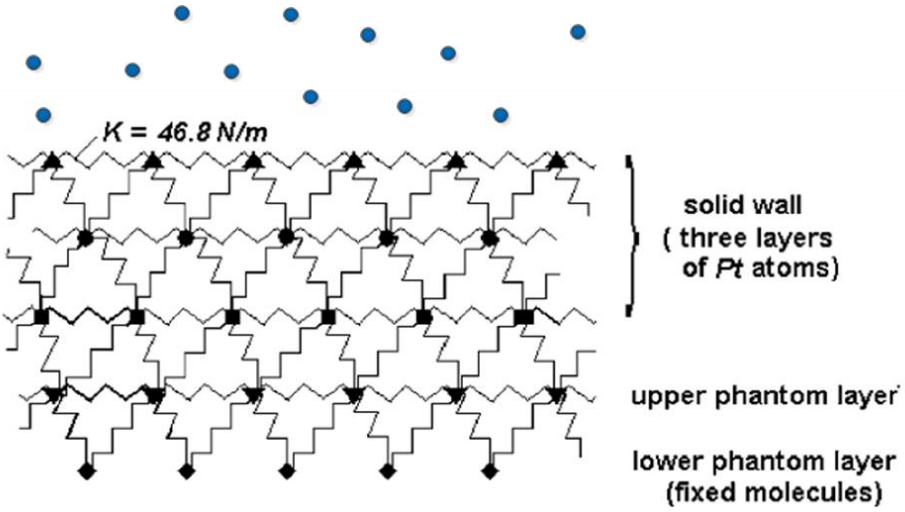

Figure 3-5: Phantom wall method (Reproduced from Yi [33]). Wall atoms are connected with each other using springs.

There exist similar methods by Nagayama et al. [35] to model the heat transfer by creating ghost layers of atoms which are anchored and the solid atoms coupled to thermostat. Their work consisted of understanding the effect of nanostructures on surfaces to the solid-liquid thermal resistance, and also the importance of determining the evaporation rate. They have performed a series of MD simulations with varying nanostructure pattern size and dimensions to study its influence on thermal resistance and evaporation. They also concluded that the evaporation from surfaces with nanostructures are much higher than flat surface. However, the heat transfer method that they used to perform the solid-liquid interaction was not validated.

In 1989, U. Heinbuch and J. Fischer [36] heated liquid by scaling only the layer adjacent to the walls. They called their method Wall Temperature Scaling (WTS) and found to be more realistic in behavior. But it is applied to Lennard Jones (LJ) fluids. They have studied the Hagen – Poiseuille flow of LJ fluid through cylindrical pores. They have claimed that their studies could match the molecular layer formation next to the walls with experimental results. However the extension of this model to heat transfer properties was not discussed in the paper.

In 2014, Hens et al. [37] performed a simulation of argon platinum thermal interaction by coupling the top layer of platinum wall atoms to Nose Hoover thermostat. The paper does not mention the accuracy or validation of this method. Moreover they have modeled six layers of platinum which makes it computationally very expensive for larger systems. Though they have applied a good canonical ensemble generator (Nose-Hoover) to the platinum wall, it won't guarantee the same to the liquid interacting with the wall. Figure 3-6 shows the model used in their work.

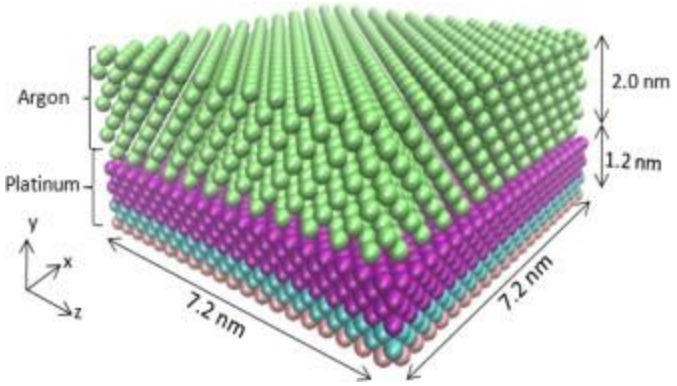

Figure 3-6: Model used by Hens et al. six layers of platinum will interact with the 2nm layer of argon.

In 2010, Bernardi et al. [38] studied the effect of different thermostatting schemes on highly confined liquids. They compared the effect of thermostatting the fluid directly to a thermostat and also to a thermal wall for a small system of LJ fluid confined between walls as shown in Figure 3-7. They have shown that the mechanical properties like shear stress, shear rate, streaming velocity, density and temperature across the channel fluctuates a lot from different thermostats. They have found that thermal wall models produce reasonable and better results compared with the direct coupling of liquid to thermostats. Their work strongly supports the claim to have an accurate model to explain the heat transfer from wall to liquid.

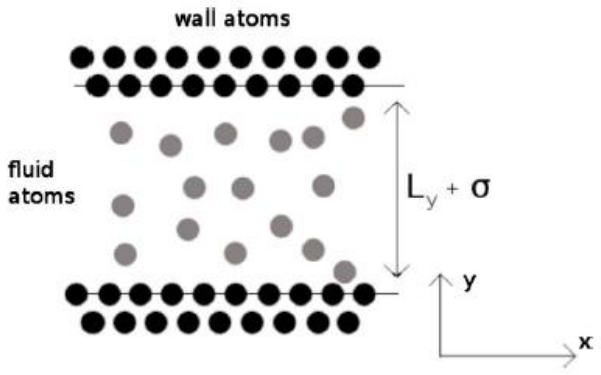

Figure 3-7: Molecular model used by Bernardi et al. [38].

The next step in building and validating the in-house code was to introduce a platinum surface in the domain to create solid-fluid interaction. The modified LJ potential by Stoddard-Ford [39] was used for argon-argon interaction and argon-platinum interactions. The periodic boundary condition along z-axis (vertical) was replaced with rigid (frozen in time) platinum surfaces. For MD simulations, one major challenge is modeling heat transfer between a surface and fluid, i.e. in this case, between atoms on platinum and argon.

3.3 Heating Algorithm for Argon-Platinum

In 2009, Maroo and Chung [25] developed a heat transfer model which simulates the heat transfer between platinum walls and argon atoms. The theory behind this model is to scale the velocity (heat or cool to a desired temperature) of the atoms which have a dominant force acted on by the platinum surface, i.e., the atom should be experiencing a larger force from the surface than from the argon atoms around it. Further, the algorithm has an additional criterion of checking whether the atom is in the repulsive region of the surface. As shown in the Figure 3-8, the region above the surface is divided into three zones. Zone 1, where the distance between surface and atom is less than the critical radius. Critical radius is the distance at which the interaction potential

between argon and platinum becomes minimum. The atoms in this region only experience repulsive force from the surface. The algorithm consists of two conditions as follows.

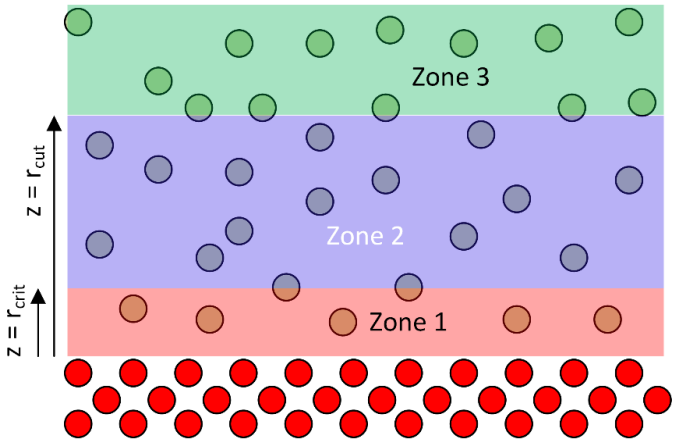

Figure 3-8. Fluid wall thermal equilibrium model [25].

Condition 1: Distance check:

$$z_i < r_{critical} \tag{3-1}$$

where z_i is the particle's shortest distance from the surface. $r_{critical}$ is defined as the equilibrium distance of the particle. For example for argon it is the distance at which the LJ potential becomes its minimum.

Condition 2: Force check:

$$F_{i-Pt} > F_{i-Ar} \tag{3-2}$$

where '*i*' is the particle or atom under consideration in the critical region. The atom meeting the above two conditions is velocity-scaled to the desired surface temperature. No changes are applied to the direction of the atoms. This heating method is validated [40] and found to be very efficient in simulating the physical behavior of liquid and vapor as they come in contact with a heated wall [4, 40] at different temperatures.

This heating algorithm is implemented in the in-house MD code. In order to test this heating algorithm's implementation in the code, we selected a baseline configuration, two thin 3.1 nm

liquid argon films are placed next to the surfaces and a 9 nm argon vapor region in the middle as shown in Figure 3-9. The system is equilibrated for 1000 ps by setting the initial surface temperatures as 90 K.

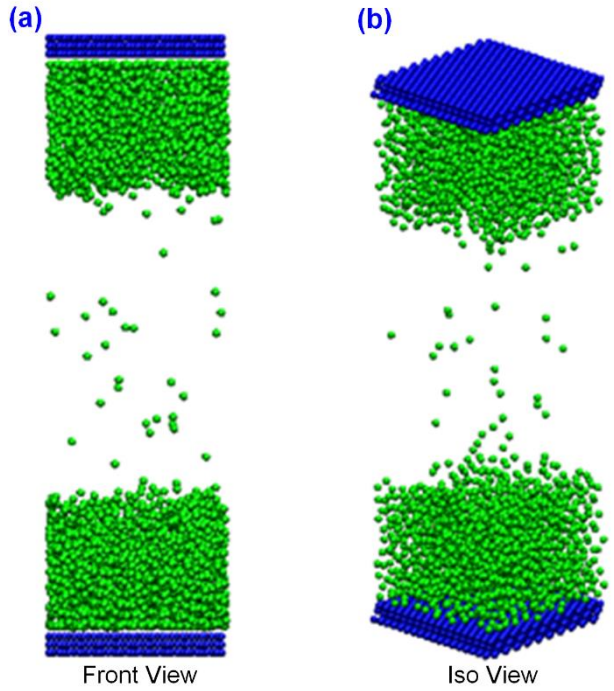

Figure 3-9. Platinum-argon simulation model. (a) Front view of the argon (green) kept on top of platinum walls. (b) Isometric view of the same model.

After equilibration at 90 K, both the surface temperatures are changed to 130 K. The evolution of average temperature of argon is plotted in Figure 3-10. Time elapsed snapshots of the system are shown in Figure 3-11. It shows the equilibration of the argon film with platinum at 90 K followed by heating and reaching a new equilibration temperature of 130 K. The new equilibrium is reached and the liquid films do not completely evaporate as the pressure in the vapor region reaches saturation values.

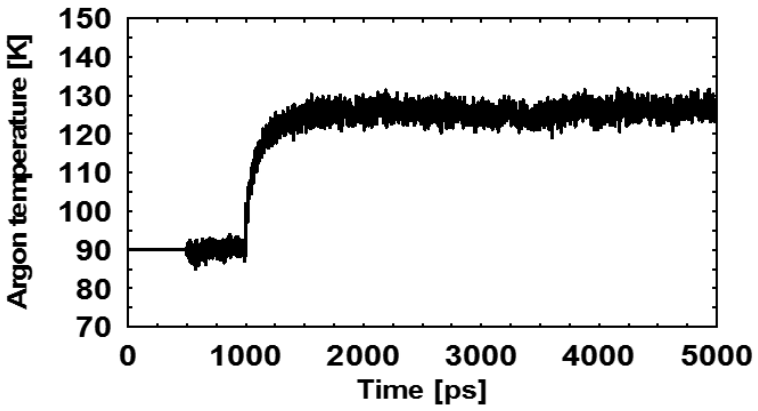

Figure 3-10. Temperature vs. time of top and bottom liquid films

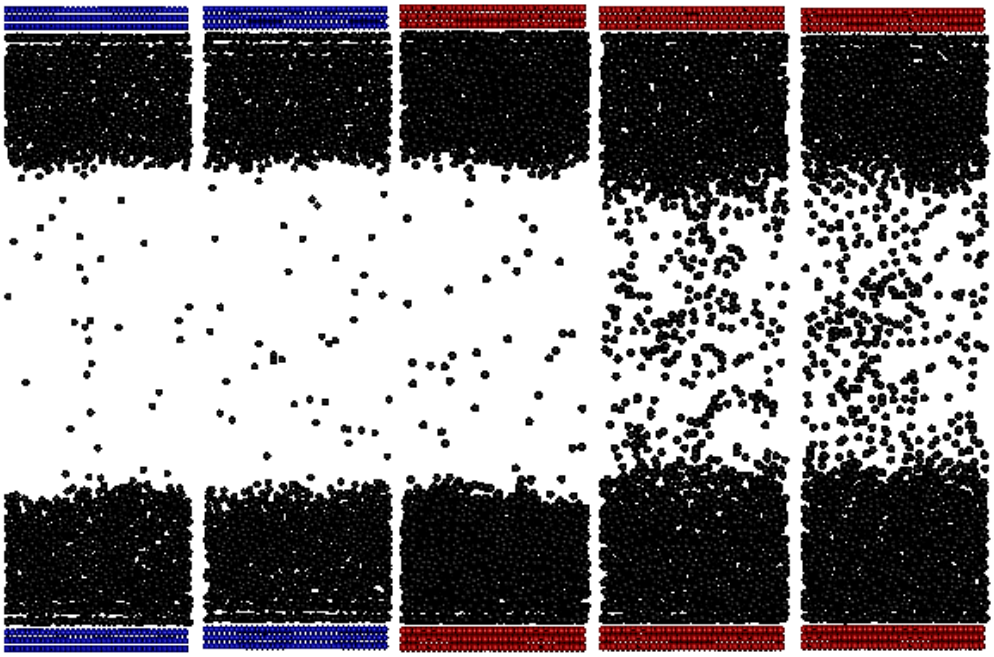

Figure 3-11. Time elapsed screenshot of heating a) Initial b) 500 ps c) 1000 ps d) 2000 ps e) 4000 ps

Next, we demonstrated simultaneous evaporation and condensation at the platinum surfaces. Both platinum surfaces are kept at 90 K and argon system is connected to velocity scaling thermostat for 500 ps. The system is then equilibrated from 500 ps to 1000 ps using the surface heating algorithm, following which the bottom surface is heated to 130 K while the top surface remains at 90 K. The result was an evaporation of argon from bottom surface and condensation at

the top surface as shown in Figure 3-12. The argon starts to evaporate almost immediately after the wall temperature switches to 130 K. The color blue indicates the wall is at 90 K and the color red indicates it is at 130 K. At around 4500 ps argon liquid had almost completely evaporated leaving behind a thin monolayer of atoms. This adsorption is due to the strong force between the surface atoms and the argon atoms.

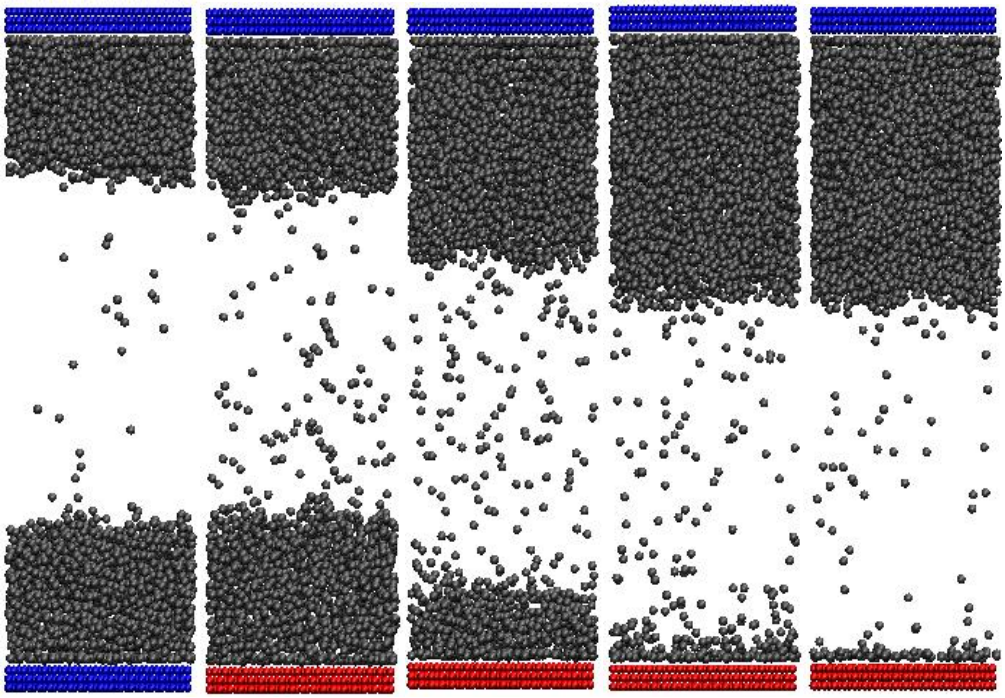

Figure 3-12. Time elapsed screenshot of evaporation a) Initial b) 1500 ps c) 3000 ps d) 4000 ps e) 5000 ps.

3.4 Water Code Validation

3.4.1 Ewald summation

The Ewald summation is a widely used scheme to handle long-range forces like Coulombic forces. The technique of the Ewald summation is to split the slowly converging Coulomb forces into two fast converging components: a real space component and a Fourier space component. The total energy of a Coulombic system can be written as

$$E_{Total} = E_{real} + E_{reciprocal} + E_{intra} + E_{self} \tag{3-3}$$

where the first term on the right hand side is the real space (direct space) contribution of energy, the second term is the Fourier space contribution, the third term represents the energy contribution due to the intramolecular (atomic interaction within the same molecule) interaction, and the last term is a corrective self-energy term.

$$E_{real} = \frac{1}{4\pi\varepsilon_0} \sum_{n}^{'} \sum_{i=1,j>i}^{N} q_i q_j \frac{\operatorname{erfc}\left(\alpha\left|\vec{r}_{ij}+\vec{n}\right|\right)}{\left|\vec{r}_{ij}+\vec{n}\right|} \tag{3-4}$$

$$E_{reciprocal} = \frac{1}{4\pi\varepsilon_0 V} \frac{1}{2} \sum_{k} \frac{4\pi}{\vec{k}^2} \exp\left(-\frac{\vec{k}^2}{4\alpha^2}\right) \left[\left| \sum_{i=1}^{N} q_i \cos\left(\vec{k}.\vec{r}_i\right) \right|^2 + \left| \sum_{i=1}^{N} q_i \sin\left(\vec{k}.\vec{r}_i\right) \right|^2 \right] \tag{3-5}$$

$$E_{Intra} = -\frac{1}{4\pi\varepsilon_0} \frac{1}{2} \sum_{i,j \in M} q_i q_j \frac{\operatorname{erf}\left(\alpha\left|\vec{r}_{ij}\right|\right)}{\left|\vec{r}_{ij}\right|} \tag{3-6}$$

$$E_{self} = \frac{-\alpha}{4\varepsilon_0 \pi^{3/2}} \sum_{i=1}^{N} q_i^2 \tag{3-7}$$

where α is the scaling parameter which decides the weighted contribution to real space and reciprocal space, r is the inter-atomic distance, n is an integer multiple, q is the partial charge, ε_0 is the permittivity of the free space, V is the volume of the domain, and k is the k-space vector.

The corresponding forces are given as

$$F_i^{direct} = \frac{q_i}{4\pi\grave{o}_0}\sum_n\sum_{j=1}^{N} q_j\left[\frac{erfc\left(\alpha\left|\vec{x}_{ij}+\vec{n}\right|\right)}{\left|\vec{x}_{ij}+\vec{n}\right|}+\frac{2\alpha}{\sqrt{\pi}}e^{-\alpha^2\left|\vec{x}_{ij}+\vec{n}\right|^2}\right]\frac{\vec{x}_{ij}+\vec{n}}{\left|\vec{x}_{ij}+\vec{n}\right|^2} \tag{3-8}$$

$$F_i^{reciprocal} = \frac{1}{\varepsilon_0 V}\sum_{k\neq 0} q_i\frac{\vec{k}}{k^2}e^{-\frac{k^2}{4\alpha^2}}\left[\sin\left(k.r_i\right)\sum_{j=1}^{N}\cos\left(k.r_j\right)-\cos\left(k.r_i\right)\sum_{j=1}^{N}\sin\left(k.r_j\right)\right] \tag{3-9}$$

$$F_i^{dipole} = \frac{q_i}{6\varepsilon_0 V}\left[\sum_{j=1}^{N} q_j x_j\right] \tag{3-10}$$

where x is the interatomic distance vector and remaining variables are the same as in the energy equations.

The value of α determines the contribution of the total energy to real and reciprocal space. If α is large, the reciprocal energy will be faster to compute but at the expense of slower real space energy and vice versa. Hence an optimal α is found using the equation below as suggested by Matthey [41].

$$\alpha = \frac{\sqrt{-\ln(\varepsilon)}}{rcut} \tag{3-11}$$

where ε is the accuracy parameter, r_{cut} is the cut off radius. The typical value of ε that we used is 1E-6 and for r_{cut} is 1.0 nm, which makes the α as 4.123. The number of k-vectors can be found by.

$$k_{total} = 2\alpha\sqrt{-\ln(\varepsilon)} \tag{3-12}$$

Even though the Ewald summation is an accurate method, it lacks the computational speed. Thus a few methods have been formulated during the past few decades to improve the computation of reciprocal space energy and force. Smooth Particle Mesh Ewald (SPME) is notable among them and is explained next.

3.4.2 Smooth Particle Mesh Ewald

The Ewald summation method has been studied in detail over the past few decades and many optimizations have been suggested. Among them, one prevalently used is the Smooth Particle Mesh Ewald (SPME) method by Essmann et al. [42]. The idea of SPME is to improve the speed and accuracy in computation of the reciprocal space energy and force term by using Fast Fourier Transform (FFT). The main steps involved are shown below. The reciprocal energy can be rewritten in terms of lattice vectors $\vec{m}$ and structure factors $S(m)$ as given below.

$$E_{reciprocal} = \frac{1}{4\pi\varepsilon_0}\frac{1}{2\pi V}\sum_{m}\exp\left[-\pi^2 m^2 / \alpha^2\right]\frac{S(m)S(-m)}{m^2} \tag{3-13}$$

where the structure factors are defined by

$$S(m) = \sum_{j=1}^{N} q_j \exp\left(2\pi i \vec{m}.\vec{r}_j\right) \tag{3-14}$$

where m is the reciprocal vector defined as $\vec{m} = m_1 a_1^* + m_2 a_2^* + m_3 a_3^*$, and $a_1^*, a_2^* and a_3^*$ represents the reciprocal vectors in x, y and z directions respectively. m_1, m_2 and m_3 are integers but not all zero, $S(-m)$ is the complex conjugate of $S(m)$ and r_i is the position of the partial charge.

In the next step the 3D domain is split into a mesh with N_X , N_Y and N_Z number of divisions in each direction. Each cell which builds such an imaginary mesh system will have sides of *dx, dy* and *dz*. Let u_1, u_2 and u_3 represent the coordinates of an atom in fractional coordinates. i.e., $u_1 = x/dx$

The complex exponential in the structure factor can be then written as

$$\exp\left(2\pi i\, \vec{m}.\,\vec{r}_j\right) = \exp\left(2\pi i \frac{m_1 u_1}{N_X}\right)\exp\left(2\pi i \frac{m_2 u_2}{N_Y}\right)\exp\left(2\pi i \frac{m_3 u_3}{N_Z}\right) \tag{3-15}$$

Further it can be written as

$$\exp\left(2\pi i\frac{m_i u_i}{N_x}\right)=b_i(m_i)\sum_{k=-\infty}^{\infty}M_n(u_i-k).\exp\left(2\pi i\frac{m_i k}{N_x}\right) \tag{3-16}$$

$$b_i(m_i)=\frac{\exp\left(2\pi i(n-1)m_i/N_x\right)}{\sum_{k=0}^{n-2}M_n(k+1)\exp\left(2\pi i m_i k/N_x\right)} \tag{3-17}$$

and M_n is the nth order B-spline polynomial

$$M_n(u)=\frac{u}{n-1}M_{n-1}(u)+\frac{n-u}{n-1}M_{n-1}(u-1) \tag{3-18}$$

Then the structure factor can be written as

$$S(m)=b_1(m_1)b_2(m_2)b_3(m_3)F(Q) \tag{3-19}$$

$F(Q)$ represents the inverse Fourier transform of the charge density matrix *Q*.

$$Q(k_1,k_2,k_3)=\sum_{i=1}^{N}\sum_{n1,n2,n3}q_i M_n(u_{1i}-k_1)M_n(u_{2i}-k_2)M_n(u_{3i}-k_3) \tag{3-20}$$

$$B(m_1,m_2,m_3)=\left|b_1(m_1)\right|^2.\left|b_2(m_2)\right|^2.\left|b_3(m_3)\right|^2 \tag{3-21}$$

$$E_{reciprocal}=\frac{1}{4\pi\varepsilon_0}\frac{1}{2\pi V}\sum_{m\neq 0}\exp\left(-\frac{\pi^2m^2}{\alpha^2}\right)\frac{B(m_1,m_2,m_3).F(Q).F(-Q)}{m^2} \tag{3-22}$$

In this way we can estimate the reciprocal space energy at the computational cost of $O(N\log N)$. The force can be calculated by using Fourier space differentiation called ik-differentiation. The x component of the force using ik-differentiation is obtained as shown in the equation 3-23.

$$\left[Fx\right]_{N_x\times N_y\times N_z}=real\left(F^{-1}\left(1i\times m_x(m_1)4\pi F(Q)(m_1,m_2,m_3)G(m_1,m_2,m_3)\right)\left(N_x\times N_y\times N_z\right)\right) \tag{3-23}$$

Smooth Particle Mesh Ewald is an upgraded version of PME. PME is different from SPME by using Lagrangian interpolation scheme instead of B-splines for charge interpolation.

3.4.3 RATTLE Algorithm

While modeling water as a rigid molecule, the relative motion of intra molecular atoms has to be constrained to avoid very small time integration steps and thereby improves the computational speed. There exists a wide variety of bond constraining methods based on Lagrangian multipliers to achieve this. For MD studies involving water in this thesis, an iterative method called RATTLE [43] is used as a constraint algorithm which is a modified version of SHAKE [44]. This method is compatible with velocity verlet [45] integration scheme. Although SHAKE method is often used by researchers, RATTLE has two advantages over SHAKE. Firstly on computers of fixed precision, RATTLE is of higher precision than SHAKE. Secondly, since RATTLE deals directly with the velocities, it is easier to modify RATTLE for use with the recently developed constant temperature and constant pressure molecular dynamics methods.

The main details of RATTLE algorithm are outlined below. The detailed derivation is not discussed in this thesis, and can be found elsewhere [43].

Let us define

$$\sigma_{ij}\left(r(t)\right)=\left[r_i(t)-r_j(t)\right]^2-d_{ij}^2 \tag{3-24}$$

where r_i is the position of the atom *i*, m_i is the mass of the atom *i*, and d_{ij} is the fixed distance between atoms *i* and *j*. Then the constraint on displacement is expressed as

$$\sigma_{ij}\left(r(t)\right)=0 \tag{3-25}$$

The time derivative of constraint dynamics gives constraint on velocities.

$$\left[\dot{r}_i-\dot{r}_j\right].\left[-r_j\right]=0 \tag{3-26}$$

The equations for constraint dynamics are

$$m_i\ddot{r}_i=F_i+G_i \tag{3-27}$$

where F_i is the force due to intermolecular interactions and intramolecular interactions not associated with constraints. G_i is the force on atom i due to the constraints and given by,

$$G_i = -\sum_j{}' \lambda_{ij} \nabla_i \sigma_{ij} \tag{3-28}$$

where prime denotes a summation over only those atoms j that are connected with atom i by a constraint and the λ_{ij} .are the time dependent Lagrangian multipliers associated with the intramolecular forces of the constraints.

The displacements and velocities are then calculated as

$$r_i(t+h) = r_i(t) + h\dot{r}_i(t) + \frac{h^2}{2m_i}\left[F_i(t) - 2\sum_j \lambda_{RRij}(t) r_{ij}(t)\right] \tag{3-29}$$

$$\dot{r}_i(t+h) = \dot{r}_i(t) + \frac{h}{2m_i}\left[F_i(t) - 2\sum_j \lambda_{RRij}(t) r_{ij}(t) + F_i(t+h) - 2\sum_j \lambda_{RVij}(t+h) r_{ij}(t+h)\right] \tag{3-30}$$

The Lagrangian multipliers $\lambda_{RRij}(t)$ and $\lambda_{RVij}(t+h)$ are chosen to satisfy the constraint equations of displacement and velocities mentioned earlier. They can be solved iteratively by using the method of Ryckaert et al. [44].

3.5 Radial Distribution Function Calculations

Radial Distribution Function (RDF) is a measure of the probability of finding a particle at a distance of '*r*' away from a given reference particle relative to that for an ideal gas. The RDF is usually determined by calculating the distance between all particle pairs and binning them into a histogram. The histogram is then normalized with respect to bulk liquid density.

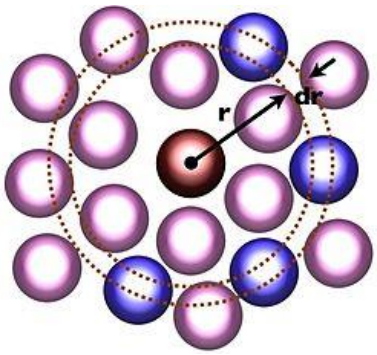

Figure 3-13. Calculation of the radial distribution function in an atomic system. (Image reproduced from Wikipedia)

Mathematically RDF is expressed as,

$$g(r) = 4\pi r^2 \rho dr \tag{3-31}$$

RDFs are a good measure for determining the phase of a substance whether it is in liquid, solid or gas form, as well as comparing simulation RDF data with experimental RDF data. The determination of the RDF is done for the in-house C++ code in which water is implemented. Multiple studies are performed to compare the RDF values of water using Smooth Particle Mesh Ewald [42] and Shift potential, calculated using the in-house code and then compared with the open source MD software GROMACS [21] and experimental results [46].

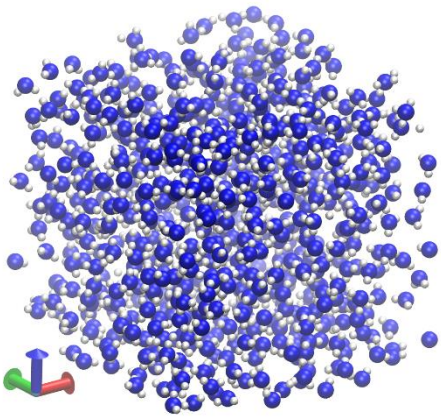

Figure 3-14. Water molecular model for RDF simulations. It consists of 512 SPCE molecules arranged in a cube shape with sides of 3 nm.

A system of 512 water molecules (as in Figure 3-14) is put into in a cubic box at its appropriate density and coupled to the Berendsen thermostat at 300 K. The system is equilibrated for 200 ps followed by estimation of RDF. The reference number density per unit volume of water for different species like oxygen - oxygen and oxygen-hydrogen is found for bulk liquid at 300 K. The number density of each species is then found in a spherical shell volume of $4\pi r^2 dr$, where r is the distance between atoms, and dr is the directional increments to calculate the volume. Finally, the number density is divided with the reference number density to get $g(r)$.

The RDF estimation of liquid water from our code, GROMACS and experiments are shown in the below figures. Table 3-1 and Table 3-2 show the comparison of the results with respect to the different potential schemes, software and experimental values, good agreement obtained, thus validating the implementation of the various modules of code for water simulation using MD.

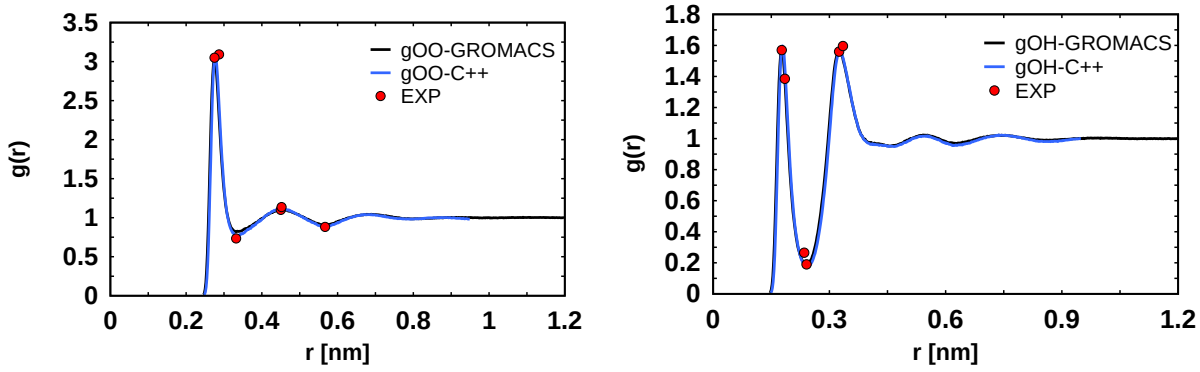

Figure 3-15. RDF comparison for Oxygen-Oxygen and Oxygen-Hydrogen from our C++ code, GROMACS and from experiments.

Table 3-1. Radial distribution function values for oxygen-oxygen

g_{OO}	First Peak		First Trough		Second Peak		Second Trough	
	r(nm)	g(r)	r(nm)	g(r)	r(nm)	g(r)	r(nm)	g(r)
Mark & Nilsson 2001	0.275	3.05	0.335	-	0.45	1.10	0.568	-
GROMACS-SPME	0.274	3.046	0.332	0.818	0.45	1.108	0.558	0.905
C++ code-shift	0.277	3.076	0.333	0.778	0.453	1.11	0.567	0.89
C++ code-SPME	0.273	3.056	0.327	0.793	0.450	1.111	0.569	0.899
Experiment (Soper 1986 [46])	0.287	3.092	0.332	0.734	0.452	1.136	0.567	0.882

Table 3-2. Radial distribution function values for oxygen-hydrogen

g_{OH}	First Peak		First Trough		Second Peak	
	r(nm)	g(r)	r(nm)	g(r)	r(nm)	g(r)
Mark & Nilsson 2001	0.177	1.57	0.241	0.19	0.325	1.56
GROMACS-SPME	0.176	1.583	0.240	0.191	0.324	1.564
C++ code-shift	0.179	1.593	0.243	0.175	0.327	1.558
C++ code-SPME	0.175	1.573	0.239	0.183	0.325	1.557
Experiment (Soper 1986 [46])	0.185	1.385	0.235	0.265	0.335	1.596

3.6 Contact Angle Algorithm

Contact angle estimation of a liquid droplet on a solid surface plays an important role to understand the solid-liquid wetting properties, capillarity and surface interaction energy. While studying the droplet on a surface using molecular dynamics (MD) simulations, the main challenge lies in separating the liquid and vapor phases, and estimating the interface, curvature and contact angle. Further, during transient MD simulations, large amount of data processing is required for calculating the time evolution of contact angle. This is an error prone and a strenuous effort to do manually or with image processing algorithms and can affect the contact angle results.

In the past, Bo Shi et al. [47] simulated the contact angle of water on top of FCC 111 platinum surface by simulating columbic potential with P3M method [48] and maintaining the temperature constant using Berendsen thermostat [22]. But the method of contact angle estimation was not mentioned. Kandlikar et al. [49] have performed contact angle studies of water on platinum with truncated potential, in which the method of estimating the contact angle was not mentioned. Barisik and Beskok [50] have done the surface interaction studies of silicon and water while considering the line tension. Erik et al. [51] smeared the molecules into a grid using the Nearest Grid Point (NGP) scheme. In another work, Malani et al. [52] demonstrate a new method called float method, which obtains the contact angle from a reverse methodology (solid beads floating on liquid) and identifying the interface using the Gibbs method. This method is dependent on the assumption that the geometry has a predicted curvature. Sergi et al. [53] calculated the contact angle of water from MD using local averaging and fitting methods. In addition, a wide range of studies on contact angle estimation using MD simulations exists [54-57]. Most of the researchers have focused on finding the contact angle and surface energy through various techniques; however, the majority use NGP scheme as the basic method to predict the liquid-vapor interface, which has certain drawbacks as explained later in this work.

To address this concern, we have developed an improved version of the contact angle estimation algorithm. This algorithm segregates the droplet molecules from the vapor molecules using Mahalanobis distance [58] (MND) technique, after which the density is smeared onto a 2D grid using various interpolation functions. The smearing is done by rotating the droplet multiple times at different angles to attain more interfacial data points. The liquid-vapor interface data is estimated using density filtering from the grid. With the interface data, a circle is accurately fitted using Landau method. The equation of this circle is solved for obtaining the contact angle. We applied this algorithm to study the hydrophilic and hydrophobic contact angles for argon and water droplets on a platinum surface with varying interaction potential parameters leading to different wettability conditions, as well as contact angle evolution of water droplet on a platinum surface.

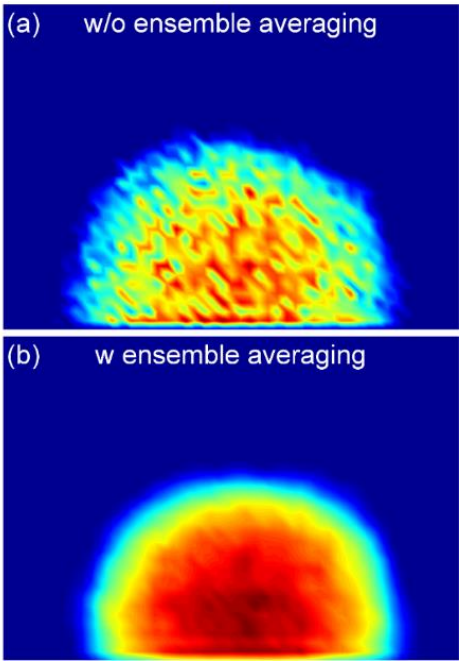

Figure 3-16 The need for ensemble averaged datasets. (a) Original data from MD simulation without averaging over time. (b) Data averaged over 500 steps and plotted using smooth function.

The estimation of the contact angle from a single data set without averaging over time may result in poor data generation and can yield incorrect results. This drawback is shown in Figure

3-16a, b. Further, due to the enormous amount of resulting MD data, the estimation of the contact angle using image recognition algorithms or manual methods becomes very strenuous and results can vary significantly.

The main contents of the algorithm are divided into three main parts: 1) explaining the algorithm used for estimating the contact angle; 2) the application of the algorithm in MD simulations for static contact angle determination of argon and water droplets on a platinum surface; and 3) the contact angle evolution of water droplet on a platinum surface.

The contact algorithm is divided into five phases: 1) Initial filtering using cutoffs and the Mahalanobis method, 2) Density smearing using different interpolation techniques, 3) Density filtering and monolayer removal, 4) Data fitting to circle or appropriate curves, and 5) Solving for contact angle.

3.6.1 Phase 1: Mahalanobis Filtering

Often MD simulation trajectory results of water, argon and other liquids have the information (coordinates and velocities) of co-existence of vapor and liquid depending on the temperature. Compared to density based filtering, segregating the liquid droplet or liquid molecules from the vapor molecules using Mahalanobis filtering will avoid false detection of a liquid-vapor boundary. Although this step is optional, it will give more informative data for estimating the contact angle and will save computational time in the later phases of the algorithm. The unwanted vapor molecules (outliers) in the data can be removed effectively using a combination of the Mahalanobis Distance [59] technique and cutoff schemes. If X_c is the $n\times 2$ column centered vector consisting of $\left(x-\bar{x}, y-\bar{y}\right)$ data of *n* points, then the variance-covariance matrix C_x is defined as:

$$C_x = \frac{1}{(n-1)}(X_c)^T (X_c) \tag{3-32}$$

The Mahalanobis Distance (MND) is calculated as:

$$MND_i = \sqrt{X_i C_x^{-1} X_i^T} \tag{3-33}$$

where X_i is the mean centered data of i^{th} data point. From this list of MND, we can neglect those data points with considerably high MND values. The main advantage of the MND technique over conventional outlier removal methods is the data is arranged at equal standard deviations instead of equal Euclidean distance, which provides initial filtering of vapor and far away molecules from desired droplet. The use of MND filtering along with a conditional cutoff along vertical direction is shown in Figure 3-17. Figure 3-17a shows data from an MD simulation of argon droplet on platinum.

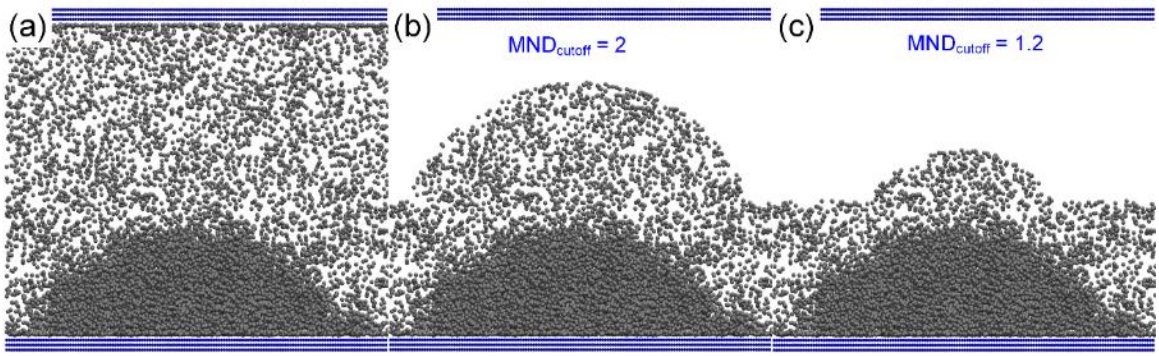

Figure 3-17 Mahalanobis filtering method. (a) Original data from MD simulation. (b) Filtered data using a Mahalanobis (MND) cutoff of 2 (c) Filtered data using a Mahalanobis (MND) cutoff of 1.2. A wisely chosen MND cutoff can remove significant amount of vapor molecules, which will save computational time for phase 2 of the algorithm.

Figure 3-17b and Figure 3-17c show the filtered data using MND filtering with MND cutoff of 2 and 1.2 respectively along with a conditional z-axis cutoff to atoms above 7 nm which represents the expected height of droplet. The suggested value of MND cutoff is in the range of 1 to 2.5. The main purpose of this phase is to remove unnecessary data for faster phase 2 operation.

3.6.2 Phase 2: Density smearing using interpolation functions

In this phase, a 2D mesh in the XZ plane (X-horizontal and Z-vertical) is generated and the entire droplet density information is projected and smeared into the grids using an interpolation function. This data is used to find a smooth transition between the liquid core and the vapor (or vacuum). The user can choose any interpolation function for this purpose. Here we discuss three different types of functions for interpolation and their effectiveness in contact angle estimation.

The first one is the simple Nearest Grid Point (NGP) method, which is a traditional first order method that researchers normally use to assign data to the grid points. Inspired from Hockney and Eastwood [60] version of the NGP scheme, the density of the atoms at every grid point using NGP scheme can be calculated by using the equation:

$$\rho_{ij} = \sum_{p=1}^{N} W\left(\frac{\left|x_i - x_p\right|}{dx}\right) * W\left(\frac{\left|y_i - y_p\right|}{dy}\right) \tag{3-34}$$

where the weight function is defined as:

$$W(x) = \begin{cases} 1, & x < \frac{1}{2} \\ 0, & \text{otherwise} \end{cases} \tag{3-35}$$

The second type of interpolation function is the cardinal B-spline function. We have used the fourth order version used in Smooth Particle Mesh Ewald [42]. Reproducing the definition of B-splines, for any real number *u*, let $M_2(u)$ denote the linear hat function given by $M_2(u) = 1 - |u - 1|$ for $0 \le u \le 2$ and $M_2(u) = 0$ for $u < 0$ or $u > 2$. For *n* greater than 2, define $M_n(u)$ by the recursion:

$$M_n(u) = \frac{u}{n-1} M_{n-1}(u) + \frac{n-u}{n-1} M_{n-1}(u-1) \tag{3-36}$$

For our case *n* = 4 and *u* is in fractional coordinates, which are evenly spaced.

The third type of interpolation function is similar to the smooth functions used for Hardy stress [61] estimation. We have developed a quadratic function which is:

$$w(r) = \frac{2\left(1 - r^2 / r_s^2\right)}{B\pi r_s^2} \tag{3-37}$$

where $r = \sqrt{rx^2 + ry^2}$, $rx = x_i - x_p$ and $ry = y_i - y_p$ are the differences between the position of i^{th} atom and p^{th} grid point, r_s is the spread radius and B is the depth of the system along Y-axis.

The atomic trajectories obtained from the MD simulations will have tiny vacuum like holes (due to van der Waals radius) in the interatomic spacing region which will give a checkered appearance to the density data. Thus, for any of the above mentioned interpolation functions, we suggest an additional boosting of the density by creating more data by rotating the droplet along the Z-axis and projecting to XZ plane (X-horizontal and Z-vertical). This step will capture the droplet shape fluctuations from all the possible sides. The rotation of the mean centered data is obtained by multiplying the rotation matrix as shown below:

$$R = \begin{bmatrix} \cos\theta & -\sin\theta \\ \sin\theta & \cos\theta \end{bmatrix} \tag{3-38}$$

where θ is the angle of rotation which ranges from 0 to π. The resulting density images are shown in Figure 3-18. Figure 3-18a shows the original data from MD simulation. Figure 3-18b, c and d show the 2D density obtained in the XZ plane (X-horizontal and Z-vertical) using NGP, B-spline and Hardy's interpolation methods respectively.

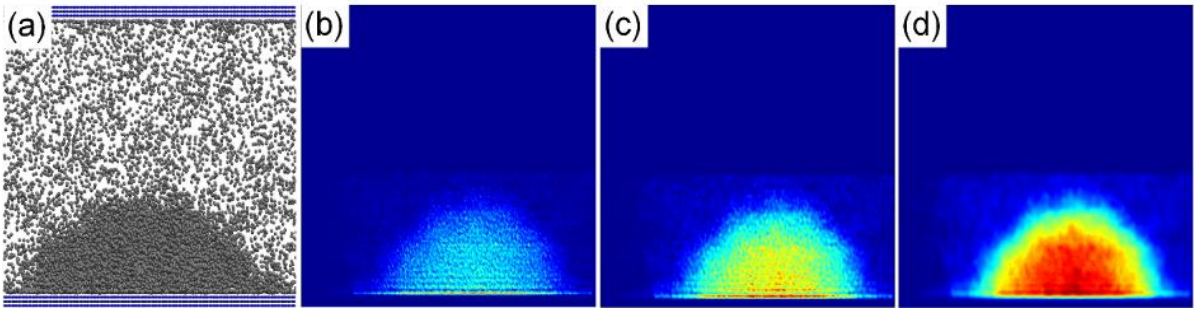

Figure 3-18 Comparison of different density calculation schemes. (a) Sample argon droplet on platinum surface. The system consists of two parallel plates confining the argon droplet and its vapor at a temperature of 105 K. (b) Two dimensional (2D) density calculated using Nearest Grid Point (NGP) approach. (c) 2D density calculated using B-splines functions. (d) 2D density calculated using Hardy's approach with a quadratic function

From the comparison of these images we can see that the Hardy's interpolation scheme shows a strong and smooth representation of the density of the droplet. We found from our studies that both B-splines and Hardy functions serves the best purpose for density smearing and in turn, best identifies the liquid-vapor interface.

3.6.3 Phase 3: Density based filtering

Phase 2 will result in a 2D density data of the droplet. In this phase, we identify the most probable liquid vapor interface using density filtering. Mathematically, this concept is explained using equation 3-39 below. This step will remove the grid points with high densities which resemble the liquid core region and low densities that resemble the vapor (noise), and thus we will be left with the interfacial data.

$$\text{Threshold}_{MIN} \leq \text{Grid.density} \leq \text{Threshold}_{MAX} \tag{3-39}$$

$$\text{Threshold}_{MAX} = w_1.\text{Maxdensity} \tag{3-40}$$

$$\text{Threshold}_{MIN} = w_2.\text{Maxdensity} \tag{3-41}$$

$w1$ and $w2$ are weights which can be fine-tuned according to the data. For the present studies we have taken them as 0.2 and 0.1 respectively. Before moving to the next phase, we may have to remove the monolayer (a high density layer formed just above the surface) information just by defining a data filter $z < z_{cutoff}$ where z_{cutoff} represents the location above the surface within which we find the monolayer and other high dense layers which are affected by the strong wall atomic interaction and do not contribute to the shape of the droplet. For our studies, we have chosen it to remove the first two layers above the surface.

3.6.4 Phase 4: Fitting the interface to a function

The data from phase 3 will represent the most probable liquid vapor interface related to the droplet. The next step is to fit this using an appropriate function that makes physical sense. We have a variety of choices including circle, ellipse and polynomials. Unless it is an impinging or moving droplet, the shape of the droplet will be similar to a circle. Therefore, we only discuss the cases with circle fitting. Circle fitting can be very accurate when using the Landau method [62]. The Landau method relies on minimizing the error of fit between the set of points and the estimated arc through a non-iterative geometric fit. The main equations for this method are mentioned below. For a detailed version and nomenclature, readers are encouraged to see the original reference [62].

$$\bar{x} = \frac{c_1 b_2 - c_2 b_1}{a_1 b_2 - a_2 b_1} \tag{3-42}$$

$$\bar{y} = \frac{a_1 c_2 - a_2 c_1}{a_1 b_2 - a_2 b_1} \tag{3-43}$$

$$R^2 = \frac{1}{N}\left[\sum x^2 - 2\sum \bar{x} + N\bar{x}^2 + \sum y^2 - 2\sum \bar{y} + N\bar{y}^2\right] \tag{3-44}$$

The variables used in above equations are given by

$$a_1 = 2\left(\left(\sum x\right)^2 - N\sum x^2\right) \tag{3-45}$$

$$a_2 = 2\left(\sum x\sum y - N\sum xy\right) \tag{3-46}$$

$$b_1 = 2\left(\sum x\sum y - N\sum xy\right) \tag{3-47}$$

$$b_2 = 2\left(\left(\sum y\right)^2 - N\sum y^2\right) \tag{3-48}$$

$$c_1 = \left(\sum x^2\sum x - N\sum x^2 + \sum x\sum y^2 - N\sum xy^2\right) \tag{3-49}$$

$$c_2 = \left(\sum x^2\sum y - N\sum y^3 + \sum y\sum y^2 - N\sum x^2 y\right) \tag{3-50}$$

where x and y are the coordinates of the data points and N is the number of data points.

From these equations, the center of the circle and radius are obtained. If the center is above the surface then the droplet is hydrophobic, else it will be hydrophilic. Further, if the center location above the surface is greater than the radius, then the droplet is freely floating and not touching the surface.

3.6.5 Phase 5: Estimating the contact angle

After the equation of circle is determined, the contact angle can be estimated by using the series of equations given below. The equation of the circle from phase 4 is shown graphically in Figure 3-19 and is given by

$$\left(\mathrm{x} - \mathrm{x_c}\right)^2 - \left(\mathrm{z} - \mathrm{z_c}\right)^2 = \mathrm{R}^2 \tag{3-51}$$

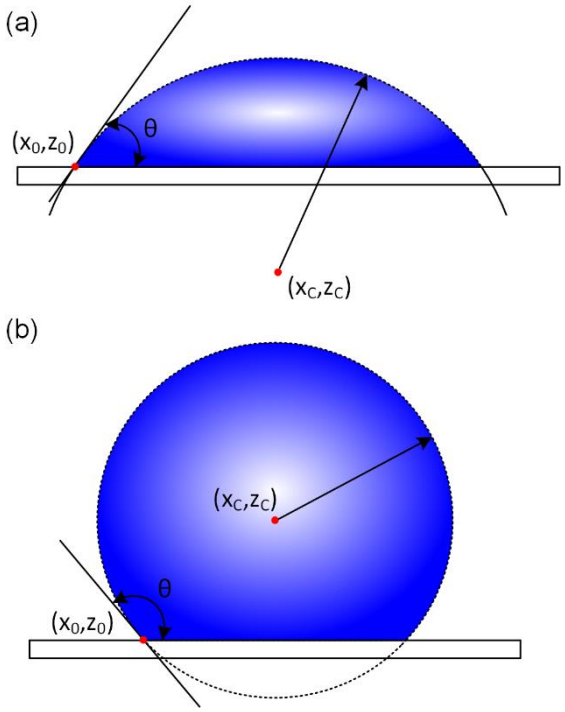

Figure 3-19 Estimation of contact angle from the interfacial data (a) location of circle center and contact angle for hydrophilic surface (b) location of circle center, contact angle for hydrophobic surface.

Consider the equation of line which represents the cutoff along the Z axis to remove the monolayer

$$z = Z_{cutoff} = z_0 \tag{3-52}$$

Slope of equation of circle at any point is given by

$$2\left(x - x_c\right) - 2\left(z - z_c\right)\frac{dz}{dx} = 0 \tag{3-53}$$

Slope at $z = Z_{cutoff} = z_0$ is given by

$$m_0 = \left.\frac{dz}{dx}\right|_{x_0, z_0} = \frac{\left(x_c - x_0\right)}{\left(z_{0-z_c}\right)} \tag{3-54}$$

where x_0 is solved as

$$x_0 = x_c - \sqrt{R^2 - \left(z_0 - z_c\right)^2} \tag{3-55}$$

Contact angle is then obtained for hydrophilic surfaces ($z_c < z_0$) by

$$\theta = \tan^{-1} m_0 \tag{3-56}$$

For hydrophobic surfaces ($z_c > z_0$) contact angle is given by

$$\theta = \pi + \tan^{-1} m_0 \tag{3-57}$$

The identification of hydrophobic or hydrophilic surfaces is simply based on the location of the circle center as shown in Figure 3-19a and b.

3.7 Contact Angle Studies

3.7.1 Static contact angle estimation studies

A series of Molecular Dynamics (MD) simulations are performed to estimate the contact angle using the aforementioned algorithm. For water droplet simulations, a cube shaped water droplet with 5 nm sides (4098 water molecules or 12294 atoms) is kept on top of a single layered platinum wall. For argon droplet simulations, an equilibrated 6 nm^3 argon droplet is placed over a 3 layered FCC 111 platinum wall. The side boundaries are periodic while the top boundary has another platinum surface similar to the lower wall. The fluid (argon or water) – platinum interaction is through LJ potential.

The simulations are performed using GROMACS software [21]. The main objective behind this section is to validate the contact angle algorithm and so we used GROMACS instead of our C++ code. The platinum surfaces are modeled with FCC 111 structure and are square shaped with sides of 20 nm. The platinum surfaces are kept apart at a distance of 16 nm for argon studies and at 10 nm for water droplet studies. The temperature of the system is kept constant using velocity re-scale thermostat as 105 K for argon drops and 300 K for water droplets. The MD simulation is then performed for 1000 ps for system equilibration. The equations of motions are

solved using velocity verlet scheme with a time step of 5 fs for argon and 2 fs for water. The shifted Lennard Jones (LJ) scheme suggested by Stoddard and Ford [63] with 1.1 nm was used. The feature of this potential is that both potential and force go smoothly to zero at the cut off radius.

$$U(r) = 4\varepsilon\left\{\left[\left(\frac{\sigma}{r}\right)^{12} - \left(\frac{\sigma}{r}\right)^{6}\right] + \left[6\left(\frac{\sigma}{rc}\right)^{12} - 3\left(\frac{\sigma}{rc}\right)^{6}\right]\left(\frac{r}{rc}\right)^{2} - 7\left(\frac{\sigma}{rc}\right)^{12} + 4\left(\frac{\sigma}{rc}\right)^{6}\right\} \quad (3\text{-}58)$$

The water molecules are modeled using SPCE model introduced by Berendsen et al [63]. The intra molecular bonds are kept rigid throughout the simulation using the LINCS algorithm [64].

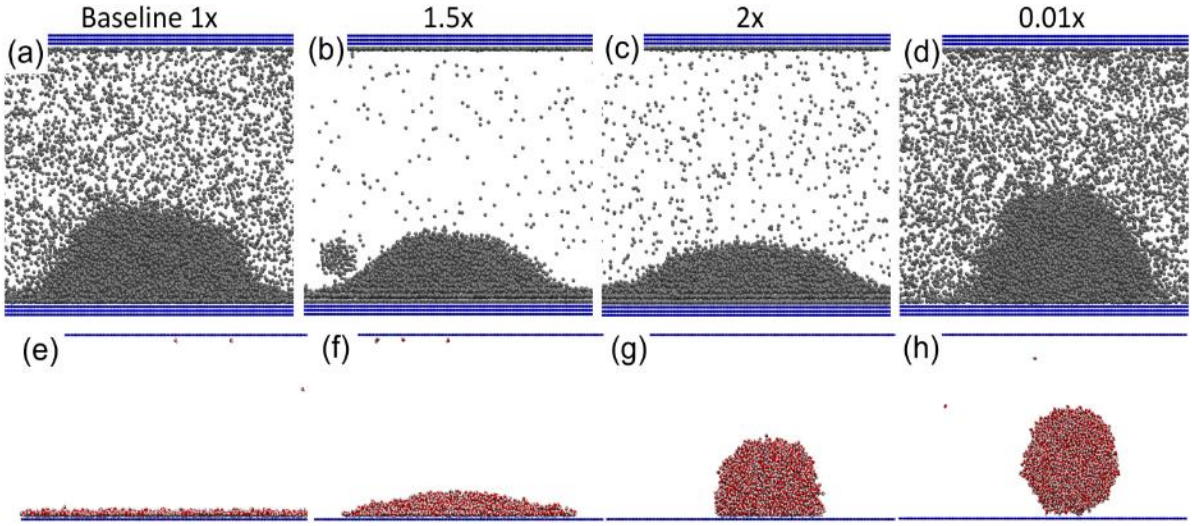

Figure 3-20 Different scenarios in molecular dynamics (MD) simulations of argon - platinum and water - platinum wettability studies. (a-d) Argon droplet on top of three layered platinum wall with varying Lennard Jones (LJ) parameters as shown in Table 3-3, cases 1 to 4. Baseline 1x refers to the baseline case 1 in Table 3-3. The 1.5x, 2x and 0.01x represent the strength of attraction compared to baseline case. (e-h) Water droplet on top of single layered platinum with varying Lennard Jones (LJ) parameters as shown in Table 3-3, cases 1 to 4.

The LJ potential parameters for argon – platinum and water – platinum are altered as shown in the table 1 to obtain hydrophilic and hydrophobic surfaces. Figure 3-20a, b, c and d shows the equilibrated argon droplets for cases 1, 2, 3 and 4 of Table 3-3. Figure 3-20e, f, g and h shows the

equilibrated water droplets for cases 1, 2, 3 and 4 of Table 3-3. These cases are studied using the developed algorithm and the resulting contact angles are tabulated in Table 3-4.

Table 3-3 Lennard Jones properties for different cases of study

	Argon – Platinum		Water – Platinum	
	$\sigma_{Ar-Pt}[nm]$	$\varepsilon_{Ar-Pt}\left[kJ/mol\right]$	$\sigma_{OW-Pt}[nm]$	$\varepsilon_{OW-Pt}\left[kJ/mol\right]$
Case 1	0.294	7.116	0.283578	3.923032
Case 2	0.294	10.674	0.283578	2.615355
Case 3	0.294	14.232	0.283578	1.307677
Case 4	0.294	0.071	0.283578	0.326919

Table 3-4 Contact angles of different cases (see Table 3-3) of water and argon on platinum

	Argon – Platinum	Water – Platinum
	$\theta[deg]$	$\theta[deg]$
Case 1	66.9	0
Case 2	46.71	14.9
Case 3	33.8	95.6
Case 4	83.09	148

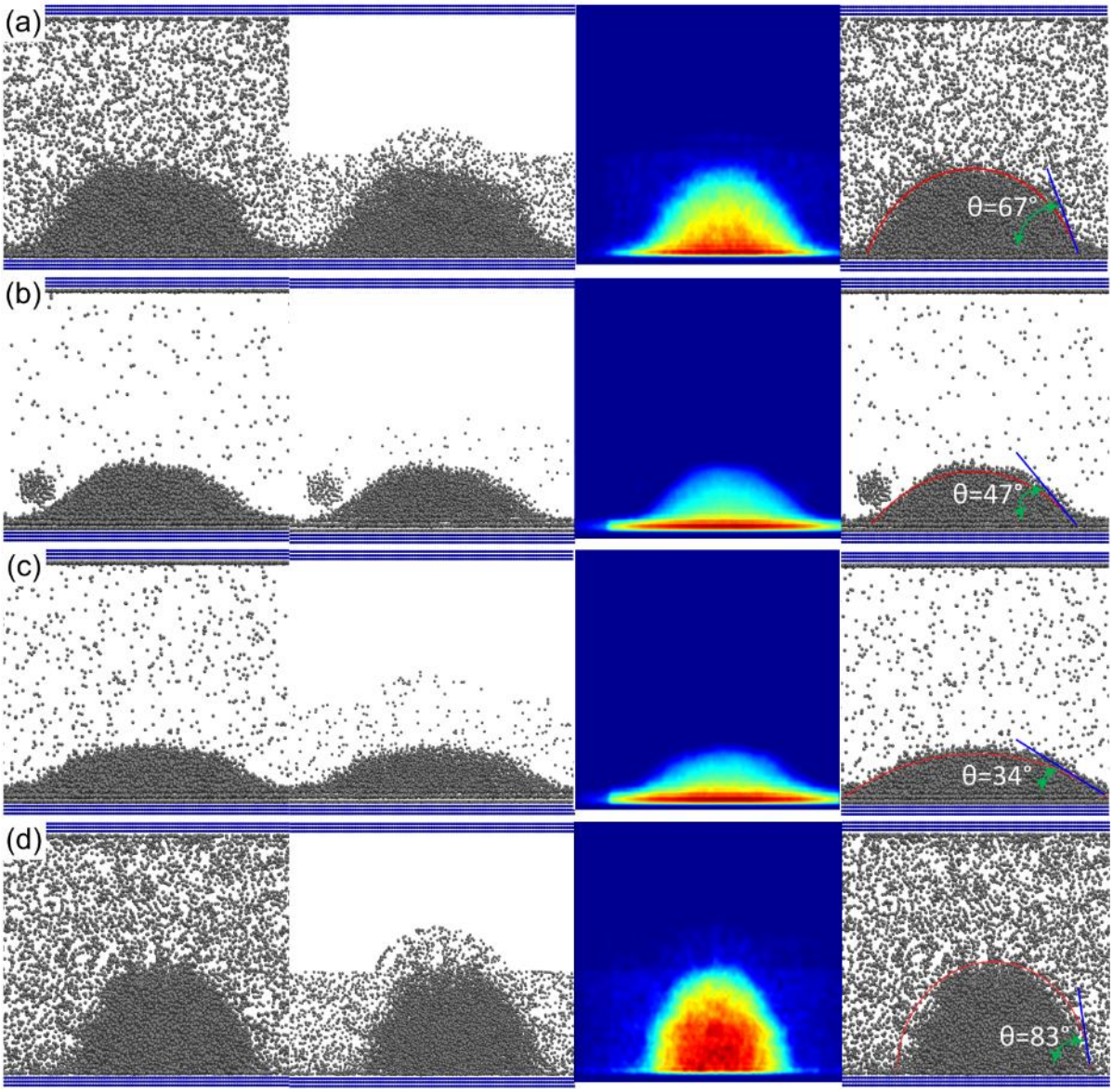

Figure 3-21 Sequence of identifying the liquid vapor interface and contact angle estimation. (a-d) Panel rows indicate different cases from 1 to 4 as shown in table 1. Panel column 1 indicates the original data from MD simulations. Column 2 shows the result of pass 1 (Mahalanobis filtering) as described in the paper. Column 3 shows the pass 2 (density smearing) using Hardy quadratic function. Column 4 shows the final identified circular shape of water droplet superimposed on original droplet data. The case 4 can have a better fit if we consider an ellipse fit which can be added to phase 5

The various phases of algorithm are visually shown in Figure 3-21a-d. The panel columns show the different phases of algorithm, and the panel rows of Figure 3-21 shows the different cases

(cases 1 to 4 from Table 3-3) for argon droplets. The first column is the equilibrated droplet from MD simulation, the second column is the Mahalanobis filtered data, the third column shows the 2D density smeared using quadratic Hardy function and the last column shows the identified interface along with the original data.

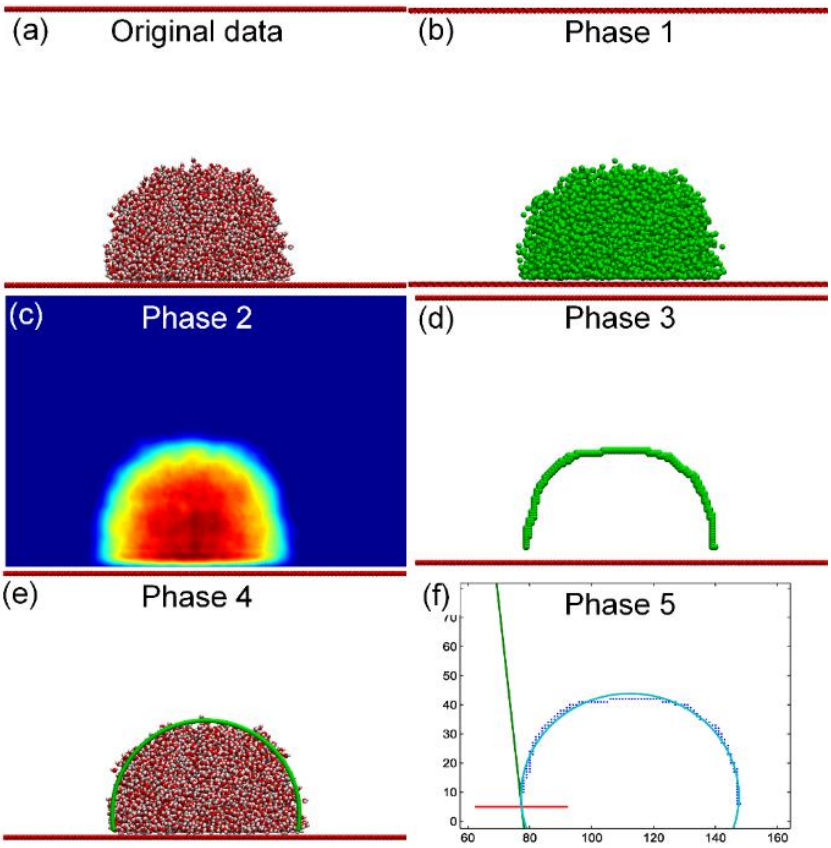

Figure 3-22 Sequence of identifying the liquid vapor interface and contact angle estimation. (a) Original data from the MD simulation (b) Data after applying the phase 1 criteria, the Mahalanobis filtering (c) data smeared into the 2 dimensional grid (phase 2) using Hardy's quadratic polynomial (d) density filtered data (phase 3) using simple threshold cutoff (e) circle fitted using Landau method (phase 4) and overlapped with original data and (f) solving the equation of circle and line to get contact angle.

A step by step visualization of various phases of the algorithm is shown in Figure 3-22. Figure 3-22a shows the original water droplet from the MD simulation. The Figure 3-22b shows the data after Mahalanobis filtering (Phase 1), Figure 3-22c shows the density smearing (Phase 2),

Figure 3-22d represents the data after applying density filtering and monolayer removal (Phase 3), Figure 3-22e shows the fitted circle with original data on background (Phase 4), and Figure 3-22f shows the contact angle calculation (Phase 5).

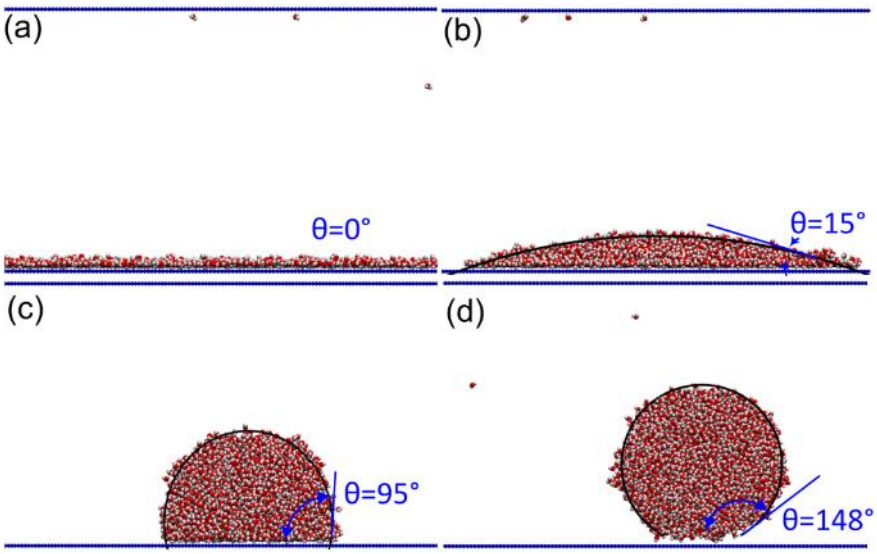

Figure 3-23 MD simulation results of water droplet on different surfaces based on the surface interaction parameters mentioned in Table 3-3 and estimated interface (as thick black line) and contact angle values for (a) super-hydrophilic surface, (b) hydrophilic surface, (c) hydrophobic surface, and (d) super-hydrophobic surface.

The identified liquid – vapor interface of water is shown in Figure 3-23a, b, c and d. We can see the effect of varying hydrophobicity based on the interaction parameters mentioned is Table 3-3. Thus, the developed algorithm can accurately estimate the contact angle for non-polar and polar liquids.

3.7.2 Contact angle Evolution with time

The evolution of contact angle can be captured with the developed algorithm. In order to present this aspect, we performed MD simulations of water droplet on the platinum surface and

estimated the contact angle evolution of the drop from its initial state. Two main cases of MD simulations were performed:

A cube shaped water droplet with 6 nm sides (7221 molecules) is kept on top of platinum wall interacting using LJ-potential. The sides are under periodic boundary condition and the top boundary is covered with another platinum surface to prevent the escape of molecules. These simulations are performed using GROMACS software, as the focus was on the contact angle algorithm and not on the custom made MD modules. The platinum surfaces are modeled with FCC 111 structure and are square shaped with sides of 25 nm. The platinum surfaces are kept apart at a distance of 14 nm. The water is modeled as SPCE molecules with σ as 0.3166 nm and ε as 1.0793×10^{-21} J and the water-platinum parameters are calculated using the geometric mean method [26]. There are three sub cases for this model based on the thermostat used. They are Berendsen [22], Nose-Hoover [20] and Velocity re-scale [65] thermostats. The simulation is performed from 0 ps to 1000 ps. A shifted scheme suggested by Stoddard and Ford, as described in [39], was used.

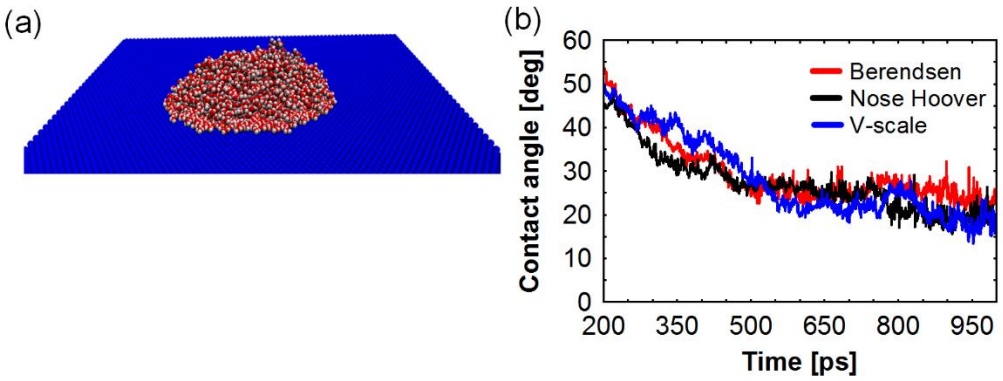

Figure 3-24 Contact angle evolution studies. (a) Equilibrated water droplet on platinum plate (b) case 1 water platinum interaction using regular LJ potential

For all simulation in Case 1, we equilibrated the system at 300K for 200 ps. From 200 ps to 1000 ps we ran the system to generate production run data. At the end of simulation the trajectory

files are processed and contact angles are determined using the algorithm mentioned in the first part of this work. The time evolution of contact angle is shown in Figure 3-24b. As expected, the contact angle fluctuates and decreases in time as the initial cubic shape of the droplet is lost. This kind of the study is important to show the use of algorithm to track the contact angle of the droplet under changing thermodynamic parameters like temperature or surface interaction parameters. The steady state contact angle is determined to be 25-30^{o} by averaging the values from 600 ps to 1000 ps, which is in good agreement with experimental value [49]. These simulations show that the developed algorithm can adequately estimate the contact angle evolution with time.

4 Pressure Estimation in Two Dimensions

Multiscale coupling of atomistic and continuum simulations is of significant importance in the areas of heat transfer, fracture mechanics and bioengineering [66]. These computations typically map properties determined from atomistic simulations onto grid points in continuum simulations [67]. Among them, a very important property is the estimation of pressure or stress in the atomistic system, which is used for interfacial energies and surface tension, pressure gradients in fluid simulations and lipid bilayer mechanics. This chapter focuses on the two-dimensional pressure and surface tension estimations of multiphase systems. Development of these modules are crucial in understanding and estimating thermodynamic variables near the surface while performing passive flow simulations.

We will first give a brief introduction about the existing methods to estimate local pressure and its applications, followed by pressure estimations for 3D and 1D grids from molecular dynamics simulations. Later in the chapter we will derive the formula for direct estimation of pressure on 2D grids which is much faster than 3D. This method is then validated by applying it to suspended film of argon and droplet of argon.

4.1 Present Methods for Local Pressure Estimation

The atomic level virial stresses from statistical analysis were first derived by Irving and Kirkwood [68], now generally referred to as the IK method. The need for large ensemble averaging due to the delta function in IK method was circumvented by Hardy in his classical paper [61, 69] by introducing a spreading function and a bond function. The virial stress has two components, a kinetic component and a force component. Ambiguity exists among researchers regarding the equivalence of virial stress with Cauchy stress. The ambiguity is thoroughly discussed in Zhou's

paper [70] which claimed that Cauchy stress is not equivalent to virial stress, as the continuum level Cauchy stress is equivalent only to the force component of virial stress. Based on this finding, researchers [71-74] performed a number of molecular studies. Zimmerman [71] showed that, for crystals, Hardy's stress formulation gave more accurate results than simple local virial averages. A comparative study of different versions of local virial stress was studied by Murdoch [75]. In contrast to Zhou's work [70], Subramaniyan [76] found that virial stress is indeed the Cauchy stress using specific examples. There were other works [77, 78] which tried to develop the appropriate relation of virial stress and continuum level stresses. A generalized method for stress calculations, which included temporal averaging weight functions were derived by Yang [79]. Recently, Vanegas [80] and Sanchez et al.[81] applied the modified Hardy versions of IK stress to lipid bilayers, coiled coil protein, and graphene sheet to determine continuum level properties from atomistic simulations.

Most of the available literature on local pressure estimation is based on 3D [82] or 1D [83-85] pressure estimation and not on 2D grids. These studies apply three dimensional (3D) pressure calculation methods smeared into grids, which is extremely computationally expensive [80] as it involves a 3D convolution. The computational cost associated with the 3D pressure estimation is qualitatively discussed in the section 4.3. However, many molecular systems do not inherently require a 3D pressure distribution estimation. For example, many practical systems have inhomogeneity only in one or two dimensions and thus only need 1D or 2D pressure distribution respectively. A few Irving-Kirkwood versions [61, 86, 87] of 1D pressure calculations exist in the literature for 1D inhomogeneous system. In the next sections, we will show the development and validation of a 2D pressure estimation algorithm based on Hardy's stress method.

4.2 Development of 2D Pressure Formulae

Here, we term the modified version of IK stress developed by Hardy [61] as 'Hardy pressure' which has a kinetic component and a virial component. The 3D pressure estimation methodology consists of smearing the kinetic and the virial component onto a 3D grid using a weight function and a bond function respectively. The components are smeared onto a spherical volume around the particle location. A typical weight function, as used by researchers [77, 79] for 3D grid, is given as:

$$w(r) = C_1\left[1 - 3r^2 / r_s^2 + 2r^3 / r_s^3\right] \tag{4-1}$$

where C_1 is the constant of integration, r is the distance between an atom and a grid point, and r_s is the spread radius. Spread radius is the radius of the circle of influence of grid points. For example, if spread radius is 0.5 nm, then the atoms within 0.5 nm radius is smeared into a grid point. A sensitivity study and details of the typical values that we have chosen for the simulations are mentioned in section 4.4.2.

Our 2D pressure estimation method is developed by reformulating the weight function which will significantly reduce the computational cost without losing any desired details in the results. Specifically, a 3D pressure method requires $N^2 \times N_X \times N_Y \times N_Z \times N_B$ operations, which can be decreased to $N^2 \times N_X \times N_Z \times N_B$ using the outlined 2D pressure method (N is the number of atoms; N_X, N_Y and N_Z are the number of grid cells along x, y and z-directions respectively; N_B is the number of discrete points for bond function). While extending the pressure estimation theory to a 2D grid, the spherical volume is changed to a cylindrical volume as shown in Figure 4-1a.

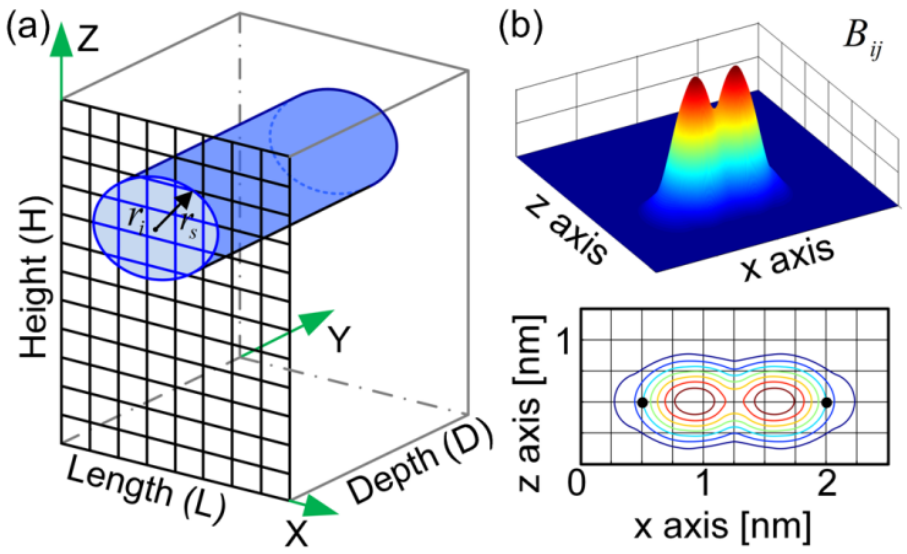

Figure 4-1. Weight and bond function developed for two-dimensional pressure formulation. (a) Cylindrical volume of influence associated with an atom located at r_i, where r_s is the spread radius, L, D, H are length, depth and height respectively. (b) Visualization of bond function for two atoms separated at a distance of 1.5 nm. The gradient image (lower) shows the surface plot of the same.

The derivation of 2D pressure formula is given below.

We start with a general interpolation function w ,

$$w(r) = C_1 w_0(r) \tag{4-2}$$

Where smearing function w_0 is,

$$w_0(r) = \begin{cases} 1 - 3r^2/r_s^2 + 2r^3/r_s^3, \; 0 < r < r_s \\ 0, \; elsewhere \end{cases} \tag{4-3}$$

Distance between atom and grid points is $r = \sqrt{rx^2 + ry^2}$, $rx = x_i - x_p$ and $ry = y_i - y_p$ are the difference between position of i^{th} atom and p^{th} grid point, r_s is the spread radius, R_c is the potential cutoff radius and C_1 is the normalization constant.

The weight function is normalized over the spread radius $\int w(r)\,dr = 1$

Integrating over the cylindrical volume gives,

$\int_0^{r_s} 2\pi r D C_1 \left(1-3r^2/r_s^2+2r^3/r_s^3\right)dr = 1$, where D is the depth of the domain as shown in Figure 4-1a. This will give the value of constant to be $C_1 = 10/3D\pi r_s^2$

Therefore the new weight function becomes

$$w(r) = 10\left[1-3r^2/r_s^2+2r^3/r_s^3\right]/\left(3D\pi r_s^2\right) \tag{4-4}$$

Thus, based on the new weight function, the Bond function (B_{ij}), pressure tensor (P), and density of the system (ρ) are defined as:

$$\mathrm{B_{ij}}\left(\mathrm{r_p}\right) = \int_0^1 \mathrm{w}\left(\lambda \mathrm{r_{ij}} + \mathrm{r_i} - \mathrm{r_p}\right)\mathrm{d}\lambda \tag{4-5}$$

$$\mathrm{P}\left(\mathrm{r_p}\right) = \sum_{\mathrm{i=1}}^{\mathrm{N}} \mathrm{m_i v_i} \otimes \mathrm{v_i w}\left(\mathrm{r_i} - \mathrm{r_p}\right) + \sum_{\mathrm{i=1}}^{\mathrm{N-1}} \sum_{\mathrm{j=i+1}}^{\mathrm{N}} \mathrm{r_{ij}} \otimes \mathrm{F_{ij} B_{ij}}\left(\mathrm{r_p}\right) \tag{4-6}$$

$$\rho\left(\mathrm{r_p}\right) = \sum_{\mathrm{i=1}}^{\mathrm{N}} \mathrm{m_i w}\left(\mathrm{r_i} - \mathrm{r_p}\right) \tag{4-7}$$

where, r_i is the position of i^{th} atom, r_p is the position vector of p^{th} grid point, F_{ij} is the force between two atoms, $r = r_i - r_p$, m_i is the mass of i^{th} atom, v is the velocity and $r_{ij} = r_i - r_j$. Figure 4-1b shows the variation of bond function for a pair of atoms kept at 1.5 nm apart. The isometric view shows the variation of magnitude of bond function for a spread radius of 0.5 nm.

For completeness, we have also derived the 1D variation of pressure and density which is suitable for 1D inhomogeneous systems like pressure in thin films, lipid bilayers etc. For this case a rectangular prism is considered with width of spread radius on either side of the particle location.

Integrating over the rectangular prism gives, $2\int_0^{r_s} LDC_2\left(1-3r^2/r_s^2+2r^3/r_s^3\right)dr = 1$,

where L is the length and D is the depth of the domain as shown in Figure 4-1a, where $r = \left| z_i - z_p \right|$ This will give the value of constant to be $C_2 = 1/LDr_s$

Therefore the new weight function becomes $w(r) = \left[1 - 3r^2 / r_s^2 + 2r^3 / r_s^3 \right] / \left(LDr_s \right)$

Researchers who want to use a different weight function, have to reformulate the normalization constants. Table 4-1 shows such formulated 3D and 2D forms for some selected functions. For grid dependent and finite support weight functions like B-splines, a rectangular prism volume should be used instead of cylindrical volume.

Table 4-1 Weight functions for 3D and 2D systems

Function Type	3D Version	2D Version
Quadratic	$w(r)=\frac{15\left(1-r^2/r_s^2\right)}{8\pi r_s^3}$	$w(r)=\frac{2\left(1-r^2/r_s^2\right)}{D\pi r_s^2}$
Exponential	$w(r)=\frac{2.267116}{r_s^3}\exp\left(\frac{r_s^2}{r^2-r_s^2}\right)$	$w(r)=\frac{2.143567}{Dr_s^2}\exp\left(\frac{r_s^2}{r^2-r_s^2}\right)$
Cosine	$w(x,y,z)=\frac{1}{8r_s^3}\left(1+cos\left(\frac{\pi x}{r_s}\right)\right)..$ $\left(1+cos\left(\frac{\pi y}{r_s}\right)\right)\left(1+cos\left(\frac{\pi z}{r_s}\right)\right)$	$w(x,y,z)=\frac{1}{4Dr_s^2}\left(1+cos\left(\frac{\pi x}{r_s}\right)\right)..$ $\left(1+cos\left(\frac{\pi z}{r_s}\right)\right)$

4.3 Computational Cost Estimation

The computational cost associated with traditional convolutions are shown in the Figure 4-2 for 3D and 2D cases. Consider N atoms in a 3D periodic box interacting with each other. The pressure estimation requires the force between the atoms to be calculated. This is $O\left(N^2\right)$ operations. This can be brought down to $O\left(N^{3/2}\right)$ by modified force summation equation. However for this work, we will consider it as $O\left(N^2\right)$ operations.

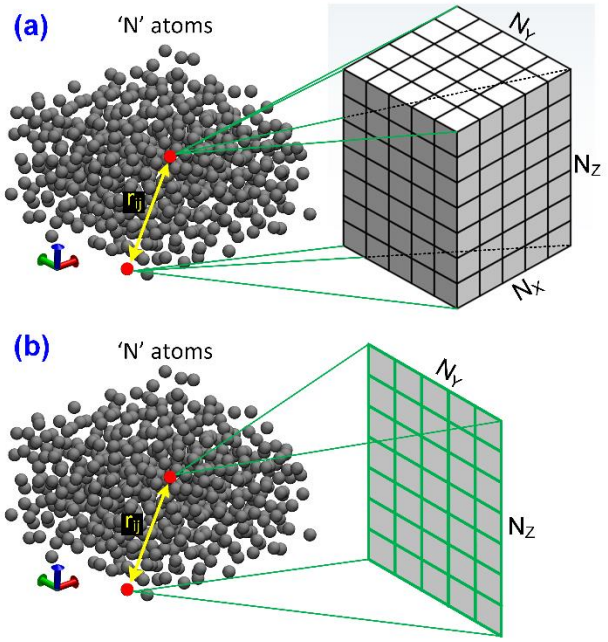

Figure 4-2. Graphical representation of 3D and 2D convolution. (a) N number of atoms interacting with each other and convoluting with 3D grid. (b) The convolution of N atoms with a 2D grids

The local pressure estimation in a grid involves convolution of the kinetic and virial contribution with a weight function. This weight function can be delta or any arbitrary function. A smooth function is generally preferred to avoid large ensemble averaging as with delta function. The equation of local pressure estimation is shown in equation 4-8. The first component is the kinetic component and the second one is the virial pressure.

$$\mathrm{P}\left(\mathrm{r_p}\right)=\sum_{\mathrm{i=1}}^{\mathrm{N}}\mathrm{m_i v_i}\otimes\mathrm{v_i w}\left(\mathrm{r_i}-\mathrm{r_p}\right)+\sum_{\mathrm{i=1}}^{\mathrm{N-1}}\sum_{\mathrm{j=i+1}}^{\mathrm{N}}\mathrm{r_{ij}}\otimes\mathrm{F_{ij}B_{ij}}\left(\mathrm{r_p}\right) \tag{4-8}$$

The kinetic component has to loop over all particles and then also loop over the 3D or 2D grid. For brevity we will explain only 3D case algorithms here. This involves $N\times N_X\times N_Y\times N_Z$ operations. The algorithm is shown below. The virial component has to be embedded inside the force calculation module. The distance between every interacting particles r_{ij} is estimated by

looping through all of them, following which the estimated force has to be convoluted with the bond function. This involves $N^2 \times N_X \times N_Y \times N_Z \times N_B$ operations, where, N_B is the number of discretization points for bond function estimation. The algorithm is given below. Similarly for a 2D case the computational cost will be $N \times N_Y \times N_Z$ and $N^2 \times N_Y \times N_Z \times N_B$ for kinetic and virial components respectively.

```
Algorithm for Kinetic component estimation -- After velocity module
For i = 1 to N
      KE = m(i)*v(i)*v(i)
      r(i) = (x(i),y(i),z(i))
      For k1 = 1 to Nx
            For k2 = 1 to Ny
                  For k3 = 1 to Nz
                        r(p) = (k1*dx,k2*dy,k3*dz)
                        W(r(p),r(i))= r(i)-r(p)
                        KE_PRESS = KE*W(r(p),r(i))
                  End
            End
      End
End
```

```
Algorithm for Virial component estimation -- along with force module
For i = 1 to N
   r(i) = (x(i),y(i),z(i))
      For j = 1 to N
            r(j) = (x(j),y(j),z(j))
            If i <> j
               rij = r(i) - r(j)
            find force(i,j)
            For k1 = 1 to Nx
            For k2 = 1 to Ny
            For k3 = 1 to Nz
                  r(p) = (k1*dx,k2*dy,k3*dz)
                     For k = 1 to NB
                        Bond = Function(r(p),rij,k)
                        VIR_PRESS = rij * force(i,j) * Bond
                     End
                End
          End
   End
End
      End
End
```

4.3.1 Cost of 2D Pressure estimation from 3D from traditional method

In this section, we discuss the existing traditional method for calculating the 2D pressure. First the 3D pressure in the system is estimated as explained in the previous section of this chapter. As we have shown in the previous section, this is computationally expensive. This 3D pressure data is then averaged into a 2D grid by navigating through all grid points and summing along the appropriate direction. This is done as in equation 4-9, graphically shown in Figure 4-3 and requires additional N_X summations and then averaging on every $N_Y \times N_Z$ grid points.

$$P_{2d}(i,j) = \sum_{k}^{Nz} P_{3d}(i,j,k) / N_Z \tag{4-9}$$

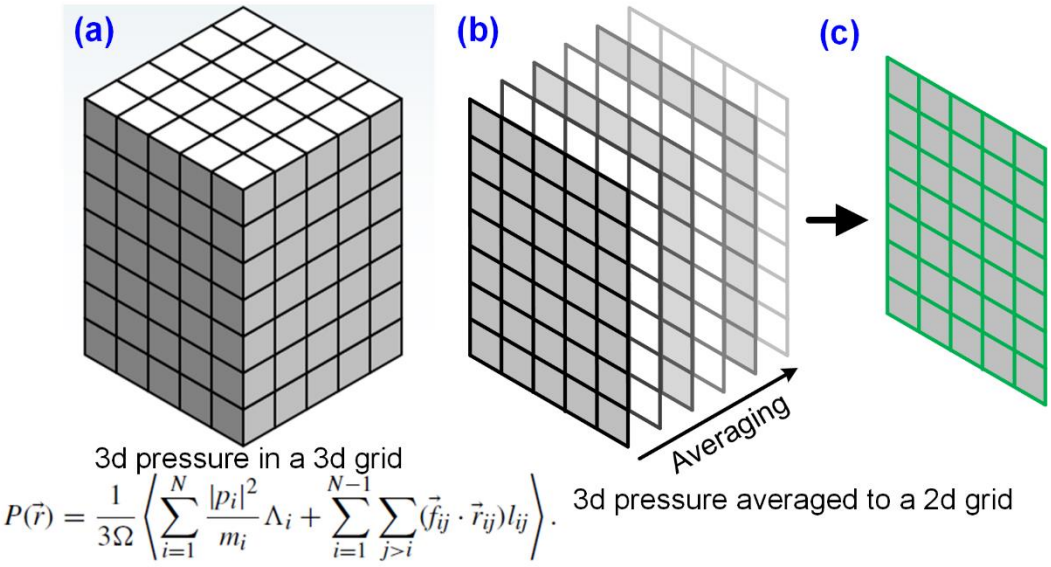

Figure 4-3. Schematic of the 2D averaging of properties from a 3D grid data. (a) Pressure, temperature or density estimated for three dimensions and stored in a 3D grid. (b) Averaging the properties in slices of 2D planes along a particular direction to obtain 2D properties. (c) 2D averaged properties in a 2D grid.

4.3.2 Computational Cost of Direct estimation of 2D pressure

In this method which is developed in our work, we can estimate the pressure on a 2D grid directly from the virial. This method works with a computational cost of $N^2 \times N_Y \times N_Z \times N_B$. We have shown in the derivation section that the volume effect of the 3rd dimension (along X) is taken into account by modifying the weight function appropriately. This method doesn't require an initial 3D estimation ($N^2 \times N_X \times N_Y \times N_Z \times N_B$) and followed by averaging ($N_X \times N_Y \times N_Z$). Thus computationally, the new method will be much faster than the conventional method.

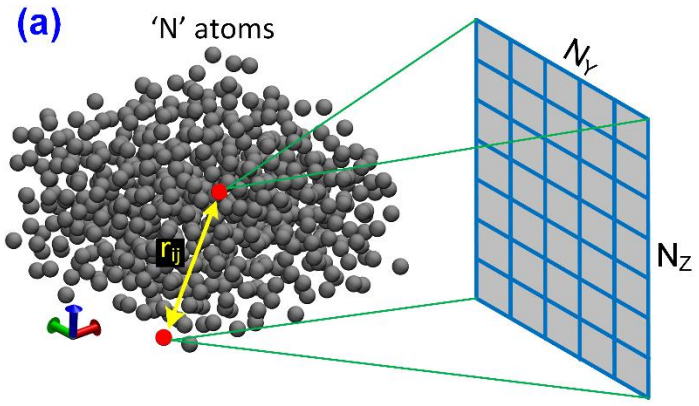

Figure 4-4. Direct estimation of pressure in a 2D grid. (a) The interaction between N atoms are smeared (using 2D convolution) to a 2D grid directly.

Next, we discuss a sample case study to show how costly it is to do a 3D pressure compared to 2D. Consider a system of N atoms in a rectangular prism of sides L, B, H. Assume the grid size to be 0.1 nm for arbitrary calculations. Therefore, $N_X = \frac{L}{0.1}, N_Y = \frac{B}{0.1}, N_Z = \frac{H}{0.1}$ respectively. Also let's assume $N_B = 100$ for convenience.

Table 4-2. Number of operations for different system parameters

	3D case		2D case		3D to 2D Ratio	
	kinetic	virial	kinetic	virial	kinetic	virial
N=10, L=2, B=2, H=2	8.0E+04	8.0E+07	4.0E+03	4.0E+06	20	20
N=100, L=2.5, B=2, H=2	1.0E+06	1.0E+10	4.0E+04	4.0E+08	25	25
N=500, L=3.25, B=4, H=3	2.0E+07	9.8E+11	6.0E+05	3.0E+10	33	33
N=1000, L=2.5, B=2, H=10	5.0E+07	5.0E+12	2.0E+06	2.0E+11	25	25
N=5000, L=8, B=5, H=5	1.0E+09	5.0E+14	1.3E+07	6.3E+12	80	80
N=10000, L=9, B=10, H=10	9.0E+09	9.0E+15	1.0E+08	1.0E+14	90	90
N=20000, L=7.5, B=8, H=8	9.6E+09	1.9E+16	1.3E+08	2.6E+14	75	75
N=50000, L=10, B=10, H=15	7.5E+10	3.8E+17	7.5E+08	3.8E+15	100	100

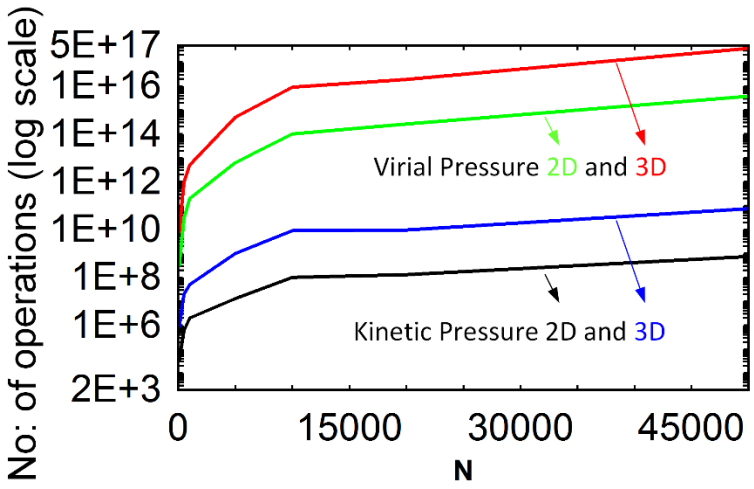

Figure 4-5. Performance comparison chart for 3D and 2D versions of the pressure formulae. The Y-axis represents the number of convolution operations in logarithmic scale and X axis represents the number of atoms. The upper two plots are for virial pressure component and lower two for kinetic pressure. The 2D pressure curve shows the same trend but much faster than the 3D version.

Table 4-2 shows the comparison of number of operations required for various sample 3D and 2D cases for both kinetic and virial components for a single time step. Even for a simple

system the performance of 2D system is 20 times than that of 3D. The speed gain is also dependent on the direction of the averaging performed. For the current cases the 2D estimation is done in YZ plane. Depending on the length along X direction, the performance increase can go beyond 100 times.

4.4 Validation of the Pressure Algorithm

In order to demonstrate and validate the new 2D pressure formulation, we apply it to study the pressure, surface tension, and density variations of argon liquid films suspended in argon vapor using molecular dynamics (MD) simulations.

4.4.1 1D inhomogeneous system pressure validation

In our chosen example (argon liquid film suspended in vapor) and also in the case of lipid bilayers [80], the inhomogeneity is in one dimension (say, Z axis) and there is no density variation along the other dimensions (X and Y axes). The computational domain is shown in Figure 4-6a. Our self-written C++ molecular dynamics code is used for all simulations. The argon liquid film is 10 nm thick with 7.5 nm thick argon vapor on either sides along the z-direction. The X-Y cross section size is 5 nm x 5 nm. Periodic boundary conditions are applied in all directions. The vapor and liquid domains in this molecular system are first equilibrated separately [87] for 1000 ps in order to get a stable suspended film and are then combined together. The simulation is run for another 1000 ps on which statistical production analysis is performed. The modified Stoddard-Ford LJ potential [39] for argon interactions is used with argon – argon LJ parameters as $\sigma_{Ar-Ar} = 0.34$ nm and $\varepsilon_{Ar-Ar} = 1.01$ kJ/mol. The time step of velocity verlet integration was 5 fs and the thermostat was velocity scaling. A number of simulations for different temperatures, spread radius and cutoff radius were performed. Using the developed 2D formulation, the temporally averaged 2D contours of density and pressure at 90 K are estimated and shown in

Figure 4-6b and Figure 4-6c. The density and pressure results are compared with the saturation properties from NIST thermo physical properties database [24] and found to be in very good agreement, which highlights the accuracy of the pressure and density calculation in the new formulation.

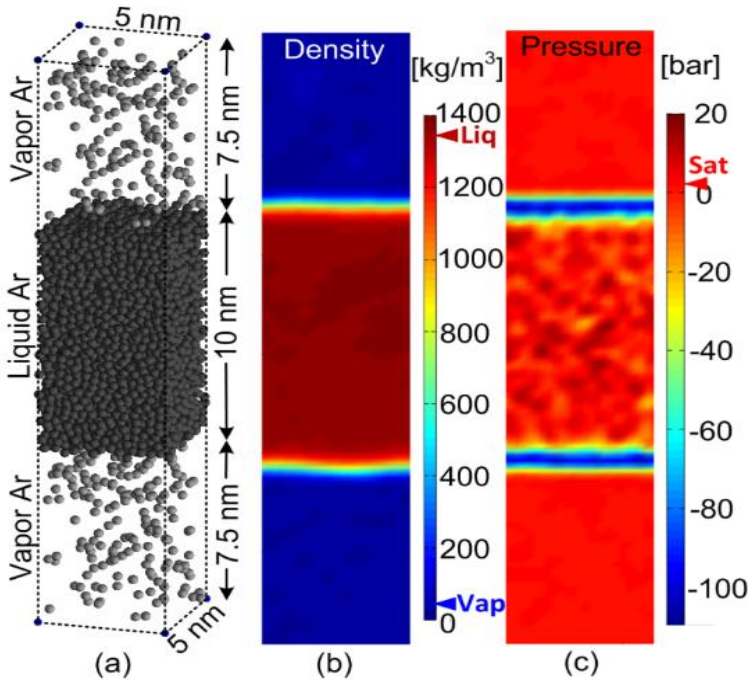

Figure 4-6. Two-dimensional density and pressure profile in argon multiphase system using the new 2D formulation. (a) A 10 nm thick argon film suspended with 7.5 nm thick vapor on both sides along the z-direction. Two-dimensional (b) density and (c) pressure distribution obtained for the system equilibrated at 90K. The saturation density (NIST data) corresponding to liquid (Liq) and vapor (Vap) are marked in the density plot colorbar, while the saturation pressure (Sat) corresponding to the saturated fluid at 90 K (NIST data) is marked in the pressure plot colorbar showing good agreement with the simulation results.

In a series of simulations by varying the cutoff radius from 1 nm to 2 nm, it is found that the thermodynamic properties of argon is best captured by using a cutoff radius of 1.8 nm or larger. However, usage of the cutoff radius as the spread radius (as done in the literature) limits the freedom of simulating an accurate system with finer local details. Thus, in this work, the dependency between the spread radius and cutoff radius has been disconnected which enables us

to retain the accuracy of the simulation without introducing any artifacts by choosing a higher cutoff radius. Nevertheless, the spread radius can be adjusted to capture the localized effects as desired. The formulae that we developed doesn't need spread radius to be same as cutoff radius.

4.4.2 Spread radius sensitivity study

Spread radius is the region of influence of every grid point around it as shown in Figure 4-2. The sensitivity of the spread radius on pressure and density results is studied using the system shown in Figure 4-6a by varying the spread radius to 0.2 nm, 1 nm and 1.8 nm and estimating the 2D properties of pressure and density. The 2D values are then averaged along the X axis to obtain a 1D pressure and 1D density profile varying along the Z axis as shown in Figure 4-7a and Figure 4-7b respectively. Alongside, the pressure and density calculation based on the already-established 1D IK method [87] with a slab thickness of 0.2 nm are also plotted. The results in Figure 4-7a and Figure 4-7b show that density and pressure smoothens and spreads to a larger area as the spread radius is increased. Also, when the spread radius is small and comparable to the slab thickness of IK method, both density and pressure matches very well. As expected, the bulk region (vapor only and liquid only) properties are found to be not sensitive to the spread radius since it primarily captures the local effects. Further, to understand the dependency of the bond function to the spread radius, the bond function for two atoms placed at 1.5 nm apart are plotted with varying spread radius of 1 nm, 0.5 nm, 0.3 nm and 0.1 nm (Figure 4-7c-f). The resulting images show an important result: the spread radius determines the degree of sharpness required to capture the local features as desired. Further, as long as the integral of bond function is unity and conserved, it does not give erroneous values for surface tension, density or pressure. However, care should be taken while selecting the grid cell size for smearing as the results may be less accurate when the spread radius

becomes comparable to grid size (although the resulting artifacts can possibly be alleviated using finite support weight functions like B-Splines).

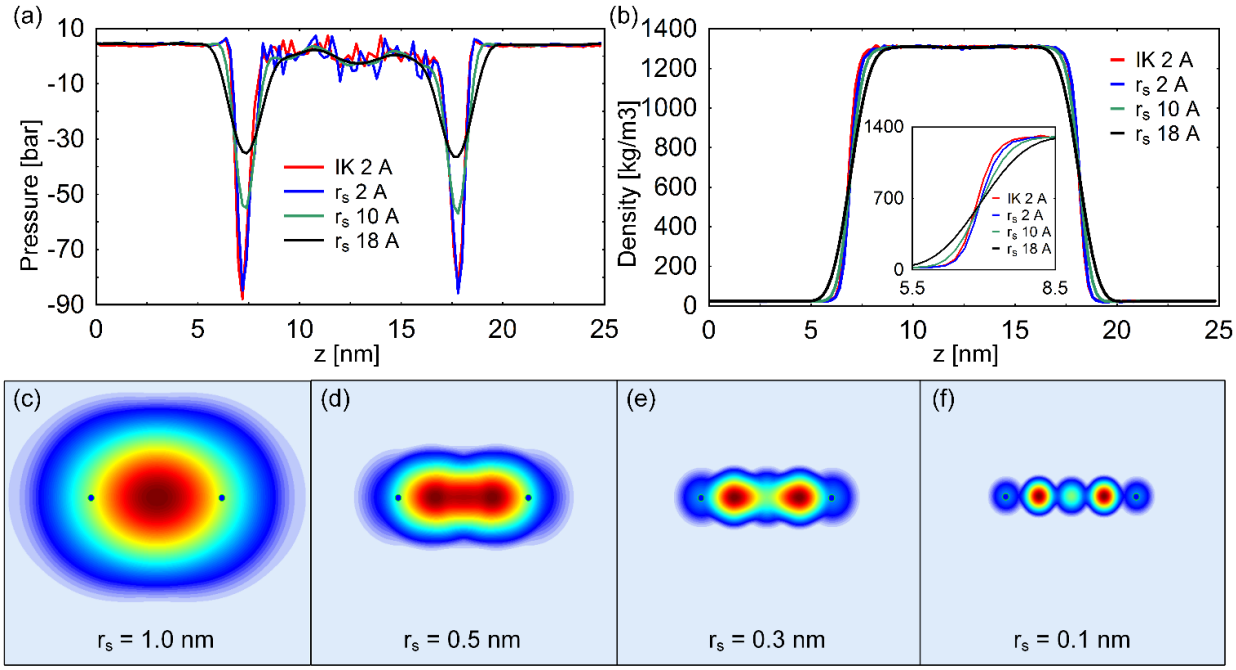

Figure 4-7. Sensitivity study of spread radius r_s on bond function, pressure and density. (a) Pressure variation across the argon film for different values of r_s. IK 2 A is the case study using the established Irving-Kirkwood's modified 1D implementation[87] for comparison. The IK 2 A and the new 2D formation based profiles show good agreement when the volume of smearing became comparable. (b) Density variation across the film for different values of r_s which confirms that the overall system bulk properties is not affected by the spread radius. (c-f) Contour plots of bond function with r_s ranging from 1 nm, 0.5 nm, 0.3 nm and 0.1 nm for two atoms kept 1.2 nm apart in a 3 nm x 3 nm domain. The plots visually show how the bond function controls the spreading of the pressure and density across the grids for different spread radii.

Next, we discuss the validation of the 2D pressure formulation by performing multiple simulations with varying temperature of the argon system (90 K, 100 K, 110 K, 120 K, 130 K, and 140 K) and comparing the simulation results with the experimental thermodynamic properties of argon from NIST database. The spread radius and cutoff radius are chosen as 0.5 nm and 1.8 nm

respectively for these simulations. We would like to re-emphasize the fact that spread radius does not alter any continuum level quantities and the choice of 0.5 nm as the spread radius is merely arbitrary. Thermodynamic quantities like pressure, density and surface tension are estimated using the developed 2D methodology. The 2D results are averaged along the X axis to obtain a 1D pressure and 1D density profile varying along the Z axis.

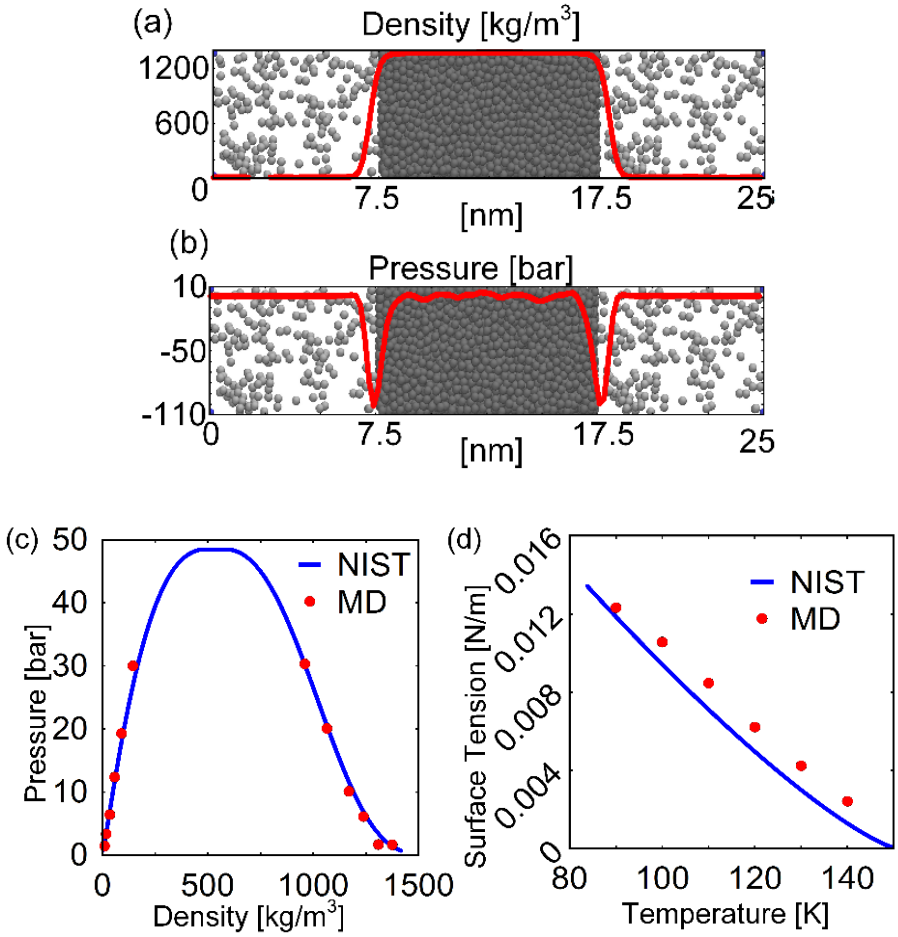

Figure 4-8. Comparison of MD simulation results with the standard thermodynamic physical data from NIST [24]. (a) 1D density profile and (b) 1D pressure profile, deduced from the new 2D formulation method, plotted over the molecular simulation of argon film. The interface locations capture the expected change in pressure and density. Comparison of MD simulation results and thermodynamic data for (c) pressure vs. density, and (d) surface tension vs. temperature showing excellent agreement. Pressure is estimated by temporal and spatial averaging of vapor and liquid regions separately.

A visualization of pressure and density variation along the height of the domain is shown in Figure 4-8a and Figure 4-8b which is consistent with previous argon film studies [86, 87]. The comparison of pressure vs. density and surface tension vs. temperature are plotted in Figure 4-8c and Figure 4-8d, respectively, and show very good agreement with the experimental data [24]. These simulations confirm the validity and accuracy of the new 2D formulation method developed and presented in this work.

4.4.3 2D inhomogeneous system pressure validation

In this sub section, as an additional example we have estimated the pressure difference in a cylindrical droplet as shown in Figure 4-9a. The droplet is symmetric in the plane of the figure with a depth of 3 nm, has periodic boundary conditions all around with sides as 11 nm each, and is a 2D inhomogeneous system. The droplet is equilibrated for 1000 ps and then production runs are done for another 2000 ps. The pressure and density is estimated every 20 steps and averaged. During this course the center of the droplet has moved away from the original location. In order to avoid a skewed averaging, center of mass of every data set is found and readjusted to the center of the domain before averaging. The resulting ensemble averaged density and pressure is shown in Figure 4-9b and Figure 4-9c respectively.

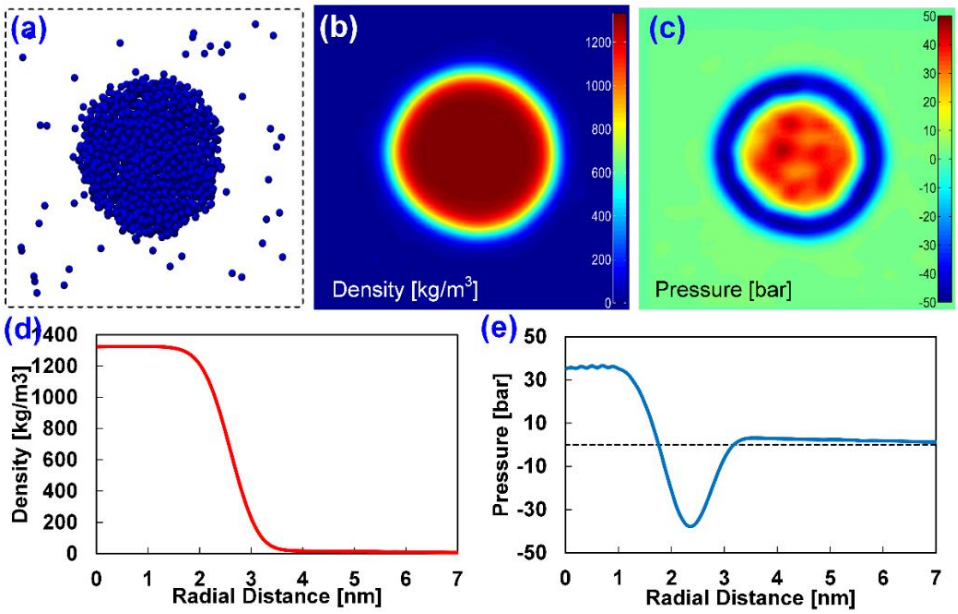

Figure 4-9. Laplace pressure study in a cylindrical liquid argon. (a) Molecular model of cylindrical argon in a 3d periodic box. (b) Density of the system after ensemble averaging using our 2d method. (c) Pressure of the system ensemble averaged using our 2d method. (d, e) Density and pressure variation from the center of the cylindrical argon radially outward.

The variation of the density and pressure from the center of the droplet towards outside is shown in Figure 4-9d and Figure 4-9e. The excess pressure inside the drop is given by the classical Young-Laplace equation:

$$P_{in} - P_{out} = \frac{2\gamma}{R} \tag{4-10}$$

where P_{out} and P_{in} are the outside and inside pressures of the drop, γ is the surface tension, and R is the radius of the drop. All parameters in equation 4-10 are estimated independently from the MD simulations. For the system simulated, we obtain $R \sim 2.5nm$ from the density profile, and the surface tension is estimated as $\gamma = 0.00316N/m$. In order to estimate the radial variation of the properties like normal pressure, density, tangential pressure and surface tension, we used the 2D rotation matrix in combination with B-spline interpolation polynomials. The left hand side of equation 4-10 results in a value of ~3.4 MPa, while the right hand side results in ~2.5 MPa. The

difference between them are expected to minimize upon selection of a bigger cylindrical droplets. These simulations confirm the validity and accuracy of the new 2D formulation method developed and presented in this chapter.

5 Passive Flow and Heat Flux Estimation

5.1 Introduction

The transport of liquid is an important phenomenon occurring in many natural and man-made systems. Nature utilizes the passive flow of liquid towards this purpose, 1e.g., water flows up a height of over 100 m in redwood trees [88] which requires a pressure difference of ten atmospheres. Macro-scale man-made systems typically use externally driven mechanisms, such as pumps, to drive the liquid. However, with the advent of nanotechnology, liquid transport in small scale systems is not trivial due to the large pressure drops occurring at such length scales, thus making externally driven flows impractical. An important application is the thermal management of electronics and energy conversion devices (e.g. concentrated photovoltaics), where high-flux cooling is desired by a continuous supply of liquid to the hot surface followed by its evaporation. Inspired from nature, passive liquid flow is the only possible practical solution, albeit at higher and well-controlled flow rates to avoid system failure. Passive liquid flows, driven by liquid-vapor surface tension forces, have been extensively studied. Primary examples include Marangoni flows [89-92] and capillary flows [93-96]. A handful of experimental designs for heat flux removal have been tested based on passive flow generated due to capillary pressure [7, 13]. A maximum heat flux of 96 W/cm^2 [13] was achieved; however, the maximum theoretical limit of heat flux is ~20,000 W/cm^2 from the kinetic theory of evaporation [2], hence moving towards a larger fraction of this goal would require stronger passive flows.

5.2 Computational Studies of Passive Flow

Surface tension driven passive liquid flow occurs in all phase change phenomena at the microlayer (Figure 5-1), however this has not yet been investigated in literature. The phenomenon occurs at the nanoscale, and when coupled with its fluidic and dynamic nature, makes it nearly

impossible to study with current non-intrusive experimental techniques. Hence, under such a scenario, molecular dynamics (MD) simulations are the ideal method to investigate this phenomenon. However, surface-driven flows require the modeling of the temperature gradient on the same surface, which was lacking in MD. The authors developed and validated [97, 98] such a surface-heating algorithm, thus making this fundamental study possible.

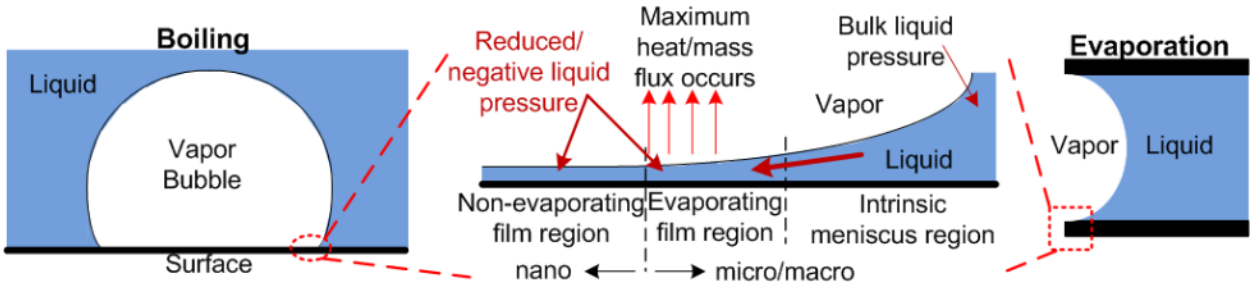

Figure 5-1 A microlayer occurs in all phase-change processes and consists of three multi-scale regions. Passive flow occurs due to the pressure difference generated between the nano non-evaporating film region and the macro bulk meniscus region.

We first characterize the solid-liquid interface at different equilibrium temperatures, followed by differential heating of a liquid film to create a meniscus and attain passive surface-driven flow due to solid-liquid surface tension gradient.

5.2.1 Solid-liquid surface tension estimation

Very little data exists for solid-liquid surface tension, which is the driving force of surface-driven passive flows. Thus, as the first step, equilibrium MD simulations were performed to determine the solid-liquid surface tension at the argon-platinum interface. A thin 6 nm argon film was placed on a 4 x 4 nm platinum surface at seven different cases with surface temperatures varying from 90 K to 150 K in steps of 10 K (Figure 5-2a). The well-established Lennard-Jones interaction parameters for argon-argon and argon platinum were taken from the literature [97]. A surface heating algorithm [97] is used to simulate the heat transfer between platinum and argon.

Simulations were performed for 1000 ps using our in-house molecular dynamics (MD) code written in C++, in which the last 500 ps were used for data sampling and ensemble averaging of various quantities like pressure tensor components, temperature, and density. We used our recently developed 2D pressure calculation algorithm [99] (which is also explained in Chapter 4) to estimate these quantities. For all of the cases and results in this work, we used a spread radius of 0.2 nm with a bin size of 0.1 nm. Surface tension is calculated from the 2D grid values of pressure tensor components and averaged over time. The density of argon is averaged along lateral (X axis) direction and its variation along vertical direction (Z axis) is shown in Figure 5-2b. Inset of Figure 5-2b shows the near-surface density fluctuations. Similarly, the ensemble averaged local surface tension is also calculated along vertical direction and shown in Figure 5-2c for different surface temperatures.

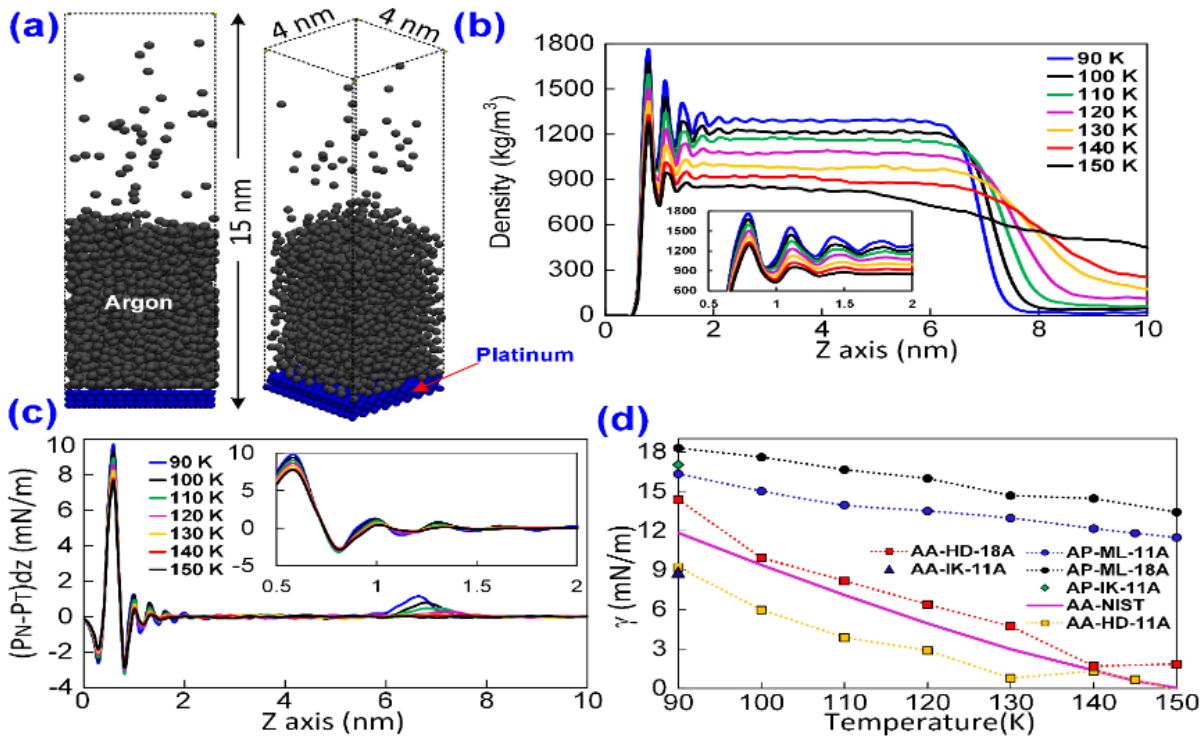

Figure 5-2: Molecular simulation of liquid argon film heated at different surface temperatures. (a) Equilibrated simulation domain of liquid film of 4×4×6 nm on platinum plate at 90 K. (b) Density of the fluid domain along vertical (Z) axis for different surface temperatures. The inset shows the zoomed view

of density fluctuations near the surface. (c) Difference of normal and tangential pressure multiplied by bin size at different surface temperatures along the Z axis. The inset shows the zoomed view near surface. The integral of these curves results in the surface tension. (d) Surface tension of argon-argon (AA) and argon-platinum (AP) using Hardy (HD) [99] and Irving-Kirkwood (IK) methods [100] for the equilibrated cases. The surface tension of argon-platinum for the monolayer (ML) next to the surface is shown for different cutoff radii.

These plots show that the high density regions near the surface occur due to the attractive force of the dense atoms of the surface, and dictate the surface tension. Thus, the solid-liquid surface tension manifests itself in a system based on the strength of the solid-liquid molecular attractions. We estimated the solid-liquid surface tension by integrating the quantity shown in Figure 5-2c from 0.5 nm to 1.5 nm and from 4 nm to 10 nm to obtain the solid-liquid and liquid-vapor surface tension, respectively. The estimated surface tension values and their variation with temperature are shown in Figure 5-2d for Argon-Argon (AA) and Argon-Platinum (AP) for different estimation schemes used: 2D Hardy's method [99] (HD) and Irving Kirkwood's 1D (IK) method [100], and for different cutoff radii: 1.1 nm and 1.8 nm. The results of AA surface tension is compared with experimental NIST data (AA-NIST) [24], and shows good agreement. Results from the well-established IK based analysis is also calculated for comparison with our 2D Hardy method, and shows no variation if we chose appropriate parameters. These results for AA liquid-vapor surface tension validate our in-house code and our 2D pressure estimation method. Further, to the best of our knowledge, this is the first time in the literature that a solid-liquid surface tension is estimated directly from MD simulations.

5.2.2 Passive flow simulations

Next, we performed non-equilibrium MD simulation to attain surface-drive passive flows. Differential surface heating is required in this case; moreover, the 2D pressure algorithm (validated in Figure 5-2d) is essential for estimating the lateral solid-liquid surface tension and relating it to the strength of the passive flow. The simulation domain consists of a 1.5 nm thin argon film on top of a 10 x 4 nm platinum surface (Figure 5-3a-b). A 4 nm region at the center of the platinum surface is heated at different temperatures (red color) while the remaining surface is always kept at 90 K (blue color) in all simulations. Seven simulation cases are run for different temperatures of the heated region: 100 K to 150 K in steps of 10 K, and 145 K. In the last 500 ps of these simulations, the thermodynamic quantities are averaged and estimated. A snapshot of the MD domain is shown in Figure 5-3c for the heated region temperature of 145 K. As the heated region partially evaporates the liquid at the center, a meniscus forms similar to the microlayer (Figure 5-1). Time averaged 2D density, absolute pressure and temperature of the system is shown in Figure 5-3d-f respectively. A crystalline-like dense layering of argon liquid can be seen next to the surface in the cooler region (Figure 5-3d) due to the attractive force of surface atoms. The thin monolayer of argon in the central heated region is also seen in Figure 5-3d but with a lower density compared to the cooler region. This difference in density affects the pressure contours (Figure 5-3e) where liquid pressure is lower in the monolayer in the heated region compared to the cooler region, and becomes the fundamental driving force for passive liquid flow towards the heated region. Figure 5-3f shows the temperature distribution in the heated and cooler liquid regions, as well as the overall domain.

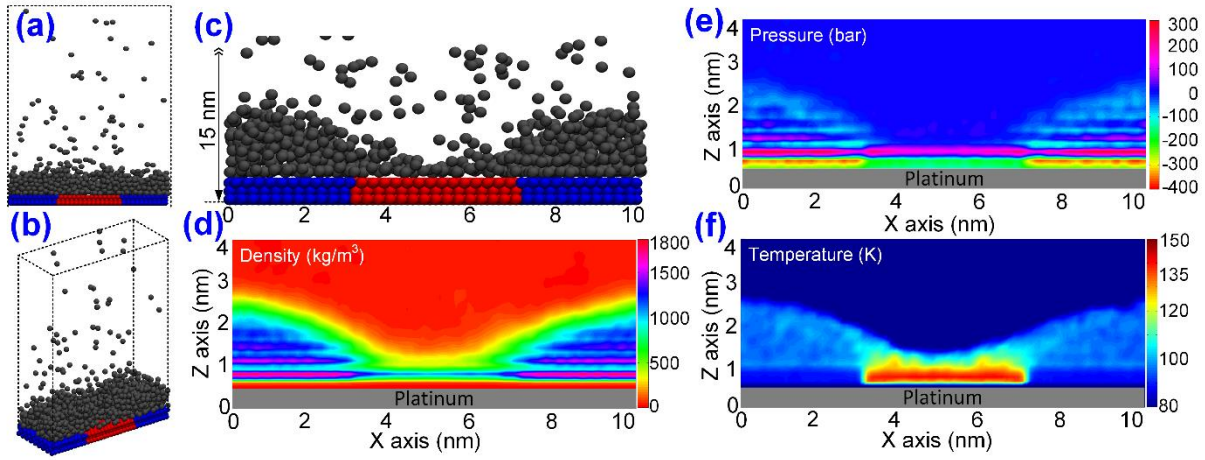

Figure 5-3: Differential heating of argon film on platinum surface. (a, b) Simulation domain with thin (1.5 nm) argon film initially at 90 K on a 10 × 4 nm platinum surface. The red region is heated, while the blue region is kept at 90 K. (c) Equilibrated liquid film when the heated region is at 145 K; the film does not completely evaporate. (d-f) Two-dimensional density, pressure and temperature contours averaged over 500 ps of simulation.

In order to assess the existence of passive liquid flow, the velocity of the fluid from the MD simulation is mapped into an Eulerian field using 2D interpolation [99]. The simulation domain is divided into three imaginary zones A, B and C as shown in Figure 5-4a. The size of the arrows represents the magnitude of the velocity, and the velocities in Zone B are scaled by 3 times to enhance the visibility of the flow field. We observe the formation of a strong passive flow from the cold regions to the heated region in the monolayer next to the surface (Figure 5-4a-c). The heated surface causes evaporation of argon and creates a surface tension variation on the surface. This surface tension gradient force drives and dictates the magnitude of the passive flow (further analyzed later in this chapter).

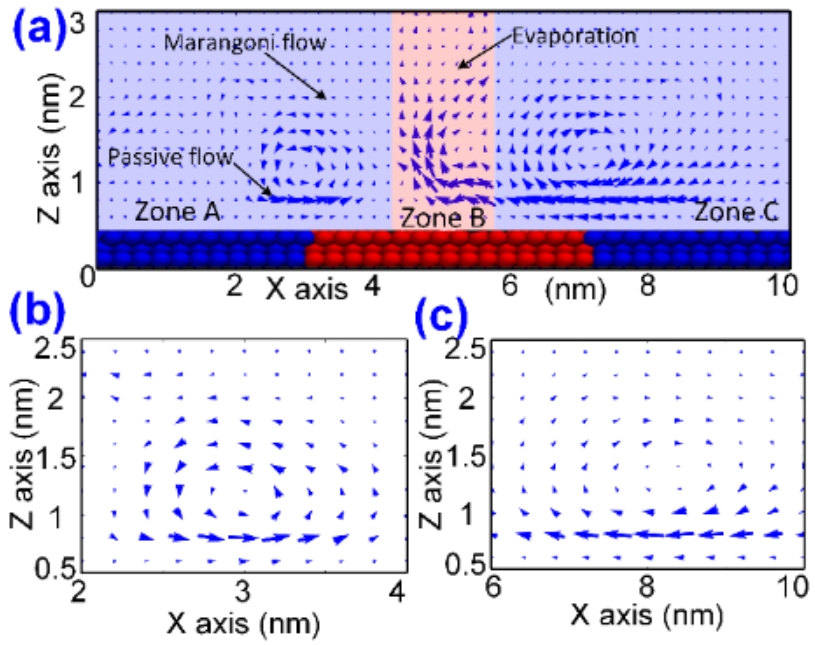

Figure 5-4. (a) Two-dimensional averaged velocity mapping in the domain showing passive liquid flow driven by the solid-liquid surface tension gradient. Size of the arrows indicates the velocity magnitude. Velocities of Zone B are 3× scaled to that of Zones A and C for better clarity. (b, c) Close-up view of the circulation and passive flow regions at either ends.

We also see the Marangoni flow along the liquid-vapor interface causing liquid to flow from the heated to cooler regions. However, as seen in Figure 5-4b-c, the liquid-solid surface-tension driven passive flow is much stronger than the liquid-vapor surface-tension driven Marangoni flow. The velocities of the atoms are smeared into an Eulerian 2D grid and temporal averaging is performed. This process is done for all the cases where the heating temperature is varied from 100 K to 150 K, while keeping the end temperatures as 90 K. The 2D velocity plots are shown in the Figure 5-5.

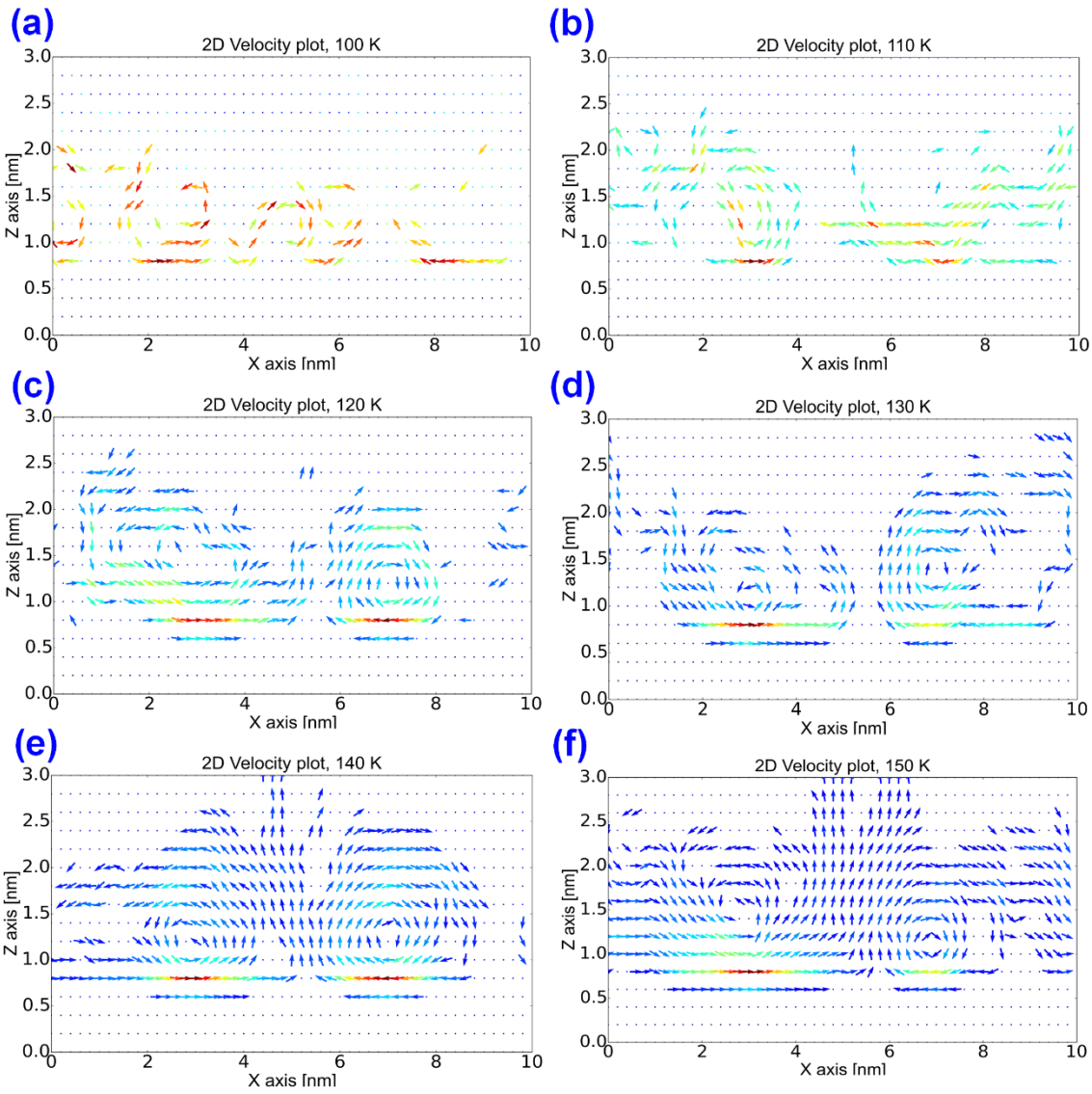

Figure 5-5: (a-f) Velocity plots at varying heated region temperature from 100 K to 150 K. The arrows indicate the direction of flow and color indicates the strength of the flow (red means strong and blue means weak)

As the liquid-solid surface-tension gradient is the main driving force for the surface-driven passive flow, we directly estimate this gradient along the surface. The surface tension gradient is determined by taking the difference of surface tension between the heated and cold regions. The surface tension in monolayer along X axis is obtained by summing $\left(P_N - P_T\right)dz$ from 0.5 nm to 1.5 nm along Z axis and shown in Figure 5-6a for 145 K mid temperature case. The Figure 5-6a

also shows the monolayer average pressure variation along the X axis. This is then averaged for a 2 nm span in heated region and a 4 nm span in cold regions to get the average surface tension gradient. Figure 5-6b shows the comparison of the argon-platinum surface tension estimated from these non-equilibrium simulations of film evaporation with those obtained from the equilibrium simulations of Figure 5-2. The difference between these surface-tension values increases with surface temperature as evaporation from the monolayer decreases its density, and hence its surface-tension, leading to passive liquid flows.

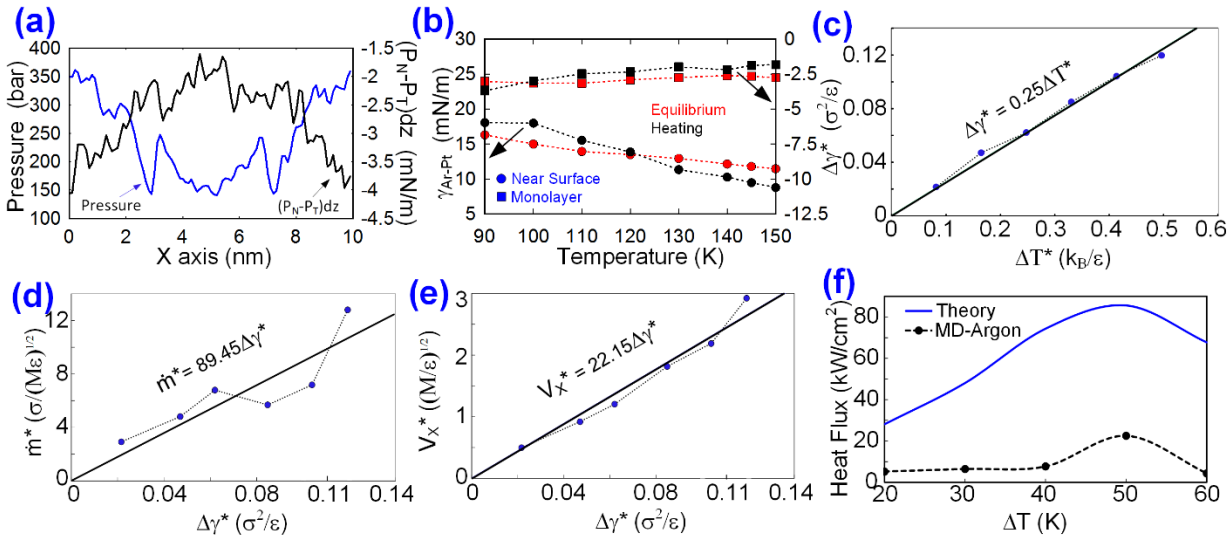

Figure 5-6. Analysis of solid-liquid surface tension driven passive liquid flows. (a) Surface tension of argon-platinum along X axis for monolayer region at different temperatures; this gradient between the regions causes passive liquid flow. (b) Comparison of monolayer surface tension estimated from both equilibrium and differential-heating cases. (c) Non-dimensional surface tension gradient versus surface temperature gradient. (d) Non-dimensional passive flow average velocity along X axis and its dependency on surface tension gradient. (e) Non-dimensional mass flow rate of passive flow with surface tension gradient. (f) Continuous steady state heat flux removed from the surface due to liquid evaporation. The plot shows the comparison between maximum possible heat flux from kinetic theory[2] to that estimated from the simulations.

5.3 Flow Rate and Heat Flux Estimation

From the simulation results, we relate the surface tension gradient with temperature gradient (Figure 5-6c), and found the relation to be linear with $R^2 = 1$, as expected from continuum equations. We further analyze the steady-state flow velocity, mass evaporation rate, and the heat flux and relate it to the solid-liquid surface-tension gradient and surface temperature difference. Quantities are non-dimensionalized so that the results can be extended for other non-polar solid-liquid combinations. Figure 5-6d shows the average passive liquid flow velocity, determined using the analysis from Figure 5-4, as a function of the surface tension gradient, which shows how very high flow velocities can be achieved. We estimate the average evaporation rate (from Zone B of Figure 5-4) by performing a control volume analysis (please refer to Figure 5-7) and relate it to the surface-tension gradients for different surface temperatures. The control volume is selected based on the judgment about the most probable location of evaporation without immediate condensation of the argon. The mass flow rate is estimated by averaging the net velocity outflow and average density in the top portion of the control volume. This analysis is performed for different heating temperature cases ranging from 100 K to 150 K and shown in the Figure 5-7.

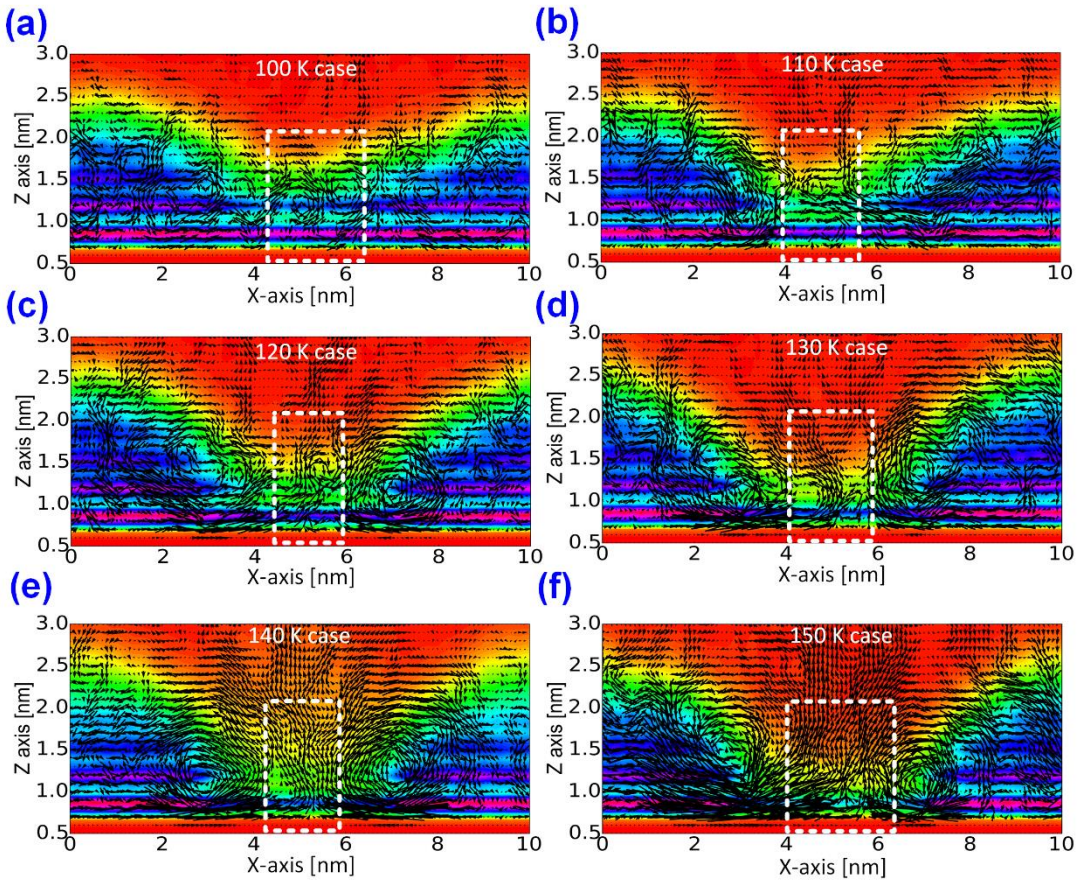

Figure 5-7: Control volume analysis at different heating temperatures. (a-f) Control volume defined based on the judgment of most probable location of evaporation is shown for the various cases.

The evaporation rate is determined based on the density and velocity averaged on the top boundary of control volumes (the control volumes for different heating temperatures are shown in Figure 5-7.). Such empirical relations can be used to design the operating conditions of passive-flow driven thermal management devices as they can help predict the surface tension gradient and mass flow rate generated for a desired surface temperature gradient.

Based on the attained evaporation rate and the heating area, we estimate the stead-state averaged evaporative heat flux obtained in the system. As mentioned earlier, the heated surface area is 4×4 nm where the surface-heating algorithm is applied. The resulting values are compared (Figure 5-6f) against the theoretically possible maximum heat flux [2] values obtained from the

following equation: $q_{max} = \rho_g h_{fg} \sqrt{RT / 2\pi}$ [2].The heat flux, in kW/cm^2, is shown as a function of temperature difference between heated and cold regions in Figure 5-6f. The simulation results follow the theoretical trend where the heat flux peaks at the temperature difference of 50 K. Beyond that, the temperature of the heated region reaches the critical temperature of argon thus resulting in a decline. The peak heat flux obtained in simulations is 22.5 kW/cm^2 and is orders of magnitude higher than the maximum reported values in experiments. To the best of our knowledge, this is the first study where steady-state, continuous and passive high-heat flux removal close to the theoretical limit is obtained.

6 MD Studies with Water and Platinum

6.1 Introduction

This chapter explain the need for and development of a surface-heating algorithm for water for molecular dynamics simulations. The validated algorithm can simulate the transient behavior of evaporation of water when heated from a surface, which has been lacking in the literature. The algorithm is used to study the evaporation of a water droplet on a platinum surface at different temperatures. The resulting contact angles of droplets are compared to existing theoretical, numerical and experimental studies. Evaporation profile along the droplet's radius and height is deduced along with the temperature gradient within the drop; the evaporation behavior conforms to the Kelvin-Clapeyron theory. The algorithm captures the realistic differential thermal gradient in water heated at the surface and is promising for studying various heating/cooling problems such as thin film evaporation, Leidenfrost effect, etc. The simplicity of the algorithm allows it to be easily extended to other surfaces, and integrated into various molecular simulation software and user codes.

6.2 Zhu Philpott potential

In 1991, Raghavan et al. [101] studied the dynamics and structure of water on top of a platinum FCC 111 wall. They came up with an improved model to predict the behavior of water on top of platinum and also how to take care of the corrugations on the surface. They have matched the density and potential mapping based on Sphor's model [102] with their model and found good agreement. In 1994 Zhu and Philpott [103] studied the structural properties of water near the platinum wall. They reported that the adsorption energies match with quantum mechanical calculations. We have used this potential for water-platinum interaction in this thesis, and will call it as "ZP potential". ZP potential is proven to be accurate in estimating contact angle of water

droplet on platinum surface [104]. It is also worth mentioning that the Sphor potential [102] will perform a similar function but is computationally expensive. Sphor's potential predicts the adsorption of water on top sites of platinum and exhibits a minimum for orientations with the oxygen atom closer to the surface than the hydrogen atoms. It also predicts correct adsorption energies similar to ZP potential.

The ZP potential of water to metal has three components and can be expressed as below.

$$E_{Total} = E_{Conduction} + E_{Isotropic} + E_{Anisotropic} \tag{6-1}$$

where first component is the conduction energy of attraction, second is the isotropic attraction and the last component is the modified LJ potential with anisotropic parameters.

$$E_{Conduction} = \sum \frac{q_{real} q_{image}}{2r} \tag{6-2}$$

Where q_{real} and q_{image} are the partial charges of the atoms in the water molecule and its images across the platinum wall, and r is the distance between them.

$$E_{Isotropic} = -4\varepsilon_{w-Pt} \sum \frac{C_{w-Pt}\sigma_{w-PT}^{10}}{r_{w-PT}^{10}} \tag{6-3}$$

$$E_{Anistropic} = 4\varepsilon_{w-Pt} \sum \left[\left(\frac{\sigma_{w-Pt}^2}{\left(\alpha\rho_w\right)^2 + z_w^2}\right)^6 - \left(\frac{\sigma_{w-Pt}^2}{\left(\rho_w/\alpha\right)^2 + z_w^2}\right)^3 \right] \tag{6-4}$$

where the scaling parameter $\alpha = 0.8$ and values of other parameters are given below.

$$\sigma_{O-Pt} = 0.270\,nm, \varepsilon_{O-Pt} = 6.44\times10^{-21}\,J, C_{O-Pt} = 1.28$$

$$\sigma_{H-Pt} = 0.255\,nm, \varepsilon_{H-Pt} = 3.91\times10^{-21}\,J, C_{H-Pt} = 1.20$$

The subscript w refers to oxygen and hydrogens of the water molecule, C is a constant, ε and σ are the LJ parameters, and z is the distance above the platinum wall.

6.3 Literature Review on Thermal Wall Models for Water

In MD simulations which involve liquids, the canonical ensemble is the most commonly simulated by coupling the liquid to an external thermostat [105, 106]. However, thermostats cannot be used to study non-equilibrium phenomena, and the thermostatting of liquid interacting with frozen solid surfaces may give unrealistic results [27, 28]. In order to perform non-equilibrium MD simulations, a number of studies have been done on the surface evaporation of simple non-polar Lennard Jones fluids [32, 38, 107, 108]. Water, although a more practical fluid of interest, has had only a handful of surface evaporation studies [104, 109, 110] primarily due to the presence of electrostatic forces and its complex nature of interaction. Among them, the phantom wall method [107], which uses Langevin based scaling for phantom layers of platinum, has been widely used to simulate the heat transfer between a surface and water [111].

In 2014, Luca et al. [109] proposed a technique to transfer heat from wall to liquid. They introduced 'virtual particles' as seen in Figure 6-1 which vibrate normal to the wall and transfer kinetic energy to the fluid. This method is computationally expensive by the introduction of virtual particles and its additional interaction with fluid particles. Also the work was demonstrated for a very thin film of 1*nm* water confined between walls which makes it questionable about the applicability for films thicker than 1 nm and for droplets.

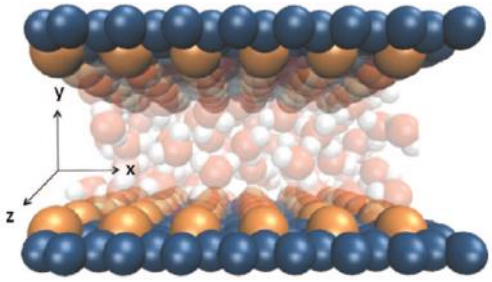

Figure 6-1: Model used by De Luca et al. The wall has additional virtual particles which will move up and down during the simulation and transfer KE to the confined water.

In 2002, Maruyama et al. [112] studied the contact angle of water on top of platinum. Their studies involved the use of Phantom wall method to simulate heat transfer between the wall and liquid water. Following their studies, Bo Shi et al. [104] also performed simulation of water on platinum. The heat transfer between solid and liquid was not modeled explicitly and Berendsen thermostat was used instead. Their works were focused on comparing the contact angles with Young Laplace equation and with experiments.

In 2005, Yang et al. [113] simulated evaporation of thin layer of water kept under vacuum. They used TIP3P water model, and along with classical Schrage model for the interface mass transfer, calculated the evaporation coefficient. They also reported that the interface layer of atoms had lower temperatures than the bulk liquid. In 2011 Yang et al. [114] studied the evaporation of water on top of magnesium surface using MD simulations. Their studies have shown the decrease of water layer thickness with increase in temperature. In 2013 Wang et al. [115] studied the evaporation of water droplets dissolved with salts. SPCE water model was used along with Coulombic and LJ potentials to simulate the system. But none of them have looked into the validation part with respect to water phase equilibrium diagram.

However, these surface heating models of water do not capture the heat transfer characteristics and thermodynamic properties of water evaporation. Moreover these methods which simulate the wall atomic vibrations are: 1) questionable as the integration time steps of both solid and liquid are assumed to be the same even though their atomic vibrational frequencies differ significantly [29, 116] , and 2) computationally very expensive due to the high frequency vibrations. Thus, in order to correctly simulate the transient behavior of water evaporation, a combination of a frozen wall and an appropriate thermal wall algorithm can be applied.

In 2009, Maroo and Chung. [25] formulated a method of heat transfer between solid and fluid by checking force equilibrium between them. This algorithm works by velocity scaling the atoms that meet two main predefined conditions; a distance check above the surface, and force equilibrium check. The method is proven to produce physically realistic results and is working well with argon and platinum. However this algorithm is not sufficient to simulate the heat transfer of water and platinum.

6.4 Development of the Surface Heating Algorithm

The development of a heat transfer model for the ZP potential is not straightforward due to the potential's anisotropic nature. Figure 6-2b shows the ZP potential energy function and its components for a flat water molecule (hydrogens and oxygen of the molecule lying on a plane parallel to platinum surface). The ZP potential influences the structure of water adsorbed on the platinum surface and is of significant importance for developing a surface heating algorithm. Figure 6-2c shows the orientation of the dense single layer of adsorbed water molecules, generally known as a monolayer, with minimum potential contour for a flat water orientation. The structure of the monolayer has a majority of the water molecules in the flat orientation. The monolayer position varies by less than an Angstrom based on the water molecular distribution histograms (Figure 6-2d) for different surface temperatures studied in this work.

The central idea of the new algorithm is shown graphically in Figure 6-2e. A "critical zone" is defined as the region above platinum wall up to a distance of $r_{critical}$. For the water molecules lying in the critical zone, the net force acting on the molecule from the surface is compared with the force acting on it from all other water molecules. If the force due to the surface is larger, the water molecule will be heated (or cooled) to the platinum surface temperature using the velocity

scaling method. Thus, a water molecule is heated (or cooled) by the surface if the following two criteria are met:

$$z_{oxygen} < r_{critical} \tag{6-5}$$

where z_{oxygen} is the location of oxygen atom of water molecule from the platinum surface.

$$\sum_{i=1}^{k} F_{w-Pt}^{i} > \sum_{j=1}^{n} F_{w-w}^{j} \tag{6-6}$$

where k is the number of platinum atoms, n is the number of water molecules, F_{w-Pt} and F_{w-w} represent force interaction between individual molecules for water-platinum and water-water respectively. The basis of this new algorithm is derived from a validated surface heating algorithm created by Maroo and Chung [117], however their algorithm was used for a simpler non-polar LJ argon fluid heat transfer. Unlike argon, a unified critical radius region (minimum potential), $r_{critical}$, is not analytically possible for water-platinum interaction as the ZP potential is anisotropic. Thus, we performed multiple MD simulations to empirically estimate $r_{critical}$ for the surface heating algorithm for water.

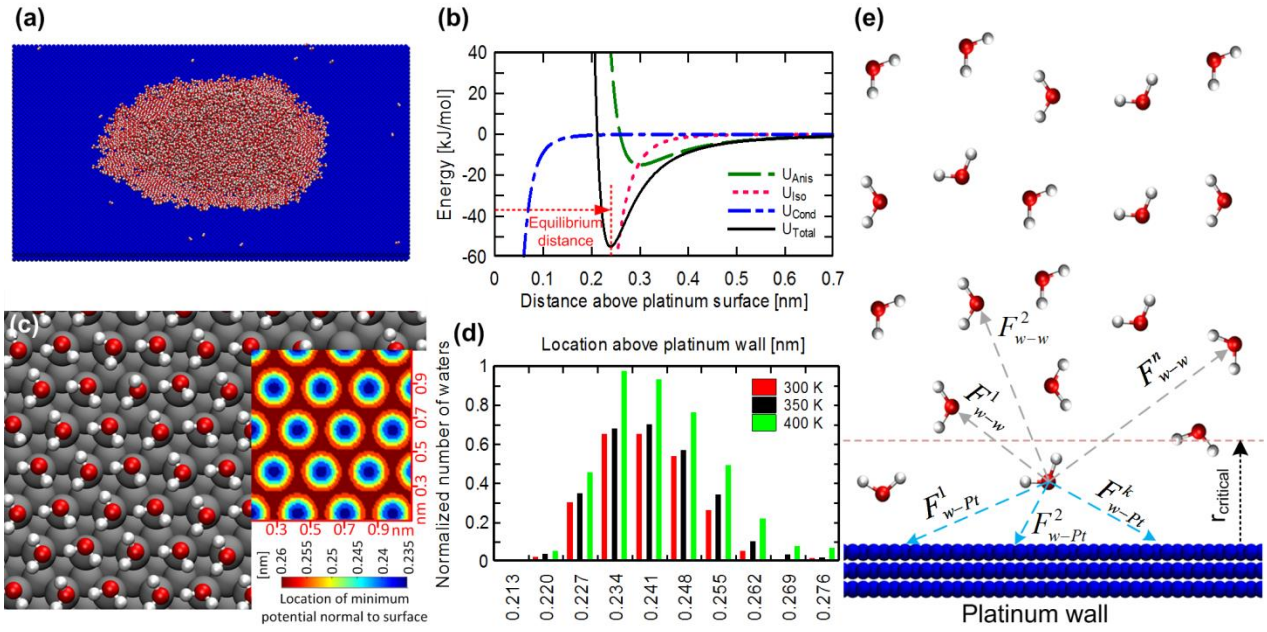

Figure 6-2. Water-surface interaction and the new surface heating algorithm for water. (a) An equilibrated droplet of 7221 water molecules on top of platinum surface (in blue). This droplet was initially a 6 nm side cube and then equilibrated for 1000 ps at surface temperature of 300 K. (b) ZP potential energy and its components based on the interaction of a flat-oriented SPCE [118] water molecule with platinum surface. (c) Orientation of water molecules in the monolayer above the platinum surface showing majority of the water molecules are in flat-orientation along with the minimum potential contours of flat-oriented water molecule. The blue regions in the contour have the strongest attraction and act as the adsorption sites for water to form the monolayer. (d) Frequency distribution of water molecules in monolayer above platinum surface at different surface temperatures; the number density is normalized by a factor of 1000. (e) Graphical representation of surface heating algorithm for water; F^{n}_{w-w} represents the interaction force between a water molecule in the critical radius region and nth water molecule, and F^{k}_{w-Pt} represents the interaction between the same water molecule and kth platinum atom.

In order to estimate the critical radius, a 4 nm cube of water is equilibrated on the platinum surface until it forms a water droplet. The new surface heating algorithm was applied for a surface temperature of 300 K and $r_{critical}$ is varied from 0.248 nm to 0.257 nm. This range of $r_{critical}$ was selected from the positional distribution of water molecules in monolayer (Figure 6-2d) and minimum potential energy location of an individual water molecule. The equilibrated droplet

temperature was measured with varying $r_{critical}$ and the same procedure was repeated for surface temperatures of 350 K and 400 K (Figure 6-3a). Using linear fits, the appropriate $r_{critical}$ was chosen when the surface temperature and droplet temperature match. Thus, a $r_{critical}$ value for each temperature was obtained, from which a correlation was deduced based on a linear fit (Figure 6-3b). Hence, the following correlation can be used to determine $r_{critical}$ for a desired surface heating temperature:

$$r_{critical} = 0.000072 \times T + 0.225133 \tag{6-7}$$

where T is the temperature of the platinum surface $\left(300\,K \le T \le 400\,K\right)$.

6.5 Validation of the Surface Heating Algorithm

6.5.1 Validation using water droplet heating

The next step was to validate and demonstrate that this new algorithm produces physically sound results. Based on the above correlation, additional simulations were performed for surface temperatures of 300 K, 350 K and 400 K with 4 nm and 6 nm cube droplets. The temperature evolution of the water droplets is shown in Figure 6-3c. The equilibrated water drop's mean temperature (Table 6-1) shows the accuracy of the proposed algorithm; the maximum error (deviation of average from the expected surface temperature) is less than 1%. Evaporation of the droplets is observed for surface temperatures of 350 K and 400 K in Figure 6-3d and Figure 6-3e respectively. To the best of our knowledge, there is no prior work reported for the evaporation of water droplets based on surface heating in MD simulations.

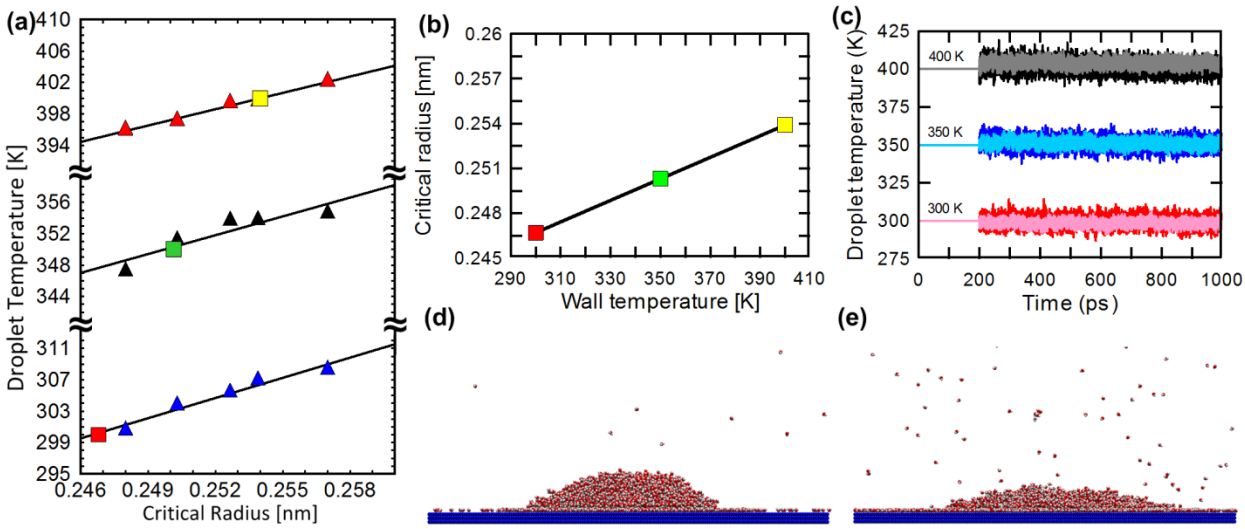

Figure 6-3. Estimation of the critical radius for the surface heating algorithm of water. (a) Droplet temperatures with varying critical radius while maintaining the surface temperature at 300 K (blue triangles), 350 K (black triangles) and 400 K (red triangles). A linear fit for these data is shown as solid lines. Interpolated critical radius values are shown in solid squares when droplet temperature matches the surface temperature. (b) Correlation between critical radius and surface temperature based on data from Figure 6-3a, which be used to determine the required critical radius for a desired surface temperature. (c) The temperature evolution of droplets with velocity scaling for first 200 ps (straight lines) and the surface heating algorithm thereafter. The darker colored lines represent the data for 64 nm^3 volume droplet, and the lighter colored lines for 216 nm^3 droplet at 300 K, 350 K and 400 K surface temperature. Evaporation of 216 nm^3 droplet at (d) 350K and (e) 400K surface temperature (images taken at 1000 ps).

Table 6-1. Water droplet temperature at steady state using the surface heating algorithm for the two MD systems studied (with 64 nm^3 and 216 nm^3 droplet volumes).

Temperature of surface [K]	Droplet Temperature [K]		|Max. error|
	64 nm^3	216 nm^3	
300K	299.4 ± 3.2	298.5±1.8	0.5 %
350K	350.7 ± 3.3	350.9±2.1	0.3 %
400K	400.8 ± 3.5	403.9±2.2	1.0 %

6.5.2 Validation using contact angle studies

In order to further validate the algorithm, we studied the dependency of the contact angle of water droplets at different platinum surface temperatures (300 K, 350 K and 400 K). Contact angle studies are important in understanding the wettability and surface interaction energies. There are many studies on contact angle of water on graphene [119, 120], graphite [121], carbon nanotubes [122, 123], solid surfaces [124, 125], polymer surfaces [126] and platinum [104, 127] using molecular dynamics simulations. However, these studies involve equilibrium MD simulations for contact angle determination, rather than transient surface heating non-equilibrium MD as performed in this work. We developed [128] a fast and accurate algorithm to estimate the contact angle which is applied here. Further, at each time step the droplet is rotated about the axis normal to surface with 1° increments up to 90° and the 2D density based contact angle is estimated. The choice of 1° is arbitrary and can have finer increments. The curvature is fitted assuming a circular shape with a robust geometric fit algorithm [62]. The contact angle values are temporally averaged from 600 ps to 1000 ps at every 1 ps. This procedure provides accurate estimation of contact angle even for small droplet undergoing high fluctuations at the liquid vapor interface. Figure 6-4a shows a screenshot of water droplet on platinum surface, equilibrated at a surface temperature of 300 K, with the bold line representing the circle fit based on the interface identification algorithm. The equilibrated drop contact angles for different surface temperatures are plotted in Figure 6-4b. The contact angles are in good agreement with the theoretical model of Young-Laplace equation [129, 130], prior numerical study [104], and experimental measurement [49].

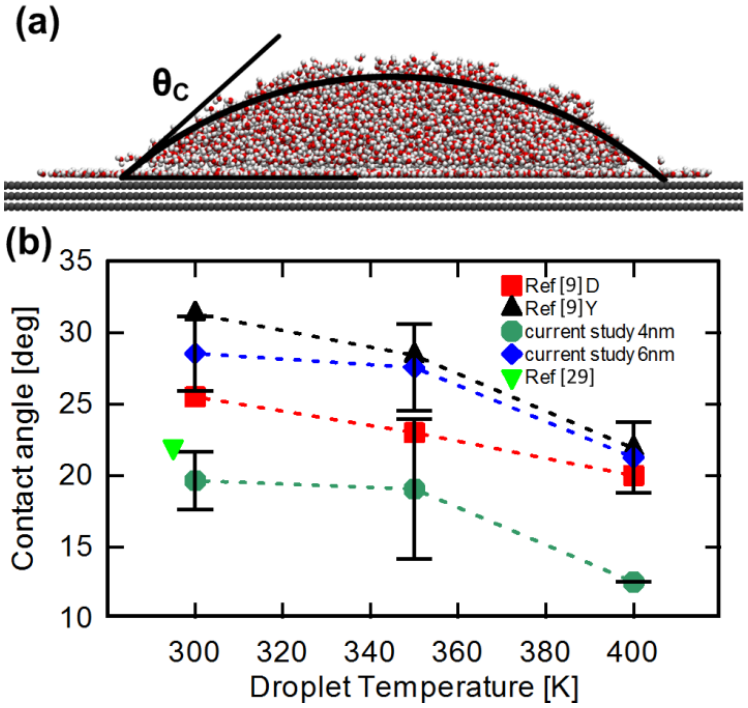

Figure 6-4. Droplet contact angle estimation and comparison. (a) Water droplet equilibrated at 300 K with the solid curved line depicting the liquid-vapor interface. (b) Contact angle of the droplets at different surface temperatures and comparison with literature. The green and blue curves show the data for 64 nm^3 and 216 nm^3 droplets respectively in the present study. The error bars indicate one standard deviation. D and Y in Ref [104] represents data from direct molecular simulation and from Young's equation respectively. Green triangular marker shows the available experimental data [127].

6.5.3 Validation using water droplet evaporation

The algorithm was applied to study the transient behavior of the water droplet evaporation using the 216 nm^3 droplet system. The platinum surface temperature was maintained at 300 K from 0 ps to 200 ps, following which, the surface temperature was changed to 400 K. This resulted in a gradual increase in the temperature of the droplet which initiated evaporation. The transient droplet temperature profile is shown in Figure 6-5a, with the droplet reaching a steady state temperature at ~250 ps. The temperature gradient within the droplet during the transient period of 200-205 ps and 200-235 ps are averaged and plotted in Figure 6-5b. The distribution shows an exponential-like trend with a relation $T = 325.53X^{-0.114}, R^2 = 0.99$ in temperature of droplet in the

initial 5 ps, and a linear change over the larger time period as expected. Temperature contours of the thermal gradient within the droplet are shown in Figure 6-5c at the onset of heating and after the drop reached steady state. As expected at continuum scale, the drop spreads over the surface at the higher temperature and achieves a uniform temperature in steady state.

The evaporation profile of the drop was determined with respect to the distance above platinum (labeled as z-axis) as well as around the centroid of the droplet (labeled as r-axis). An "evaporated" molecule is defined when a molecule suddenly has one or few neighbors within its 0.4 nm radius near the droplet interface, or has less than three neighbors within its 0.4 nm radius away from the droplet. Based on this definition, the evaporation positions of all "evaporated" molecules are identified and quantified in Figure 6-5d. The curve "along z" represents the number of molecules evaporated at positions along the vertical direction, while "along r" curve shows the same data radially outward from the center of the droplet. Both these curves indicate that the base of the droplet has a higher rate of evaporation primarily due to the higher temperature and thinner water film at the base as seen in Figure 6-5c. These results are in agreement with the classical Kelvin-Clapeyron equation [131], where the evaporation rate for a droplet can be approximated as $\dot{m} = a\left(T_{lv} - T_v\right) = a\left(T_s - T_v\right) \Big/ 1 + \frac{a h_m}{k}\delta$, where T_{lv} is the liquid-vapor interface temperature, T_v is the vapor temperature, T_s is the surface temperature, δ is the liquid thickness, k is the thermal conductivity of the liquid, h_m is the latent heat of vaporization, a is a function of temperature, enthalpy of vaporization and pressure of vapor and liquid region [131], and the pressure variation within the liquid region is assumed to be negligible. The equation predicts a higher evaporation rate at regions of higher T_{lv} or smaller thickness δ, similar to that observed from the MD simulations at the base of the bubble.

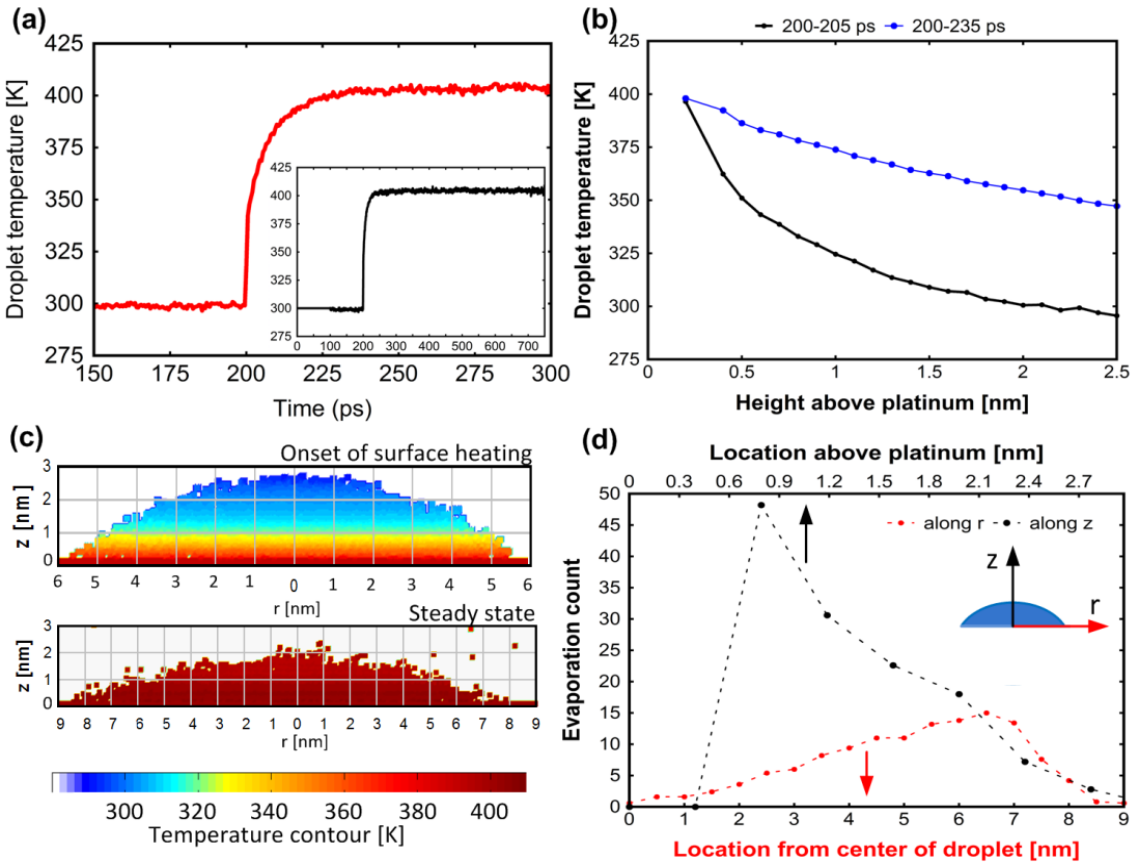

Figure 6-5. Transient behavior of water droplet evaporation using the surface heating algorithm. (a) Average droplet temperature variation with time of a 216 nm^3 droplet when surface is heated from 300 K to 400 K. The inset shows the droplet temperature for the entire time range of simulation. (b) Droplet temperature gradient along the droplet height based on temporal averages from 200-205 ps and 230-235 ps. (c) Thermal gradient contours at the onset of surface temperature increase (upper) and for equilibrated droplet (lower), showing gradual and realistic change in droplet temperature due to the surface heating when compared to heating the entire droplet using a thermostat. (d) The total number of water molecules evaporated between 200 ps to 1000 ps (averaged over 5 different simulation sets) plotted against the location of evaporation, in the vertical direction (along z) and also from the center of the droplet (along r).

6.5.4 Validation using 1D diffusion equation

The surface heating algorithm is applied to a thin water film of 5.5 nm confined between two platinum surfaces as shown in Figure 6-6. There are 735 water molecules subjected to ZP potential interaction with platinum. The system is equilibrated for 500 ps with velocity scaling at 300 K. The surface heating algorithm is applied for the next 500 ps for both wall temperatures of

300 K. At 1000 ps, the left side wall temperature is step changed to 400 K. The space between the platinum walls is partitioned using imaginary slabs of thickness 0.1nm. The temperature of these slabs are estimated and averaged over 1 ps, and shown in Figure 6-7 (a) to (d) at different time intervals. These temperatures are compared against the solution of the classical heat equation (shown in equation 6-5).

$$\frac{1}{\alpha}\frac{\partial T(x,t)}{\partial t} = \frac{\partial T^2(x,t)}{\partial x^2} \tag{6-8}$$

$$T(x,t) = T_{right} + \left(T_{left} - T_{right}\right)\frac{x}{L}$$
$$+\sum_{n=1}^{\infty}\frac{2}{n\pi}\left[\left(T_{left} - T_i\right)(-1)^n - \left(T_{right} - T_i\right)\right]\sin\left(\frac{n\pi x}{L}\right)\exp\left(-\alpha t\left(\frac{n\pi}{L}\right)^2\right) \tag{6-9}$$

Equation 6-5 is the analytical solution of equation 6-4, T_{right} and T_{left} are the right and left wall temperatures respectively, x is the location along x-axis, L is the length along the x-axis and α is the thermal diffusivity of water.

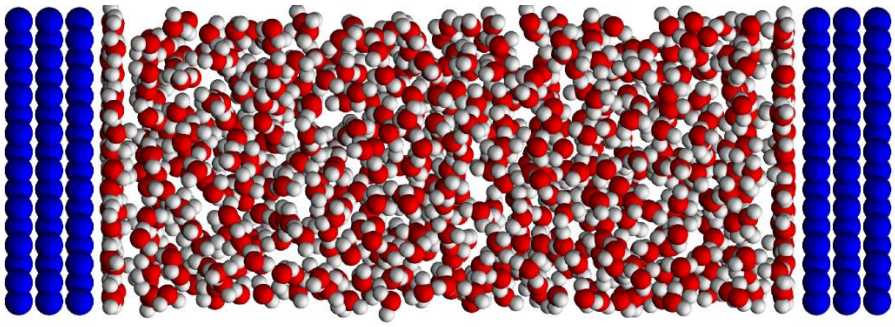

Figure 6-6. Liquid water confined between platinum surfaces

The solution of the heat equation and MD simulation results are compared in Figure 6-7(a-d). The bold line shows the 1D heat equation solution with $n = 25$ terms of equation 6-5 and the markers show the slab averaged temperature from the MD simulation. The averaging is done by considering data up to 1ps forward to the specific time values. For example, the 1000 ps plot shows the data averaged from 1000.1 ps to 1001.1 ps. The transient response comparison plot in Figure

6-7 shows a good agreement and proves the validity of the surface heating algorithm. This study also supports the fact that such thermal gradients occurring in transient simulations can be captured using our new surface heating algorithm.

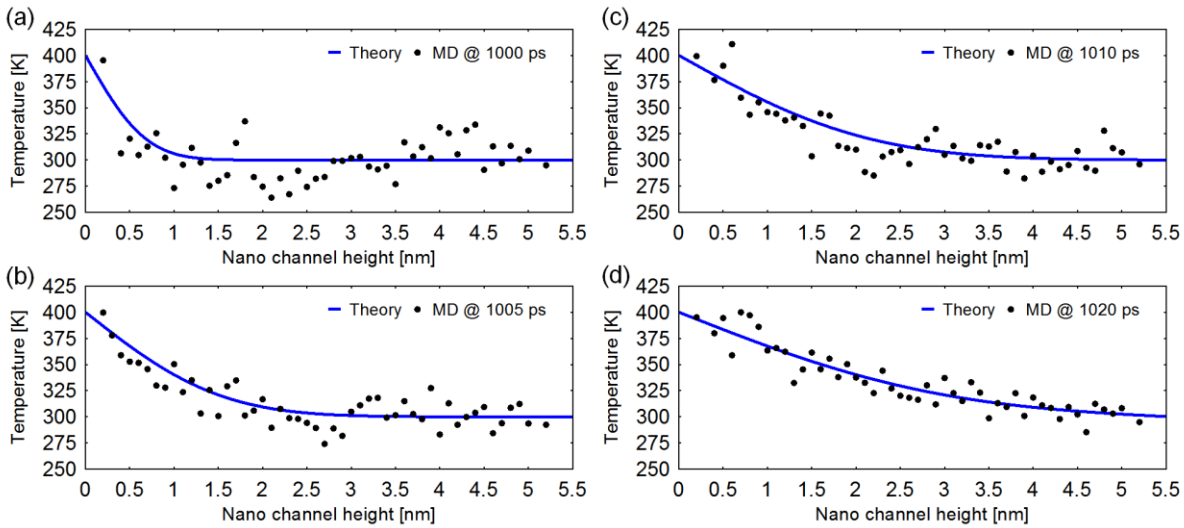

Figure 6-7 (a), (b), (c) and (d) show the validation of surface heating algorithm where MD results are compared with the 1D heat equation at 1000 ps, 1005 ps, 1010 ps and 1020 ps respectively.

7 Near Surface Pressure Studies

7.1 Introduction

The study of near surface thermodynamic properties are of great interest to the heat transfer community to understand the behavior of water with different substrates while heating. In the past there are a few studies [132] done to understand the stability and other properties of the thin films near the surface. The detailed knowledge of the thermodynamic properties can help to understand lubrication on surface [133, 134], wetting and spreading [135, 136], condensation [137], evaporation, and boiling, as well as solidification and melting.

Most of the methods and works rely on indirect estimation of quantities like pressure. This includes estimation of disjoining pressure from empirical methods. In this chapter, we demonstrate how we can calculate these quantities directly from molecular simulations. For this, a system of water film on top of silicon di-oxide substrate is modeled, followed by MD simulation and estimation of local pressure and density using well established atomic to continuum methods. The pressure profile above the silicon dioxide substrate is estimated based on Hardy's method. The knowledge of pressure at this region is expected to strengthen our understanding about the heat removal and flow characteristics in solid-fluid systems at nanoscale.

7.2 Molecular Model of Water-SiO_2 System

Thin films of water are modeled on top of a silicon substrate and this water is maintained at room temperature using a thermostat. Water molecules are modeled using SPCE model. Silicon dioxide is modeled as a crystalline structure and hydrogen atoms are added on either surfaces to balance the partial charge imbalance. We have analyzed two cases in which the thickness of the water film used was 3 x 3 x 3 nm (as in Figure 7-1) for one case and 3 x 3 x 1 nm (as in Figure 7-2) for the other case. The silicon dioxide was having a size of 3 x 3 x 1 nm in Cartesian

coordinates. The simulation domain was of size 3 x 3 x 7 nm. The interaction parameters of SPCE molecules were same as in the chapter 2. The silicon dioxide – water interaction parameters are taken from literature [119].

The system is equilibrated at 300 K for 50000 steps with a time integration step of 2 fs. Then the production run is performed with estimation of the local pressure. The simulations are performed in LAMMPS and the local pressure is estimated using the Atomic to Continuum (ATC) package. The ATC package will run every 500 steps during the production time of 100000 steps.

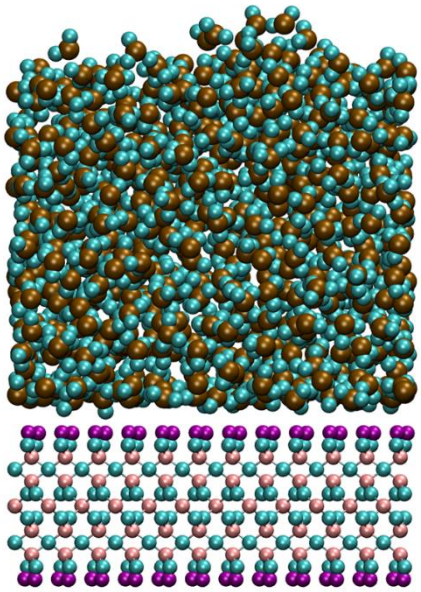

Figure 7-1. A 3 x 3 x 3 nm water film on top of silicon dioxide substrate.

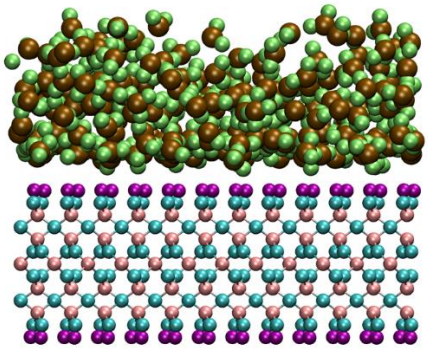

Figure 7-2. A 3 x 3 x 1 nm water film on top of SiO_2 substrate.

7.3 Pressure Estimation of the Water-SiO_2 System

The local pressure is estimated using the Hardy post processing method in ATC package. The concept behind the local pressure estimation is as follows and is similar as explained in the chapter 4. A mesh with spacing of 0.4 nm and a smearing radius of 0.7 nm was kept inside the simulation domain and performed the convolution of the local pressure with the mesh. This will give us the direct estimate of the local pressure from the molecular dynamics simulations. A typical mesh which overlaps the atomistic simulation domain is shown in Figure 7-3.

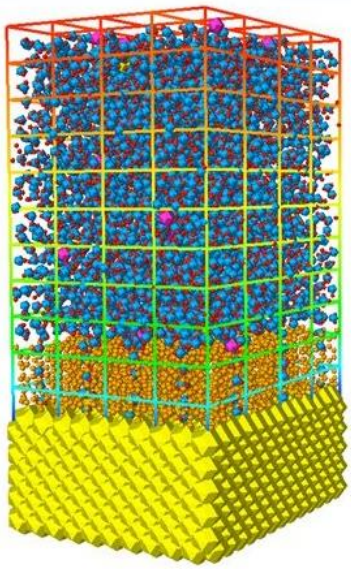

Figure 7-3. Atomistic to continuum simulation coupling. Image courtesy: Sandia National Labs

The estimated local pressure for the 3 nm thick water film is shown in Figure 7-4 and Figure 7-5 respectively. The Figure 7-4 represents the directional pressure components along each directions and Figure 7-5 represents the tangential and normal pressure of the water. The x-axis of these figures show the z-direction values in angstroms. The water film starts from 12 A, and extends upward. The z component of the pressure shows little variation along the vertical direction

while x and y components show a variation of the pressure near the interface of water and silicon dioxide. The peak pressure value of -2916 atm is observed near the liquid-solid interface.

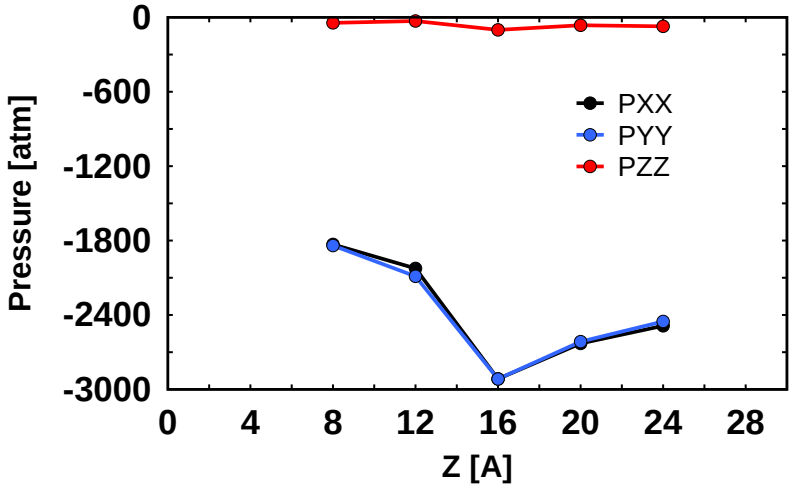

Figure 7-4. Pressure components along x, y and z of 3 nm water on top of SiO_2 along vertical (Z) direction

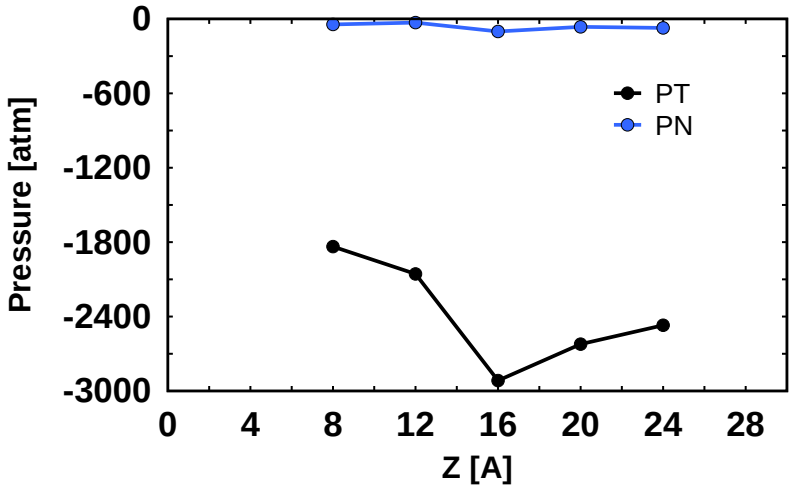

Figure 7-5. Normal and tangential components of pressure of 3 nm water on top of SiO2 along vertical (Z) direction

The local pressures estimated for the 1 nm water film on top of SiO_2 is shown in Figure 7-6 and Figure 7-7. The directional components of the pressure along x, y and z directions are shown in Figure 7-6 and the normal and tangential components of the pressure are shown in Figure 7-7. The trend in these pressure profiles are different from those of 3 nm thick water films.

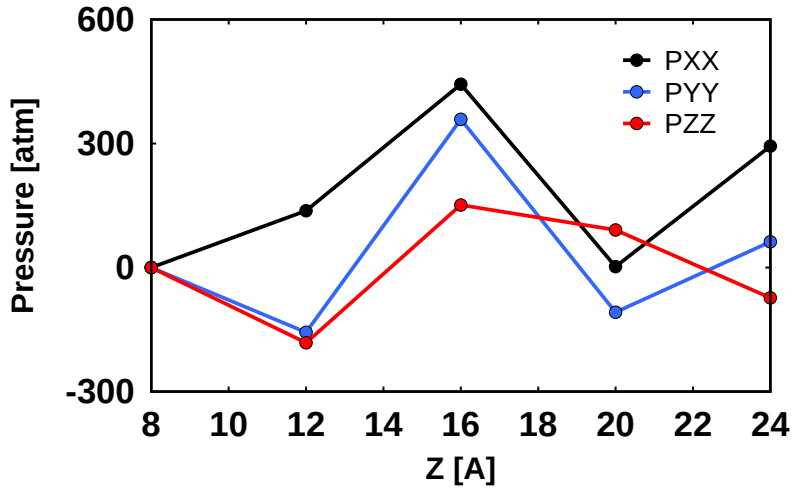

Figure 7-6. Pressure components along x, y and z of 1 nm water on top of SiO_2 along vertical (Z) direction

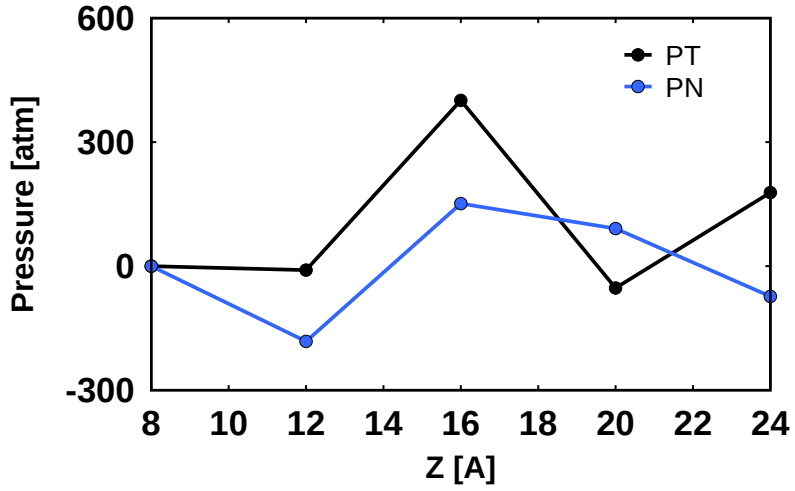

Figure 7-7. Normal and tangential components of the pressure of 1 nm water film on SiO2.

The maximum pressure of 1 nm water on SiO_2 was estimated to be 443 atm. The results from the figures show that the pressure reduces significantly when the liquid thickness was reduced. The 3 nm thick case shows a significant pressure near the surface and the pressure becomes relatively very low in the case of 1 nm water film. We have also estimated the surface tension of water and silicon dioxide from these pressure data. The surface tension is estimated as the difference between the normal and tangential values of the pressure. This estimation is done for both 1 nm and 3 nm cases and is shown in Figure 7-8. The surface tension is much higher for the 3 nm case. The total value of the surface tension can be obtained by integrating the curve in Figure 7-8 along z direction.

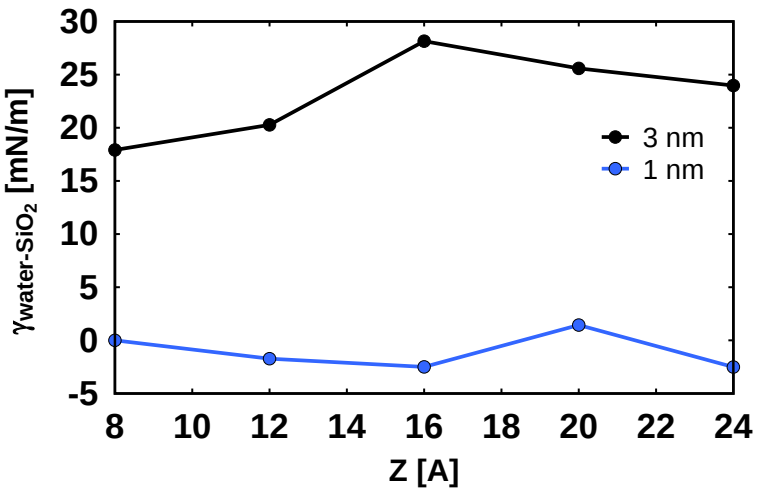

Figure 7-8. Surface tension of water-SiO_2 along the vertical direction.

7.4 Challenges in Estimation of Pressure

The estimation of the local pressure was challenging due to many reasons. One of the main reason is the computational power requirement. These local pressure modules are implemented in LAMMPS by the name atomistic to continuum (ATC) package. This package is currently serial version and for best performance we need to have a parallel version. Even with the existing

computational resources which includes two servers and a cluster, these studies will take months to finish, because the current ATC package won't utilize multiple processors as it is not multithreaded or parallel. Due to time limitations, we had to choose the estimation parameters based on that. For example, for better refinement and for more clarity we needed 0.1 nm grid spacing with 0.5 nm or lesser spread radius. But we have used 0.4 nm as the spacing, and the spread radius as 0.7 nm.

Currently we have simulated a domain with 3 nm by 3 nm sides and 7 nm height. Again, due to above limitations, we have selected the grid dimensions as a 2 nm x 2 nm x 2.4 nm mesh box inside the simulation region. This region had 54 nodes and the spacing was done as 3 x 3 x 6 along x, y and z directions respectively. These limitations currently makes it such that, it takes 2 days for the 3 nm water-SiO2 system in an Intel Xeon workstation. However the future versions of LAMMPS is expected to have the parallel versions of ATC and then we can study large scale problems with better detailing of the near surface pressure characteristics.

8 Conclusions and Future Work

8.1 Conclusions

8.1.1 Code development and validation

A C++ code was developed to perform MD simulations. This code was written by implementing major modules of the molecular dynamics simulation as mentioned in the chapter 2. The code has the capability to simulate argon, platinum and water using a set of potentials like Lennard-Jones (LJ), Coulomb and Zhu-Philpott (ZP potential). While LJ and Coulombic potentials are used for the argon-argon and water-water interactions, the ZP potential is used to simulate the accurate interaction between water and platinum. The water model used was SPCE and RATTLE algorithm was implemented to keep it rigid.

The code is also capable of simulating the long range Coulomb force interaction by Classical Ewald and Smooth Particle Mesh Ewald (SPME) technique. This method gives accurate long range forces and energies for charged species with 3D periodicity. The traditional Coulomb potential, which is a slowly convergent series is modified into two components where a real space component converges very fast in real space and a reciprocal space component converges fast in Fourier space. The SPME empowers the classical Ewald method by performing the Fourier transformation using FFT instead of DFT. More details of the SPME implementation is explained on the chapter 2.

The numerical integration scheme adopted was velocity verlet and different thermostat schemes like Berendsen, Nose-Hoover and velocity scaling is implemented and validated. As a standard case, argon liquid film suspended in argon vapor was studied. The surface tension, pressure and density of the suspended argon was compared against the standard database values for different temperatures and found to be in good agreement.

The code is also implemented with faster methods to calculate the interatomic potentials with modified cell list algorithm. The periodic boundary conditions are implemented and also the minimum image convention to replicate the neighboring cells. We have also implemented reflective boundary conditions which are equivalent to the adiabatic walls. These reflective boundaries don't have periodicity and work by principle of changing the atomic direction of the momentum away from it.

The water code is tested with calculation of the Radial Distribution Function (RDF) and contact angles. The RDF estimation results show the implementation was correct and matched the results with experiments and other MD software like GROMACS. The contact angle estimation validated the implementation of the ZP potential and surface heating algorithm as explained in the chapter 6. We have developed an efficient algorithm to estimate the contact angle from the MD simulation data and validated it with a set of studies as in chapter 3.

8.1.2 Local pressure estimation algorithm

Estimation of continuum level properties from the MD simulation is of great importance while studying the transient problems involving phase change and heat transfer. Local thermodynamic property estimation plays a key role in it, especially the estimation of local pressure and local density.

We have developed a faster version of the local pressure estimation based on Irving-Kirkwood-Hardy formalism in 2D. The classical approach of Hardy to use a 3D smearing (interpolation) function to distribute the pressure across the local 3D grids is modified appropriately to account for 2D grids. Often the system under study will be 2D inhomogeneous and doesn't require a full 3D knowledge of the pressure and density. Hence we modified the sampling local volume from spherical to cylindrical and reformulated the weight function and

avoided the necessity of the 3D estimation and averaging of the local pressure. We have also separated spread radius of the formula from cutoff radius, so that we can tune the details of the local thermodynamic quantities without losing any accuracy.

The local pressure module was validated by studying the surface tension and density of the liquid argon suspended in the vapor argon. The validated code was then used to estimate the surface tension of liquid-solid interface of argon-platinum. These results are believed to the first time in literature about estimating the surface tension directly from the MD simulations. We have given formulations for three more different types of smearing formula which can be used for different benefits including computational speed and mesh insensitivity.

8.1.3 Passive flow studies

Passive flow heat removal is a promising futuristic cooling method. Using the surface heating algorithm of argon-platinum we have simulated the passive flow of the liquid under a thermal gradient and estimated the heat removal rate. A thin film of argon was kept on top of a platinum plate and was heated in the middle at a higher temperature than the sides. This created a differential thermal zone and eventually led to difference in the solid-liquid surface tension. This gradient created a flow from the sides to the center of the system. When the middle temperature was high the argon from the center started evaporating directly to the bulk vapor and this augmented the passive flow.

The mass flow rate was estimated based on the local density variations and evaporative mass flux was estimated from the control volume analysis. Using these details and temperature we have estimated the heat removal rate from the system. The heat flux for argon was estimated as $20kW/cm^2$ and is promising for cooling devices.

8.1.4 Surface heating algorithm

To study the heat transfer behavior between the water and platinum, we need to have an accurate model in MD simulations. We have developed one such algorithm which can simulate solid-liquid heating that will allow us to study a whole new set of fundamental heat transfer problems at the nanoscale like surface heating/cooling of droplets, thin-films, etc. which was not yet possible.

The pre-existing surface heating algorithm for argon-platinum interaction was reformulated for water-platinum. The use of ZP potential made the estimation of critical radius as challenging. So we performed an empirical estimation of the critical radius for the anisotropic ZP potential. The details of the derivations and implementation was explained in the chapter 6.

The surface heating algorithm was validated with a set of analysis. At first two droplets with different sizes are heated for 1000ps and then estimated the droplet average temperature. The transient average temperature was showing good results for three different temperatures. Then, the droplets are subjected to evaporation. The droplet shown evaporation and achievement of steady state shape for different temperatures.

The water droplets are heated using the surface heating algorithm and estimated the contact angle. We have used our contact angle estimation algorithm to estimate the contact angles. Such estimated contact angles are compared with the literature and with the experimental results and found good agreement.

Further, the surface heating algorithm was validated with studying water film confined between platinum plates. The platinum walls' temperature was changed during the transient simulation and the 1D temperature profile was compared against the solution of 1D heat diffusion equation. The resulting profiles matched very well and more details are shown in the chapter 6.

8.1.5 Near surface pressure estimation

The pressure profile of water near to the silicon dioxide substrate was estimated using Hardy's method. The simulations were performed using LAMMPS software. Thin films of water with various thickness were kept on top of silicon dioxide wall and equilibrated. The pressure distribution near to the surface was then estimated using the atomic-to-continuum package of LAMMPS. These results will be helpful in understanding and estimation of disjoining pressure of water of various surfaces.

8.2 Future Work

8.2.1 Surface heating algorithm in LAMMPS

The surface heating algorithm that we developed is capable of performing transient heat transfer studies for a large number of thermal engineering problems. Currently our C++ code is serial version and hence the study of large systems using surface heating algorithm requires large amount of time. This can be circumvented if we can implement it in LAMMPS. By integrating our surface heating algorithm [138] into the open source MD software LAMMPS, we can extend it to the heat transfer research community. This will enable us to leverage the large scale and parallel computing modules on LAMMPS and perform the nanoscale heat transfer studies for larger channels, complex geometries etc. This integration of the algorithm requires creation of new "fix" in LAMMPS source code and sharing of the main variables including velocity, position and forces.

We can also implement this in LAMMPS for studying the systems with coarse grain molecular dynamics (CGMD). The heating algorithm parameters can be redefined for CGMD and this can open new possibilities and scales of the systems to explore.

8.2.2 Wettability and disjoining pressure of water

The studies performed and mentioned in chapter 7 can give insights about the near surface pressure characteristics of water with silicon di-oxide. This study can be extended further with different substrates and liquids. Till today the disjoining pressure was estimated using empirical methods and indirect calculation methods [139]. The disjoining pressure for such systems can be estimated with much better accuracy compared to the conventional estimation using Hamaker's constant. Also these studies can give better estimation of the capillary pressure from the molecular simulations. With the use of the modules that we developed and validated through chapters 3, 4, 5, 6 and 7, we can estimate and understand the pressure and surface tension characteristics of water near irregular and complex geometries.

We can apply these methodology to nano structures and capillary like devices which can give better understanding of development of high power electronics cooling devices.

8.2.3 Nano-pore evaporation and passive flow cooling

The concept of efficient Nano-wicking devices (Figure 8-1) can be investigated using molecular dynamics simulations. The existing heat transfer potential of passive nanowicking [13, 140] devices can be efficiently improved by performing detailed numerical studies. These existing experimental studies point out that utilizing negative liquid pressure for evaporation can allow us to achieve a heat flux of ~96 W/cm^2. This idea can be effectively explored if we can understand the change in thermodynamic parameters like pressure, density, surface tension, temperature of water near to the surface and other nanoscale structures. Leveraging the heat transfer algorithms [117, 138] we developed as explained in chapter 6, we can perform MD simulations to understand the transient *thermal, fluidic and thermodynamics* behavior of thin films at the solid-liquid interface with varying surface wettability.

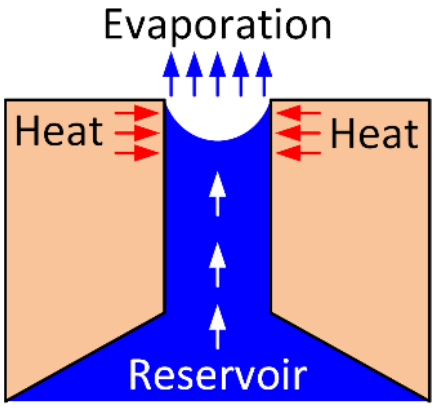

Figure 8-1. Conceptual model of nano pore evaporation

Using the available mathematical schemes like Hardy stress and Irving-Kirkwood theory and the modified versions of local pressure as mentioned in chapter 4, we can estimate continuum level thermodynamic properties like pressure, velocity, density and surface tension from MD simulations. Towards this goal, the MD code that we developed can be multithreaded or parallelized. Alternatively we can use the LAMMPS with surface heating algorithm implemented on it. We can extend the current simulations on negative pressure [141] simulation (as in chapter 5) on platinum flat surfaces to nanopores and other geometries. This is expected to show a nanowicking effect. By studying the change in thermodynamic properties in nanopores during heating, we shall be able to understand and create models on passive pumping, which can potentially be integrated into CFD and other mesoscale simulations. There are still challenges in simulating the reservoir, evaporating atmosphere and other boundary conditions. The pore dimensions in the range of 5-10 nm is expected to give better passive flow results.

REFERENCES

[1] Kandlikar, S. G., Review and Projections of Integrated Cooling Systems for Three-Dimensional Integrated Circuits, *Journal of Electronic Packaging*, vol. 136, no. 2, p. 024001, 2014.(article)

[2] Gambill, W. R., and Lienhard, J. H., An Upper Bound for the Critical Boiling Heat Flux, *J. Heat Transfer-Trans. ASME*, vol. 111, no. 1-4, pp. 815-818, 1989.(article)

[3] Koch, G. W., *et al.*, The Limits to Tree Height, *Nature*, vol. 428, no. 6985, pp. 851-854, 2004.(article)

[4] Maroo, S., and Chung, J., Negative Pressure Characteristics of an Evaporating Meniscus at Nanoscale, *Nanoscale research letters*, vol. 6, no. 1, p. 72, 2011.(article)

[5] Angell, C., Approaching the Limits, *Nature*, vol. 331, no., pp. 206-207, 1988.(article)

[6] Zhang, R., *et al.*, Negative Capillary-Pressure-Induced Cavitation Probability in Nanochannels, *Nanotechnology*, vol. 21, no. 10, p. 105706, 2010.(article)

[7] Wheeler, T. D., and Stroock, A. D., The Transpiration of Water at Negative Pressures in a Synthetic Tree, *Nature*, vol. 455, no. 7210, pp. 208-212, 2008.(article)

[8] Briggs, L. J., Maximum Superheating of Water as a Measure of Negative Pressure, *Journal of Applied Physics*, vol. 26, no. 8, pp. 1001-1003, 1955.(article)

[9] Maxwell, J. C., *Theory of Heat*, Longmans, 1921.(book)

[10] Tas, N. R., *et al.*, Capillarity Induced Negative Pressure of Water Plugs in Nanochannels, *Nano Letters*, vol. 3, no. 11, pp. 1537-1540, 2003.(article)

[11] Yang, S. H., *et al.*, Nanoscale Water Capillary Bridges under Deeply Negative Pressure, *Chemical Physics Letters*, vol. 451, no. 1, pp. 88-92, 2008.(article)

[12] Nosonovsky, M., and Bhushan, B., Phase Behavior of Capillary Bridges: Towards Nanoscale Water Phase Diagram, *Physical Chemistry Chemical Physics*, vol. 10, no. 16, pp. 2137-2144, 2008.(article)

[13] Xiao, R., *et al.*, Negative Pressures in Nanoporous Membranes for Thin Film Evaporation, *Appl. Phys. Lett.*, vol. 102, no. 12, p. 123103, 2013.(article)

[14] Alder, B., and Wainwright, T., Phase Transition for a Hard Sphere System, *The Journal of Chemical Physics*, vol. 27, no. 5, pp. 1208-1209, 1957.(article)

[15] Rahman, A., Correlations in the Motion of Atoms in Liquid Argon, *Physical Review*, vol. 136, no. 2A, p. A405, 1964.(article)

[16] Lee, J. K., *et al.*, Surface Structure and Surface Tension: Perturbation Theory and Monte Carlo Calculation, *The Journal of Chemical Physics*, vol. 60, no. 5, pp. 1976-1980, 1974.(article)

[17] contributors, W., 2016, "Molecular Dynamics.."

[18] Alejandre, J., *et al.*, Molecular Dynamics Simulation of the Orthobaric Densities and Surface Tension of Water, *The Journal of chemical physics*, vol. 102, no. 11, pp. 4574-4583, 1995.(article)

[19] Weng, J.-G., *et al.*, Molecular Dynamics Investigation of Thickness Effect on Liquid Films, *The Journal of Chemical Physics*, vol. 113, no. 14, pp. 5917-5923, 2000.(article)

[20] Hoover, W. G., Canonical Dynamics: Equilibrium Phase-Space Distributions, *Physical Review A*, vol. 31, no. 3, pp. 1695-1697, 1985.(article)

[21] Hess, B., *et al.*, Gromacs 4: Algorithms for Highly Efficient, Load-Balanced, and Scalable Molecular Simulation, *Journal of Chemical Theory and Computation*, vol. 4, no. 3, pp. 435-447, 2008.(article)

[22] Berendsen, H. J., *et al.*, Molecular Dynamics with Coupling to an External Bath, *The Journal of Chemical Physics*, vol. 81, no. 8, pp. 3684-3690, 1984.(article)

[23] Mattson, W., and Rice, B. M., Near-Neighbor Calculations Using a Modified Cell-Linked List Method, *Computer Physics Communications*, vol. 119, no. 2, pp. 135-148, 1999.(article)

[24] Lemmon, E., *et al.*, Thermophysical Properties of Fluid Systems, *NIST chemistry webbook, NIST standard reference database*, vol. 69, no., 2005.(article)

[25] Maroo, S. C., and Chung, J., A Novel Fluid–Wall Heat Transfer Model for Molecular Dynamics Simulations, *J. Nanopart. Res.*, vol. 12, no. 5, pp. 1913-1924, 2010.(article)

[26] Pronk, S., *et al.*, Gromacs 4.5: A High-Throughput and Highly Parallel Open Source Molecular Simulation Toolkit, *Bioinformatics*, vol. 29, no. 7, pp. 845-854, 2013.(article)

[27] Liem, S. Y., *et al.*, Investigation of the Homogeneous-Shear Nonequilibrium-Molecular-Dynamics Method, *Physical Review A*, vol. 45, no. 6, p. 3706, 1992.(article)

[28] Van Der Spoel, D., and van Maaren, P. J., The Origin of Layer Structure Artifacts in Simulations of Liquid Water, *Journal of Chemical Theory and Computation*, vol. 2, no. 1, pp. 1-11, 2006.(article)

[29] Qiu, B., *et al.*, Molecular Dynamics Simulations of Lattice Thermal Conductivity and Spectral Phonon Mean Free Path of Pbte: Bulk and Nanostructures, *Computational Materials Science*, vol. 53, no. 1, pp. 278-285, 2012.(article)

[30] Saha, S. K., and Shi, L., Molecular Dynamics Simulation of Thermal Transport at a Nanometer Scale Constriction in Silicon, *Journal of applied physics*, vol. 101, no. 7, p. 074304, 2007.(article)

[31] Koplik, J., *et al.*, Molecular Dynamics of Fluid Flow at Solid Surfaces, *Physics of Fluids A: Fluid Dynamics (1989-1993)*, vol. 1, no. 5, pp. 781-794, 1989.(article)

[32] Abraham, F. F., The Interfacial Density Profile of a Lennard-Jones Fluid in Contact with a (100) Lennard-Jones Wall and Its Relationship to Idealized Fluid/Wall Systems: A Monte Carlo Simulation, *The Journal of Chemical Physics*, vol. 68, no. 8, pp. 3713-3716, 1978.(article)

[33] Yi, P., *et al.*, Molecular Dynamics Simulation of Vaporization of an Ultra-Thin Liquid Argon Layer on a Surface, *International Journal of Heat and Mass Transfer*, vol. 45, no. 10, pp. 2087-2100, 2002.(article)

[34] Kapitza, P., Heat Transfer and Superfluidity of Helium Ii, *Phys. Rev.*, vol. 60, no. 4, p. 354, 1941.(article)

[35] Nagayama, G., *et al.*, On the Evaporation Rate of Ultra-Thin Liquid Film at the Nanostructured Surface: A Molecular Dynamics Study, *International Journal of Thermal Sciences*, vol. 49, no. 1, pp. 59-66, 2010.(article)

[36] Heinbuch, U., and Fischer, J., Liquid Flow in Pores: Slip, No-Slip, or Multilayer Sticking, *Physical Review A*, vol. 40, no. 2, p. 1144, 1989.(article)

[37] Hens, A., *et al.*, Nanoscale Study of Boiling and Evaporation in a Liquid Ar Film on a Pt Heater Using Molecular Dynamics Simulation, *International Journal of Heat and Mass Transfer*, vol. 71, no., pp. 303-312, 2014.(article)

[38] Bernardi, S., *et al.*, Thermostating Highly Confined Fluids, *The Journal of chemical physics*, vol. 132, no. 24, p. 244706, 2010.(article)

[39] Stoddard, S. D., and Ford, J., Numerical Experiments on the Stochastic Behavior of a Lennard-Jones Gas System, *Physical Review A*, vol. 8, no. 3, pp. 1504-1513, 1973.(article)

[40] Maroo, S. C., and Chung, J., Molecular Dynamic Simulation of Platinum Heater and Associated Nano-Scale Liquid Argon Film Evaporation and Colloidal Adsorption Characteristics, *Journal of colloid and interface science*, vol. 328, no. 1, pp. 134-146, 2008.(article)

[41] Matthey, T., 2002, "Framework Design, Parallelization and Force Computation in Molecular Dynamics," Citeseer.

[42] Essmann, U., *et al.*, A Smooth Particle Mesh Ewald Method, *The Journal of Chemical Physics*, vol. 103, no. 19, pp. 8577-8593, 1995.(article)

[43] Andersen, H. C., Rattle: A "Velocity" Version of the Shake Algorithm for Molecular Dynamics Calculations, *J. Comput. Phys.*, vol. 52, no. 1, pp. 24-34, 1983.(article)

[44] Ryckaert, J.-P., *et al.*, Numerical Integration of the Cartesian Equations of Motion of a System with Constraints: Molecular Dynamics of N-Alkanes, *Journal of Computational Physics*, vol. 23, no. 3, pp. 327-341, 1977.(article)

[45] Swope, W. C., *et al.*, A Computer Simulation Method for the Calculation of Equilibrium Constants for the Formation of Physical Clusters of Molecules: Application to Small Water Clusters, *The Journal of Chemical Physics*, vol. 76, no. 1, pp. 637-649, 1982.(article)

[46] Soper, A., The Radial Distribution Functions of Water and Ice from 220 to 673 K and at Pressures up to 400 Mpa, *Chemical Physics*, vol. 258, no. 2, pp. 121-137, 2000.(article)

[47] Shi, B., *et al.*, Molecular Simulation of the Contact Angle of Water Droplet on a Platinum Surface, Proc. *ASME International Mechanical Engineering Congress and Exposition*, American Society of Mechanical Engineers, Orlando, Florida, USA, November 5-11, pp. 93-97, 2005.(conference)

[48] Eastwood, J., *et al.*, P3m3dp-the Three-Dimensional Periodic Particle-Particle/Particle-Mesh Program, *Computer Physics Communications*, vol. 19, no. 2, pp. 215-261, 1980.(article)

[49] Kandlikar, S. G., *et al.*, Molecular Dynamics Simulation and Measurement of Contact Angle of Water Droplet on a Platinum Surface, Proc. *ASME International Mechanical Engineering Congress and Exposition*, American Society of Mechanical Engineers, Denver, Colorado, USA, November 11-17, pp. 343-348, 2001.(conference)

[50] Barisik, M., and Beskok, A., Wetting Characterisation of Silicon (1, 0, 0) Surface, *Molecular Simulation*, vol. 39, no. 9, pp. 700-709, 2013.(article)

[51] Santiso, E. E., *et al.*, On the Calculation of Solid-Fluid Contact Angles from Molecular Dynamics, *Entropy*, vol. 15, no. 9, pp. 3734-3745, 2013.(article)

[52] Malani, A., *et al.*, Can Dynamic Contact Angle Be Measured Using Molecular Modeling?, *Physical Review Letters*, vol. 109, no. 18, p. 5, 2012.(article)

[53] Sergi, D., *et al.*, Molecular Dynamics Simulations of the Contact Angle between Water Droplets and Graphite Surfaces, *Fluid Phase Equilibria*, vol. 332, no., pp. 173-177, 2012.(article)

[54] Ohler, B., and Langel, W., Molecular Dynamics Simulations on the Interface between Titanium Dioxide and Water Droplets: A New Model for the Contact Angle, *Journal of physical chemistry. C*, vol. 113, no. 23, pp. 10189-10197,

[55] Blake, T. D., *et al.*, Contact Angle Relaxation During Droplet Spreading: Comparison between Molecular Kinetic Theory and Molecular Dynamics, *Langmuir*, vol. 13, no. 7, pp. 2164-2166, 1997.(article)

[56] Nijmeijer, M. J. P., *et al.*, A Visual Measurement of Contact Angles in a Molecular-Dynamics Simulation, *Physica A*, vol. 160, no. 2, pp. 166-180, 1989.(article)

[57] Hong, S., *et al.*, Static and Dynamic Contact Angles of Water Droplet on a Solid Surface Using Molecular Dynamics Simulation, *Journal of colloid and interface science*, vol. 339, no. 1, pp. 187-195, 2009.(article)

[58] Mahalanobis, P. C., On the Generalized Distance in Statistics, *Proceedings of the National Institute of Sciences (Calcutta)*, vol. 2, no., pp. 49-55, 1936.(article)

[59] De Maesschalck, R., *et al.*, The Mahalanobis Distance, *Chemometrics and Intelligent Laboratory Systems*, vol. 50, no. 1, pp. 1-18, 2000.(article)

[60] Hockney, R. W., and Eastwood, J. W., *Computer Simulation Using Particles*, CRC Press, Bristol, UK, 2010.(book)

[61] Hardy, R. J., Formulas for Determining Local Properties in Molecular-Dynamics Simulations: Shock Waves, *J. Chem. Phys.*, vol. 76, no. 1, pp. 622-628, **1982**.(article)

[62] Thomas, S. M., and Chan, Y., A Simple Approach for the Estimation of Circular Arc Center and Its Radius, *Computer Vision, Graphics, and Image Processing*, vol. 45, no. 3, pp. 362-370, 1989.(article)

[63] Berendsen, H., *et al.*, The Missing Term in Effective Pair Potentials, *J. Phys. Chem.*, vol. 91, no. 24, pp. 6269-6271, 1987.(article)

[64] Hess, B., *et al.*, Lincs: A Linear Constraint Solver for Molecular Simulations, *J. Comput. Chem.*, vol. 18, no. 12, pp. 1463-1472, 1997.(article)

[65] Bussi, G., *et al.*, Canonical Sampling through Velocity Rescaling, *The Journal of Chemical Physics*, vol. 126, no. 014101, pp. 1-7, 2007.(article)

[66] Horstemeyer, M. F., **2010**, "Multiscale Modeling: A Review," Practical Aspects of Computational Chemistry, Springer, pp. 87-135.

[67] Steinhauser, M. O., *Computational Multiscale Modeling of Fluids and Solids*, Springer, **2008**.(book)

[68] Irving, J., and Kirkwood, J. G., The Statistical Mechanical Theory of Transport Processes. Iv. The Equations of Hydrodynamics, *J. Chem. Phys.*, vol. 18, no. 6, pp. 817-829, **1950**.(article)

[69] Hardy, R. J., *et al.*, Continuum Properties from Molecular Simulations, Proc. *AIP Conf. Proc.*, IOP Publishing, pp. 363-366, **2002**.(conference)

[70] Zhou, M., A New Look at the Atomic Level Virial Stress: On Continuum-Molecular System Equivalence, Proc. *Proc. R. Soc. A*, The Royal Society, pp. 2347-2392, **2003**.(conference)

[71] Zimmerman, J. A., *et al.*, Calculation of Stress in Atomistic Simulation, *Modell. Simul. Mater. Sci. Eng.*, vol. 12, no. 4, p. S319, **2004**.(article)

[72] Gall, K., *et al.*, The Strength of Gold Nanowires, *Nano Lett.*, vol. 4, no. 12, pp. 2431-2436, **2004**.(article)

[73] Buehler, M. J., and Gao, H., Dynamical Fracture Instabilities Due to Local Hyperelasticity at Crack Tips, *Nature*, vol. 439, no. 7074, pp. 307-310, **2006**.(article)

[74] Gates, T., *et al.*, Computational Materials: Multi-Scale Modeling and Simulation of Nanostructured Materials, *Compos. Sci. Technol.*, vol. 65, no. 15, pp. 2416-2434, **2005**.(article)

[75] Murdoch, A. I., A Critique of Atomistic Definitions of the Stress Tensor, *J. Elasticity*, vol. 88, no. 2, pp. 113-140, **2007**.(article)

[76] Subramaniyan, A. K., and Sun, C., Continuum Interpretation of Virial Stress in Molecular Simulations, *Int. J. Solids Struct.*, vol. 45, no. 14, pp. 4340-4346, **2008**.(article)

[77] Admal, N. C., and Tadmor, E. B., A Unified Interpretation of Stress in Molecular Systems, *J. Elasticity*, vol. 100, no. 1-2, pp. 63-143, **2010**.(article)

[78] Zimmerman, J. A., *et al.*, A Material Frame Approach for Evaluating Continuum Variables in Atomistic Simulations, *J. Comput. Phys.*, vol. 229, no. 6, pp. 2364-2389, **2010**.(article)

[79] Yang, J. Z., *et al.*, A Generalized Irving–Kirkwood Formula for the Calculation of Stress in Molecular Dynamics Models, *J. Chem. Phys.*, vol. 137, no. 13, p. 134104, **2012**.(article)

[80] Vanegas, J. M., *et al.*, Importance of Force Decomposition for Local Stress Calculations in Biomembrane Molecular Simulations, *J. Chem. Theory Comput.*, vol. 10, no. 2, pp. 691-702, **2014**.(article)

[81] Torres-Sánchez, A., *et al.*, Examining the Mechanical Equilibrium of Microscopic Stresses in Molecular Simulations, *Phys. Rev. Lett.*, vol. 114, no. 25, p. 258102, **2015**.(article)

[82] Ollila, O. S., *et al.*, 3d Pressure Field in Lipid Membranes and Membrane-Protein Complexes, *Phys. Rev. Lett.*, vol. 102, no. 7, p. 078101, **2009**.(article)

[83] Sonne, J., *et al.*, Methodological Problems in Pressure Profile Calculations for Lipid Bilayers, *The Journal of chemical physics*, vol. 122, no. 12, p. 124903, 2005.(article)

[84] Lindahl, E., and Edholm, O., Spatial and Energetic-Entropic Decomposition of Surface Tension in Lipid Bilayers from Molecular Dynamics Simulations, *The Journal of Chemical Physics*, vol. 113, no. 9, pp. 3882-3893, 2000.(article)

[85] Heyes, D., *et al.*, The Equivalence between Volume Averaging and Method of Planes Definitions of the Pressure Tensor at a Plane, *The Journal of chemical physics*, vol. 135, no. 2, p. 024512, 2011.(article)

[86] Lee, S. H., Pressure Analyses at the Planar Surface of Liquid-Vapor Argon by a Test-Area Molecular Dynamics Simulation, *Bull. Korean Chem. Soc.*, vol. 33, no. 9, pp. 3039-3042, **2012**.(article)

[87] Weng, J.-G., *et al.*, Molecular Dynamics Investigation of Thickness Effect on Liquid Films, *J. Chem. Phys.*, vol. 113, no. 14, pp. 5917-5923, **2000**.(article)

[88] Tyree, M. T., Plant Hydraulics: The Ascent of Water, *Nature*, vol. 423, no. 6943, pp. 923-923, 2003.(article)

[89] Kundan, A., *et al.*, Thermocapillary Phenomena and Performance Limitations of a Wickless Heat Pipe in Microgravity, *Phys. Rev. Lett.*, vol. 114, no. 14, p. 146105, 2015.(article)

[90] Tam, D., *et al.*, Marangoni Convection in Droplets on Superhydrophobic Surfaces, *J. Fluid Mech.*, vol. 624, no., pp. 101-123, 2009.(article)

[91] Zhang, K., *et al.*, Temperature Distribution Along the Surface of Evaporating Droplets, *Phys. Rev. E*, vol. 89, no. 3, p. 032404, 2014.(article)

[92] Cai, Y., and Zhang Newby, B.-m., Marangoni Flow-Induced Self-Assembly of Hexagonal and Stripelike Nanoparticle Patterns, *J. Am. Chem. Soc.*, vol. 130, no. 19, pp. 6076-6077, 2008.(article)

[93] Pratt, D. M., and Kihm, K. D., Binary Fluid Mixture and Thermocapillary Effects on the Wetting Characteristics of a Heated Curved Meniscus, *J. Heat Transfer*, vol. 125, no. 5, pp. 867-874, 2003.(article)

[94] Wang, Y., *et al.*, Combined Effects of Underlying Substrate and Evaporative Cooling on the Evaporation of Sessile Liquid Droplets, *Soft matter*, vol. 11, no. 28, pp. 5632-5640, 2015.(article)

[95] Huang, D., *et al.*, The Capillary Outward Flow inside Pinned Drying Droplets, *Int. J. Heat Mass Transfer*, vol. 83, no., pp. 307-310, 2015.(article)

[96] Nie, C., *et al.*, A Microfluidic Device Based on an Evaporation-Driven Micropump, *Biomed. Microdevices*, vol. 17, no. 2, pp. 1-12, 2015.(article)

[97] Maroo, S. C., and Chung, J. N., A Novel Fluid-Wall Heat Transfer Model for Molecular Dynamics Simulations, *J. Nanopart. Res.*, vol. 12, no. 5, pp. 1913-1924, 2010.(article)

[98] Yd, S., and Maroo, S. C., Surface-Heating Algorithm for Water at Nanoscale, *The Journal of Physical Chemistry Letters*, vol. 6, no. 18, pp. 3765-3769, 2015.(article)

[99] YD, S., and Maroo, S. C., Two-Dimensional Pressure Formulation in Molecular Dynamics, *submitted*, no., 2016.(article)

[100] Irving, J. H., and Kirkwood, J. G., The Statistical Mechanical Theory of Transport Processes .4. The Equations of Hydrodynamics, *J. Chem. Phys.*, vol. 18, no. 6, pp. 817-829, 1950.(article)

[101] Raghavan, K., *et al.*, Structure and Dynamics of Water at the Pt (111) Interface: Molecular Dynamics Study, *The Journal of chemical physics*, vol. 94, no. 3, pp. 2110-2117, 1991.(article)

[102] Heinzinger, K., and Spohr, E., Computer Simulations of Water—Metal Interfaces, *Electrochimica Acta*, vol. 34, no. 12, pp. 1849-1856, 1989.(article)

[103] Zhu, S.-B., and Philpott, M. R., 1994, Interaction of Water with Metal Surfaces, DTIC Document.

[104] Shi, B., and Dhir, V. K., Molecular Dynamics Simulation of the Contact Angle of Liquids on Solid Surfaces, *The Journal of chemical physics*, vol. 130, no. 3, p. 034705, 2009.(article)

[105] Berendsen, H. J., *et al.*, Molecular Dynamics with Coupling to an External Bath, *The J. of Chem. Phys.*, vol. 81, no. 8, pp. 3684-3690, 1984.(article)

[106] Nosé, S., A Unified Formulation of the Constant Temperature Molecular Dynamics Methods, *The J. of Chem. Phys.*, vol. 81, no. 1, pp. 511-519, 1984.(article)

[107] Yi, P., *et al.*, Molecular Dynamics Simulation of Vaporization of an Ultra-Thin Liquid Argon Layer on a Surface, *Intl J. of Heat and Mass Transfer*, vol. 45, no. 10, pp. 2087-2100, 2002.(article)

[108] Maroo, S. C., and Chung, J., Molecular Dynamic Simulation of Platinum Heater and Associated Nano-Scale Liquid Argon Film Evaporation and Colloidal Adsorption Characteristics, *J. of Colloid and Interface Science*, vol. 328, no. 1, pp. 134-146, 2008.(article)

[109] De Luca, S., *et al.*, A New and Effective Method for Thermostatting Confined Fluids, *The Journal of chemical physics*, vol. 140, no. 5, p. 054502, 2014.(article)

[110] Hu, H., and Sun, Y., Effect of Nanopatterns on Kapitza Resistance at a Water-Gold Interface During Boiling: A Molecular Dynamics Study, *Journal of Applied Physics*, vol. 112, no. 5, p. 053508, 2012.(article)

[111] Mao, Y., and Zhang, Y., Molecular Dynamics Simulation on Rapid Boiling of Water on a Hot Copper Plate, *Applied Thermal Engineering*, vol. 62, no. 2, pp. 607-612, 2014.(article)

[112] Maruyama, S., *et al.*, Molecular Scale Aspects of Liquid Contact on a Solid Surface, Proc. *NATIONAL HEAT TRANSFER SYMPOSIUM OF JAPAN*, Japan Heat Transfer Society; 1999, pp. 577-578, 2002.(conference)

[113] Yang, T., and Pan, C., Molecular Dynamics Simulation of a Thin Water Layer Evaporation and Evaporation Coefficient, *International journal of heat and mass transfer*, vol. 48, no. 17, pp. 3516-3526, 2005.(article)

[114] Yang, X., and Yan, Y., Molecular Dynamics Simulation for Microscope Insight of Water Evaporation on a Heated Magnesium Surface, *Applied Thermal Engineering*, vol. 31, no. 5, pp. 640-648, 2011.(article)

[115] Wang, B.-B., *et al.*, Molecular Dynamics Simulations on Evaporation of Droplets with Dissolved Salts, *Entropy*, vol. 15, no. 4, pp. 1232-1246, 2013.(article)

[116] Saha, S. K., and Shi, L., Molecular Dynamics Simulation of Thermal Transport at a Nanometer Scale Constriction in Silicon, *J. of Applied Phys.*, vol. 101, no. 7, p. 074304, 2007.(article)

[117] Maroo, S. C., and Chung, J., A Novel Fluid–Wall Heat Transfer Model for Molecular Dynamics Simulations, *J. of Nanoparticle Research*, vol. 12, no. 5, pp. 1913-1924, 2010.(article)

[118] Berendsen, H., *et al.*, The Missing Term in Effective Pair Potentials, *J. of Phys. Chem.*, vol. 91, no. 24, pp. 6269-6271, 1987.(article)

[119] Raj, R., *et al.*, Wettability of Graphene, *Nano Lett.*, vol. 13, no. 4, pp. 1509-1515, 2013.(article)

[120] Taherian, F., *et al.*, What Is the Contact Angle of Water on Graphene?, *Langmuir*, vol. 29, no. 5, pp. 1457-1465, 2013.(article)

[121] Sergi, D., *et al.*, Molecular Dynamics Simulations of the Contact Angle between Water Droplets and Graphite Surfaces, *Fluid Phase Equilibria*, vol. 332, no. 1, pp. 173-177, 2012.(article)

[122] Werder, T., *et al.*, Molecular Dynamics Simulation of Contact Angles of Water Droplets in Carbon Nanotubes, *Nano Lett.*, vol. 1, no. 12, pp. 697-702, 2001.(article)

[123] Werder, T., *et al.*, On the Water-Carbon Interaction for Use in Molecular Dynamics Simulations of Graphite and Carbon Nanotubes, *The Journal of Physical Chemistry B*, vol. 107, no. 6, pp. 1345-1352, 2003.(article)

[124] Hong, S. D., *et al.*, Static and Dynamic Contact Angles of Water Droplet on a Solid Surface Using Molecular Dynamics Simulation, *Journal of colloid and interface science*, vol. 339, no. 1, pp. 187-195, 2009.(article)

[125] Grigera, J. R., *et al.*, Wall-Water Interface. A Molecular Dynamics Study, *Langmuir*, vol. 12, no. 1, pp. 154-158, 1996.(article)

[126] Hirvi, J. T., and Pakkanen, T. A., Molecular Dynamics Simulations of Water Droplets on Polymer Surfaces, *The Journal of chemical physics*, vol. 125, no. 14, p. 144712, 2006.(article)

[127] Kimura, T., and Maruyama, S., Molecular Dynamics Simulation of Water Droplet in Contact with a Platinum Surface, *Heat Transfer*, vol. 1, no., pp. 537-542, 2002.(article)

[128] YD, S., and Maroo, S. C., A New Algorithm for Contact Angle Estimation in Molecular Dynamics Simulations, *arXiv preprint arXiv:1505.05932*, no., 2015.(article)

[129] Young, T., An Essay on the Cohesion of Fluids, *Philo. Trans. of the Royal Society of London*, no., pp. 65-87, 1805.(article)

[130] Laplace, P. S., *Traité De Mécanique Céleste*, de l'Imprimerie de Crapelet, 1805.(book)

[131] DasGupta, S., *et al.*, Use of the Kelvin-Clapeyron Equation to Model an Evaporating Curved Microfilm, *Previews of Heat and Mass Transfer*, vol. 2, no. 21, p. 128, 1995.(article)

[132] Hu, H., *et al.*, Effect of Nanostructures on the Meniscus Shape and Disjoining Pressure of Ultrathin Liquid Film, *Nano Lett.*, vol. 14, no. 12, pp. 7131-7137, 2014.(article)

[133] Hsiao, E., *et al.*, Effects of Nanoscale Surface Texturing on Self-Healing of Boundary Lubricant Film Via Lateral Flow, *Tribology Letters*, vol. 44, no. 2, pp. 287-292, 2011.(article)

[134] Itoh, S., *et al.*, Shear Thinning of Nanometer-Thick Liquid Lubricant Films Measured at High Shear Rates, *Tribology Letters*, vol. 53, no. 3, pp. 555-567, 2014.(article)

[135] Kondiparty, K., *et al.*, Wetting and Spreading of Nanofluids on Solid Surfaces Driven by the Structural Disjoining Pressure: Statics Analysis and Experiments, *Langmuir*, vol. 27, no. 7, pp. 3324-3335, 2011.(article)

[136] Mate, C. M., Spreading Kinetics of Lubricant Droplets on Magnetic Recording Disks, *Tribology Letters*, vol. 51, no. 3, pp. 385-395, 2013.(article)

[137] Narayanan, S., *et al.*, Heat and Mass Transfer During Evaporation of Thin Liquid Films Confined by Nanoporous Membranes Subjected to Air Jet Impingement, *International Journal of Heat and Mass Transfer*, vol. 58, no. 1, pp. 300-311, 2013.(article)

[138] Yesudasan, S., and Maroo, S. C., Surface-Heating Algorithm for Water at Nanoscale, *The Journal of Physical Chemistry Letters*, vol. 6, no. 18, pp. 3765-3769, 2015.(article)

[139] Hu, H., *et al.*, Model of Meniscus Shape and Disjoining Pressure of Thin Liquid Films on Nanostructured Surfaces with Electrostatic Interactions, *The Journal of Physical Chemistry C*, vol. 119, no. 21, pp. 11777-11785, 2015.(article)

[140] Adera, S., *et al.*, Capillary-Limited Evaporation from Well-Defined Microstructured Surfaces, Proc. *ASME 2013 4th International Conference on Micro/Nanoscale Heat and Mass Transfer*, American Society of Mechanical Engineers, pp. V001T011A006-V001T011A006, 2013.(conference)

[141] YD, S., and Maroo, S. C., Non-Equilibrium Molecular Dynamics of Passive Flow and Negative Pressure at Nanoscales, *In Prep.*, no., 2016.(article)

Biographical Sketch

Sumith Yesudasan Daisy (Sumith YD) was born in 1983 in Kerala, India. He received his Bachelors in mechanical engineering from University of Kerala in 2005 and Masters in manufacturing technology from National Institute of Technology Calicut in 2007. He worked as a mechanical engineer in GE Energy from 2007 to 2011 and as an advanced analysis engineer in Delphi Automotive from 2011 to 2012. He joined the Department of Mechanical and Aerospace Engineering at Syracuse University in 2012 to pursue his PhD with Prof. Shalabh C. Maroo. Sumith completed his research work for the Doctor of Philosophy degree in summer 2016. He will be joining as a postdoctoral research associate at University of Georgia.